UDC 533.6.011.72.082.5 :
533.697.4 :
629.76.062

TECHNICAL REPORT OF NATIONAL AEROSPACE LABORATORY

TR-286T

An Investigation of Secondary Injection Thrust Vector Control

Tatsuo YAMANAKA

May 1972

NATIONAL AEROSPACE LABORATORY

CHŌFU, TOKYO, JAPAN

List of NAL Technical Reports

TR-256 On the Aerodynamic Damping Moment in Pitch of a Rigid Helicopter Rotor in Hovering	Kingo TAKAZAWA	Nov. 1971
TR-257 The Dynamic Stability of a Connected Rod under Periodic Longitudinal Force	Masaaki SANO	Jan. 1972
TR-258 Three Dimensional Suboptimal Explicit Guidance for Space Vehicles	Koji OTSUBO	Jan. 1972
TR-259 Study on a Rotary-Drive Vibratory-Output Rate Gyro	Hiroshi YAMADA	Jan. 1972
TR-260 A High Sensitive Total Atmospheric Temperature Measuring Apparatus	Kenji NISHIO, Hiroyuki NOSE, Takeshi KOSHINUMA, Shigeo INOUE, Hiroshi USUI & Toshimi OHATA	Jan. 1972
TR-261 Strain Measurement of Solid Propellant Material with Birefringent Coating	Shinichi KOSHIDE	Jan. 1972
TR-262 A Structuctural Analysis of Cylinder-Cone-Cylinder Shells by F.E.M	Akinori OGAWA	Jan. 1972
TR-263 A Study of Subsonic, Two-Dimensional Wall-Interference Effects in a Perforated Wind Tunnel with Particular Reference to the NAL 2 m × 2 m Transonic Wind Tunnel	Masao EBIHARA	Jan. 1972
TR-264 Flight Control System Design for Launch Vehicle with Liquid Propellant	Hidehiko MORI & Hajime KOSHIISHI	Jan. 1972
TR-265 Fluidic Turbine Inlet Gas Temperature Sensor	Kenji NISHIO, Seiki ENDO & Tokukazu ENDO	Jan. 1972
TR-266 Some Consideration on the Aerodynamic Characteristics for a Body of Rocket with Blunt Nose	Iwao KAWAMOTO	Jan. 1972
TR-267 Aerodynamic Design and Test Result of Front Fans	Shoichi FUJII, Hideo NISHIWAKI, Mitsuo GOMI, Noboru SUGAWARA & Katsumi TAKEDA	Jan. 1972
TR-268T Aerodynamic Design and Test Results of Results of Front Fans	Shoichi FUJII, Hideo NISHIWAKI & Mitsuo GOMI	Jan. 1972
TR-269T Approximation of Linear Operator Semigroups	Tadayasu TAKAHASHI	Feb. 1972
TR-270 The Experiments on the Buckling of Circular Cylindrical Shells	Susumu TODA & Kazuo KUSAKA	Feb. 1972
TR-271 On the Vibration of Three-Parallel-Beams	Yoichi HAYASHI & Tsuneo TSUKIJI	Feb. 1972
TR-272 An Investigation of a Transonic Axial-Flow Turbine (I)—A Cold Air Test of the Annular Turbine Nozzle Cascade—	Tadao TORISAKI, Mitsuo MORITA, Shizuo SEKINE, Hiroyuki NOSE & Shigeo INOUE	Feb. 1972
TR-273 An Investigation of a High Speed Axial-Flow Turbine (II)—A Investigation of a Single Stage Turbine—	Tadao TORISAKI, Mitsuo MORITA, Hiroyuki NOSE, Shizuo SEKINE & Shigeo INOUE	Feb. 1972
TR-274 Investigation of Strength of Axial-Flow Compressor Disc (1 On the Disc with Many Pin Hole)	Katsutoshi MATSUSUE	Feb. 1972
TR-275 Height Control Test Equipment for VTOL Aircraft	Masakatsu MATSUKI, Tadao TORISAKI, Kenji NISHIO, Masanori ENDO, Akira YOSHIDA, Sin NAKAYAMA, Keisuke IWABE, Katsumi TAKEDA, Shizuo SEKINE & Takeshi KOSHINUMA	Feb. 1972

二次噴射推力方向制御の研究

山中龍夫

概要

ロケットの超音速ノズルに2次流体を噴射して推力の方向を制御する技術は，特に固体ロケットにおいて，最近良く使われている。超音速ノズルに2次流体を噴射すると，非常に複雑な主流場の乱れが発生する。2次噴射による推力方向の偏向角度，すなわち，発生制御力を推定するには，この複雑な主流場の乱れに関する十分な知識を必要とする。いままでに，2次噴射による発生制御力を推定する研究は多くなされてきたが，必ずしも，十分な成果が得られていない。これは，いままでの研究がこの複雑な主流場の乱れに関する情報を十分に与えていないためと思われる。すなわち，実際の2次噴射はほとんど円錐流内の現象であるのに実験技術の制約から，いままでの研究がほとんど2次元ノズルによる実験に限られていたからでもある。本論文の目的は，この複雑な主流場の乱れに関して，従来の研究報告よりもさらに詳しい実験資料を提出し，さらに，新しい実験手段による円錐ノズル内の3次元的実験資料を提出することによって，これらの現象を理解するための解析的流体モデルを提示し，これらの実験資料および解析的流体モデルに基づく発生制御力の一推定方法を提出するためのものである。本論文は化学反応を伴わない気体噴射および液体噴射に関する研究であり，四つの章から成り立っている。第1章から第3章までは気体噴射に関するものであり，第4章において，液体噴射の問題点を気体噴射との相異を挙げながら論じている。

第1章においては，2次元ノズルを用いた噴射孔近傍の流れに関する研究について述べている。実際のロケットに起きる現象は，主として，円錐流内の現象であるが，噴射孔近傍の狭い領域のみに限定すれば2次元ノズル内の現象でも十分に実際の現象と類似であると推定できる。主流，2次気体噴流の両方とも空気を用いて，シャドー写真をいくつかの条件について撮影した。その結果，主流場の乱れには二種類あることが判った。一つは，2次噴流がノズル壁上乱流境界層を突き破って十分に主流を横切っていない場合であり，この場合の2次噴流の透過距離は境界層の厚さと同程度であると考えられる。いま一つは，2次噴流が壁上境界層を突き破って十分に主流を横切って透過している場合である。前者については，Mager による乱流境界層のはく離に伴なう斜め衝撃波に関する半実験的解析モデルと良く一致している。後者に関しては，本論文のほとんどがこの後者についての研究であるが，次のような流体モデルを考えた。不足膨張する2次噴流が動圧を受けながら自由膨張し，過膨張してからリーマン波を形成して再圧縮されてから主流と混合する。このとき，自由噴流境界の静圧が変わらないことから噴流境界に沿う流管を想定して，1次元膨張流の等エントロピ変化による静圧降下は，流線の方向を変えることによって相殺され，さらに主流の動圧は噴流境界に沿う流管の曲率による遠心力と平衡を保っているとして，自由噴流境界の軌跡を近似的に求める方法を提示する。この自由噴流境界とリーマン波で形成される樽状噴流が超音速流内に置かれた鈍頭物体と同じ効果を持ち，前流領域に分離衝撃波を生ずる。この分離衝撃波がノズル壁面乱流境界層と干渉する領域では，乱流境界層のはく離に伴う斜め衝撃波を生じている。この斜め衝撃波の斜め角度も Mager の解析と良く一致することが判った。樽状噴流の前流には，超音速の主流と斜め衝撃波を通過する超音速のはく離流があるから，それぞれ，主流方向とはく離流方向に主軸を持ち樽状噴流に内接する楕円球を想定し，Kaattari の行なった超音速流内の楕円球に生ずる分離衝撃波の分離距離と分離衝撃波の曲率半径を求める図式解法を適用して，主流に対する分離衝撃波と斜め衝撃波の生ずるはく離点の位置を求めた。これらの解析的モデルはシャドー写真の結果を良く説明できることが示される。

前にも述べたように，2次噴射推力方向制御が実際のロケットに適用されるのは円錐流に対してであり，主流場の乱れの領域が広い噴射孔後流領域の現象は，2次元ノズルによっる観察結果とは大い

に異なる。そこで，第2章では新しい観測手段を提供することによって，円錐流内の現象を観測して，いままで判らなかった現象を捕捉した。すなわち，平行に入射した平行光線が円錐管内を平行に横切ってから，平行に出て行くような円錐管レンズの原理を述べ，位置ベクトル表示による微分幾何学を応用して，レンズの表面形状を求めるレンズ方程式の厳密解を導いた。このレンズ方程式の解に基づいて円錐管レンズを4個試作した。それらのレンズの性能を示すことによって十分に目的とする現象が捕捉できることを確かめた。噴射孔後流の乱れとは，前流領域の分離衝撃波から続く2次曲面状の衝撃波で囲われた領域で，2次噴射流はこの領域で主流との混合を行なっている。円錐管レンズを用いることによって，この2次曲面状衝撃波の形状を撮影し，さらに，回転型円錐管レンズを用いることによって，この衝撃波形状の展開写真を撮影し，その3次元的形状を捕捉した。また，極超音速気流中の鈍頭物体まわりに生ずる衝撃波形状を求めた Lees 等のブラスト・ウェーブ・アナロジによる計算方法を超音速領域に拡張した計算式から求めた理論形状と撮影された写真とを比較することによって，次のような結論を得た。従来良く使われてきた Hsia 等の，いわゆる，運動量交換モデルに基づく理論よりは，楕状噴流を鈍頭物体と見なしてその主流に対する空気抵抗から計算する理論式の方が円錐ノズル内での実験結果と良く一致する。また，ブラスト・ウェーブ・アナロジを適用する際の回転対称軸は，従来円錐ノズルの場合においては，壁に平行とすべきか，または，ノズル主軸に平行とすべきか議論されてきたところであるが，実験された条件の範囲では，壁に平行に取った方が良いと言うこともこの実験から判った。さらに，回転型円錐管レンズによる衝撃波の展開写真撮影の結果から，2次曲面状の衝撃波の断面は，回転軸対称面のそれではなくて，偏球のそれに近いことも判った。

第1章と第2章において，2次気体噴射によって生ずるロケットのノズル内の乱れの形状は相当十分な精度で予測できることが判った。第3章では，これらの乱れが発生制御力に寄与する領域について，それらの領域の圧力増加分を推定しながら述べている。噴射流の前流領域の乱れは極めて限られた狭い範囲内であるから圧力増加分の実験による測定は行なわれなかったので，各流体モデルに基づく圧力分布の近似的な計算方法を提示するに留めた。噴射孔後流における圧力測定の結果は，気体噴射においては，過膨張と再圧縮の繰り返しのためか圧力増加はほとんど認められなかった。これらの解析的モデルおよび実験結果に基づいた2次気体噴射の場合の発生制御力推定方法を提示し，実際の固体ロケットによる推力方向制御実験を地上の多分力測定装置によって測定した値と比較した。その結果は良い一致を示している。

第4章においては，液体噴射について述べている。液体噴射の場合は，第1章と第2章に述べたような観測実験を行なうには，温度条件を相似させるための困難があるので，ここでは，簡単な液体の噴流モデルを想定して前の第1章と第2章の実験結果と類似であると思われる現象と，液体噴射特有の現象とを区別することによって，発生制御力の推定問題を論じている。流体の噴流に関するモデルが決まれば，前流領域は気体噴射の場合と全く同一と考えることができる。ここで言う，液体噴射特有の問題とは，気体噴射と違って，液体噴流では過膨張と再圧縮と言った過程は存在しないことである。したがって，噴射孔後流の2次曲面状衝撃波による主流の圧縮効果と混合流内の圧力分布は，気体噴射の場合と違って，発生制御力に大きく寄与する。この2次曲面状衝撃波内での圧縮効果を推定するための簡単な流体モデルに基づいた計算方式を考えた。また，実際の固体ロケットにフレオンのごとき液体を2次噴射して，噴射孔後流の圧力増加を測定した値と比較して，液体噴射孔後流においてこのような流体モデルを考えることの妥当性を実験的に確かめた。したがって，液体噴射流と主流場の乱れに関する十分な知識さえあれば，液体2次噴射による発生制御力を気体2次噴射なみに推定することは可能であることを示唆している。

An Investigation of Secondary Injection Thrust Vector Control

By Tatsuo YAMANAKA**

ABSTRACT

Secondary injection thrust vector control (SITVC) of rockets has been in use for sometime. This paper presents an experimental and analytical study on disturbances produced by secondary injection and on an estimation of control forces produced by SITVC. SITVC is done by gas injection or by liquid injection. The control force producing mechanism of gas injection TVC is a little different from that of liquid injection TVC. Most part of the present study is devoted to investigating the disturbances produced by under-expanding gas injection TVC and to presenting an analytical method for estimating control forces of gas injection. Disturbances such as under-expanding gas injection flow, complicated flowfield ahead of injection flow, and leading shock wave in a conical supersonic flowfield are investigated by using two-dimensional cold and dry air flow and by using conical lens method. An analytical model to predict the disturbances induced by secondary gas injection is presented. The comparison of the analysis with the induced disturbed flow is shown in good correlation. Based on the analysis, an estimation of produced control forces by gas injection is tried. The measured control forces produced by secondary gas injection thrust vector control (GITVC) tests, conducted on solid propellant rockets, are compared with the estimated control forces.

Liquid injection thrust vector control (LITVC) also was conducted and the produced control forces were measured by multi components thrusts measuring stand. The regions contributing to the generation of control force of LITVC are discussed by means of an analytical model to predict liquid injectant trajectory. The difference between gas injection and liquid injection is discussed.

INTRODUCTION

It needs much informations of the flowfield induced by secondary injection if one wants to estimate control forces produced by secondary injection thrust vector control (SITVC). Much work has been done to estimate control forces by investigating the complicated flow phenomena associated with such injection[1]~[6], but the estimating methods do not sufficiently well predict the control forces. This may be due to the lack of informations about the complicated interaction processes. The purpose of this investigation is to study, more in detail, the complicated interaction processes and to present an analytical estimating method of the control forces, which is based on an optical observation of the interaction phenomena. Only inert gases and non chemically reactive liquids are considered here as injectants.

In section 1 of the present paper, the disturbances induced by gas injection are discussed by the injection experiment of two-dimensional nozzle flow with a circular injection port. The phenomenon near the injection port can be considered to simulate well the actual flowfield of SITVC in a conical rocket nozzle. The disturbances induced by gas injection have been observed by shadowgraph method. From the optical observation, it is found out that two kinds of disturbances exist. One is such that the penetrating height of an injection flow is almost the same order of the thickness of turbulent boundary layer near the injection port. Another is that, an under-expanding injection flow protrudes deep into rocket nozzle main flow, breaking through boundary layer. The first type of disturbance can be well predicted by Mager's model[7], which is a semi-empirical theory on turbu-

* Received November 6, 1971
** Space Technology Research Group

lent boundary layer separation. As for the second type of disturbance, an analytical model is presented to predict under-expanding injection gas flow, which is being subjected to dynamic pressure of supersonic main flow. Two types of interferences are analysed in the stagnation flowfield ahead of the free jet boundary of injectant, especially about the detached shock distances, the radii, and the separation point. One is the interference between supersonic main flow and injection flow, another is the interference between separated supersonic flow and injection flow.

SITVC of rockets is generally applied to supersonic conical nozzle flow. The experimental results of two-dimensional nozzle flow, especially, leading shocks and mixing flowfield in the downstream of injection port, must be different from those of three-dimensional nozzle flow. Therefore, three-dimensional investigation of secondary gas injection flow is stated in section 2.

Section 2 of the present paper consists of three parts. The first part of the section introduces the conical lens method and presents the derivation of conical lens equations[8]~[9]. Two types of conical lenses were machined and polished. One is called here as simple type and another is called as rotatable type. Three simple type conical lenses were machined and polished for the use of three-dimensional experiment. The performance of these lenses are shown in the second part of section 2. In the last part of section 2, the observed three-dimensional shock waves induced by secondary gas injection, by the use of the conical lens method, are introduced. Because of deteriorating lens performance near the injection port, only leading shocks have been observed. Based on the experimental and analytical study of two-dimensional nozzle flow in section 1, the leading shock waves induced by secondary gas injection into a conical nozzle supersonic flow are compared with the analytical study.

In section 3, an estimating method of control forces produced by secondary gas injection is presented[10]. The method is based on the study of sections 1 and 2. The analytical estimation of produced control forces by the secondary gas injection are compared with the measured control forces, which were conducted by using solid propellant rocket motors on multi-components thrusts measuring stand.

Liquid injection thrust vector control (LITVC) is a little different from gas injection thrust vector control (GITVC) in control force producing mechanism. In section 4, three series of LITVC experiments are introduced. The first is that of high expansion nozzle, and the second and the third are those of sea level expansion nozzles. The LITVC feed system of the third series of test was that of on-board type. A simple analytical treatment for estimating control forces of LITVC is studied.

1. UNDER-EXPANDING SECONDARY GAS INJECTION FLOW AND EXPERIMENT OF TWO-DIMENSIONAL NOZZLE FLOW

Nomenclature

A =area
A_D =frontal area of the jet
a_M =semiminor axis of main ellipsoid
a_s =semiminor axis of separation flow ellipsoid
b_M =semimajor axis of main ellipsoid
b_s =semimajor axis of separation flow ellipsoid
C_D =aerodynamic drag coefficient
D =aerodynamic drag force acting on an infinitesimal length ds
d_N =diameter of injection nozzle at exit
$d_{N\,eff}$ =effective diameter of injection nozzle at exit
d_* =throat diameter of injection nozzle
g =acceleration of gravity
h =width of injection jet stream tube
M =Mach Number
M_j =Mach Number of initial expansion at the injection nozzle exit
M_e =Mach Number of injectant expanded to aft-separation pressure
M_N =Mach Number at injection nozzle exit
M_p =Mach Number of injectant where Riemann wave (the first Mach disc) is standing
M_s =Mach Number of aft-separation flow
M_∞ =Mach Number of free stream
$\dot{m}_j$ =injectant mass flow rate of gases
P =static pressure
P_{c0} =total pressure of main flow
P_{j0} =total pressure of injection gas flow
P_∞ =static pressure of free stream
p $=P/P_{j0}$
q_∞ =dynamic pressure of free stream
R_j =radius of curvature of the jet stream tube
R_{sM} =detached shock radius in front of main ellipsoid
R_{ss} =detached shock radius in front of separation flow ellipsoid
s =trajectory path length of free jet boundary
u_∞ =free stream velocity
v =jet velocity along jet trajectory

v_j =injectant velocity at injection nozzle exit
$\dot{w}_j$ =injectant weight flow rate
x, y =co-ordinates of injectant trajectory
x_p =penetrating length of injectant
Y_s =distance between separation shock apex and detached shock front for main flow
$(\ )_{0M}$ =apex of main ellipsoid
$(\ )_{0s}$ =apex of separated flow ellipsoid
α =over-all flow expansion angle with respect to the x axis
α_N =half angle of rocket nozzle
γ =specific heats ratio of main flow gas
γ_j =specific heats ratio of injectant gas
δ =turning angle across oblique shock
δ_I =injection angle to the cross section of rocket nozzle axis
δ_N =half angle of injection nozzle at exit
δ_s =turning angle of separated flow
Δ_{0M} =shock standoff distance from main ellipsoid
Δ_{0s} =shock standoff distance from separation flow ellipsoid
θ =angle subtracted tangent angle to the jet boundary from the over-all expansion angle
ρ_j =density of the injectant at nozzle exit
ρ_∞ =density of free stream
σ =angle of shock to incoming flow
ω_e =Prandtl-Meyer angle of Mach Number M_e
ω_N =Prandtl-Meyer angle of Mach Number M_N

Subscripts

b =condition along the jet boundary
t =condition along the trajectory of the injected jet axis

The injection of a secondary gas into supersonic flow produces very complicated flowfield near the injection port. The flowfield of this region was observed by using two-dimensional nozzle, whose width was 40 mm, throat length was 10 mm, and nozzle divergent angle was 30°. Injection port was varied from 1 mm to 5 mm in diameter, the expansion ratio at injection from 3.4 to 5.55, the injection angle was 90° to the nozzle axis, and the injection was sonic. Cold and dry air was used for the main flow and injectant. The shadows of the induced disturbances were directly projected to the film (Kodak, TRI-X Pan, 2.25×3.25 in.) by a collimating system. The direct projection was convenient for the comparison with the analysis. Fig. 1.1 shows the test apparatus of two-dimensional nozzle flow. More than one hundred test runs were conducted.

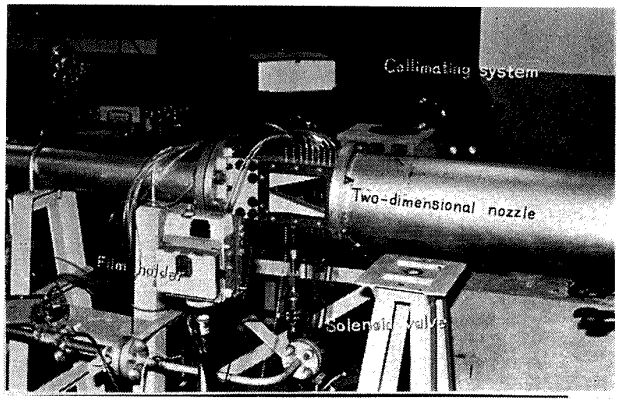

Fig. 1.1 Test apparatus of two-dimensional nozzle.

From the optical observation of the two-dimensional nozzle, it was found out that two-kinds of disturbances existed. One is such that the penetrating height of under-expanding injection flow is almost the same order of the thickness of turbulent boundary layer near the injection port. Fig. 1.2 (a) shows a typical example of the first type. Another is that an under-expanding injection flow protrudes deep into nozzle main flow, breaking through turbulent boundary layer. Fig. 1.2 (b) shows a typical example of the second type.

The separation shock angles and the leading shock angles were measured by the shadowgraphs for various injection conditions. The injection

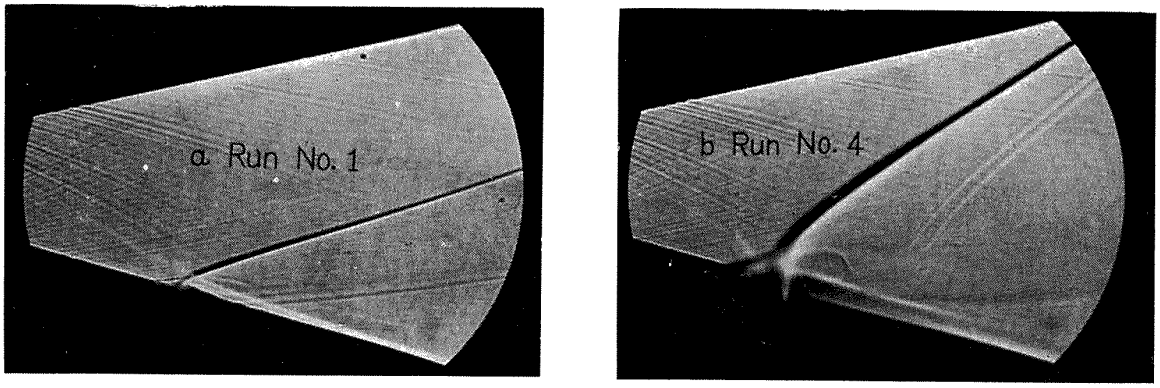

Fig. 1.2 Two types of disturbances induced by gas injection.

Table 1.1 The results of under-expanding air injection into two-dimensional nozzle

Run No.	1	2	3	4	5	6	7	8	9	10	11	12
$P_{c0}=P_{j0}$ ((kg/cm²ab)	16.6	17.1	17.5	17.1	15.4	15.0	14.5	17.5	16.9	16.2	16.9	16.9
M_∞	2.77	2.77	2.77	2.77	3.06	3.06	3.06	3.06	3.28	3.28	3.28	3.28
M_N	1	1	1	1	1	1	1	1	1	1	1	1
M_e	2.34	2.34	2.34	2.34	2.59	2.59	2.59	2.59	2.80	2.80	2.80	2.80
d_N (mm)	1	2	3	5	1	2	3	5	1	2	3	5
d_* (mm)	1	2	3	5	1	2	3	5	1	2	3	5
δ_N (degrees)	0	0	0	0	0	0	0	0	0	0	0	0
δ_1 (degrees)	15	15	15	15	15	15	15	15	15	15	15	15
$\dot{m}_j$ $(Nm^3/s)\times10^{-3}$	2.04	8.14	17.7	41.0	2.08	7.44	15.5	43.0	2.25	7.91	22.0	41.0
$d_{N\,\mathrm{eff}}$ (mm)	0.917	1.81	2.63	4.05	0.962	1.84	2.71	4.10	0.954	1.83	2.98	4.04
δ_s (degrees)	19.1	19.1	19.1	19.1	18.3	18.3	18.3	18.3	17.5	17.5	17.5	17.5
σ (degrees)	38.7	38.7	38.7	38.7	35.3	35.3	35.3	35.3	33.0	33.0	33.0	33.0
M_s	1.88	1.88	1.88	1.88	2.13	2.13	2.13	2.13	2.32	2.32	2.32	2.32
M_p	3.93	3.93	3.93	3.93	4.41	4.41	4.41	4.41	4.80	4.80	4.80	4.80
Ellipsoid (Main)												
$a_M/d_{N\,\mathrm{eff}}$	1.03	1.03	1.03	1.03	1.21	1.21	1.21	1.21	1.39	1.39	1.39	1.39
$b_M/d_{N\,\mathrm{eff}}$	1.62	1.62	1.62	1.62	1.96	1.96	1.96	1.96	2.28	2.28	2.28	2.38
$x_{0M}/d_{N\,\mathrm{eff}}$	0.643	0.643	0.643	0.643	0.942	0.942	0.942	0.942	1.25	1.25	1.25	1.25
$y_{0M}/d_{N\,\mathrm{eff}}$	0.697	0.697	0.697	0.697	0.852	0.852	0.852	0.852	1.04	1.04	1.04	1.04
Ellipsoid (Separated)												
$a_s/d_{N\,\mathrm{eff}}$	0.708	0.708	0.708	0.708	0.793	0.793	0.793	0.793	0.892	0.892	0.892	0.892
$b_s/d_{N\,\mathrm{eff}}$	1.26	1.26	1.26	1.26	1.50	1.50	1.50	1.50	1.74	1.74	1.74	1.74
$x_{0s}/d_{N\,\mathrm{eff}}$	0.268	0.268	0.268	0.268	0.506	0.506	0.506	0.506	0.726	0.726	0.726	0.726
$y_{0s}/d_{N\,\mathrm{eff}}$	0.636	0.636	0.636	0.636	0.786	0.786	0.786	0.786	0.954	0.954	0.954	0.954
$\Delta_{0M}/d_{N\,\mathrm{eff}}$	0.475	0.475	0.475	0.475	0.614	0.614	0.614	0.614	0.696	0.696	0.696	0.696
$R_{sM}/d_{N\,\mathrm{eff}}$	3.34	3.34	3.34	3.34	4.45	4.45	4.45	4.45	5.23	5.23	5.23	5.23
$\Delta_{0s}/d_{N\,\mathrm{eff}}$	0.620	0.620	0.620	0.620	0.701	0.701	0.701	0.701	0.716	0.716	0.716	0.716
$R_{ss}/d_{N\,\mathrm{eff}}$	3.26	3.26	3.26	3.26	4.10	4.10	4.10	4.10	4.48	4.48	4.48	4.48
Penetrating length $/d_{N\,\mathrm{eff}}$	1.31	1.31	1.31	1.31	1.76	1.76	1.76	1.76	2.19	2.19	2.19	2.19
Type of injection flow	I	II	II	II	I	II	II	II	I	II	II	II

conditions of typical twelve test runs are listed in Table 1.1. The measured separation shock angles and leading shock angles of the test runs were compared with the Mager's analysis[7] in Fig. 1.3. The suffix numbers of × marks in Fig. 1.3 show the test run numbers of Table 1.1. Because of two-dimensional nozzle flow, only the shocks very near the injection port were considered here. As far as the phenomenon very near the wall is concerned, it can be said that the phenomenon is hardly affected by the two-dimensional nozzle flow. Fig. 1.3 shows that the first type of separation induced by secondary gas injection agrees well with the oblique shock angles separated by wedge shocks. The separation shock angles of the second type may agree better with the oblique shock angles separated by conical shocks than wedge ones. But the difference may be within 10 degrees. Angles of the leading shock waves with respect to the incoming flow of the second type are far from the Mager's model. Thus, the leading shock of the second type is considered to be produced by a mechanism of flow different from the Mager's model.

As for the second type flowfield, which is of the major interest here, a schematic flow model is considered as shown in Fig. 1.4. The under-expanding injection flow, injected into the upstream by angle of δ_I to the plane perpendicular to rocket nozzle axis, expands and over-expands until it is recompressed with standing Riemann

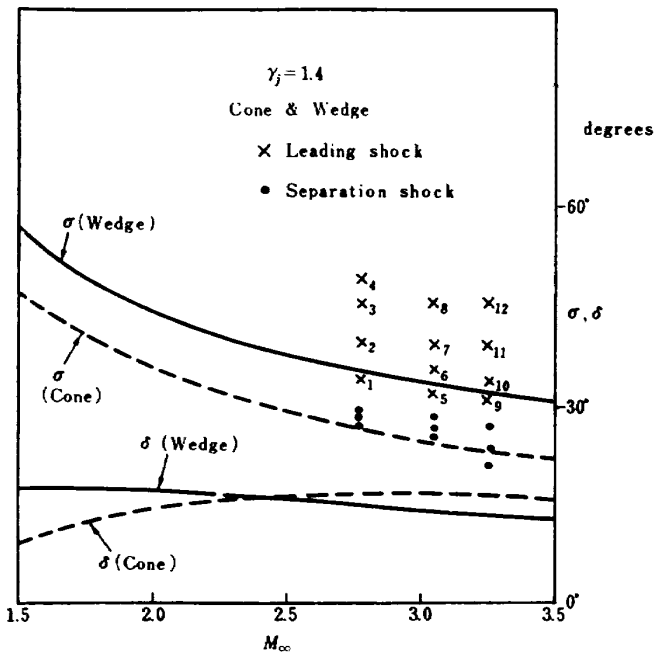

Fig. 1.3 Seperated shock relations of Mager's model and measured shock angles.

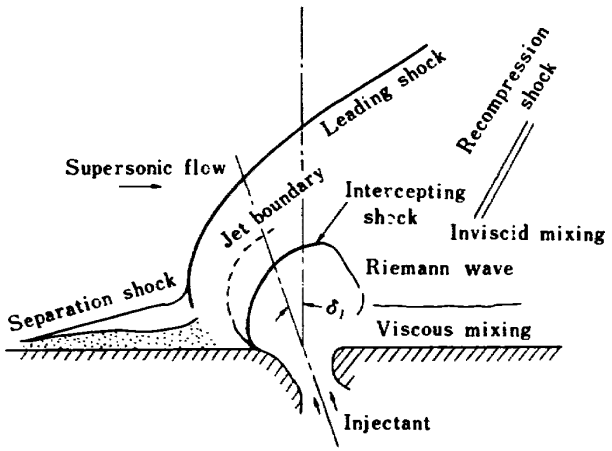

Fig. 1.4 Schematic of typical flow pattern for an under-expanding injection, protruding deep into supersonic main stream, breaking turbulent boundary layer.

wave (the first Mach disc) to the mixing region pressure. During the expanding process, the injection flow is subjected to the dynamic pressure of the supersonic main flow. There have been both experimental and analytical investigations of the under-expanding free jet in recent years. However, there is no method that predicts the under-expanding jet transversely injected into the supersonic main flow in the present study. An approximate analytical model to predict the under-expanding injection gas flow is presented. Fig. 1.5 shows trajectories of the jet boundaries and the jet axes with and without being subjected to the main flow. The axisymmetric ideal

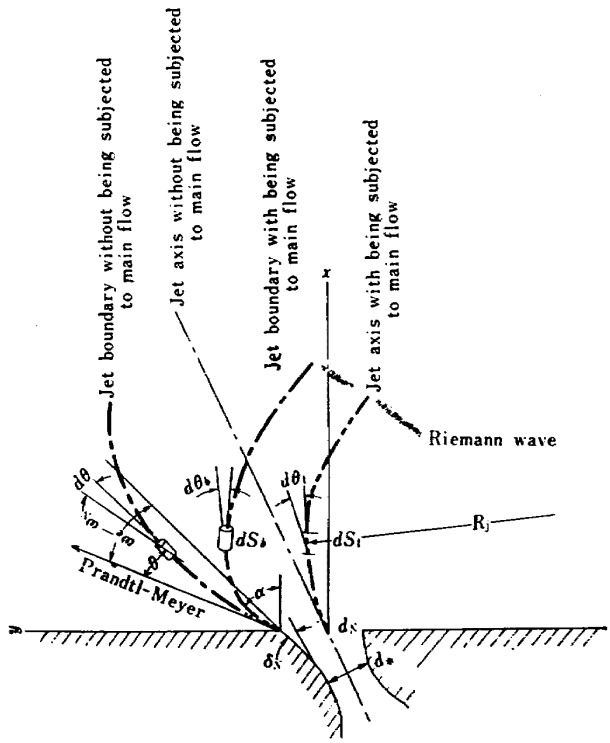

Fig. 1.5 Jet boundaries and jet axes with and without being subjected to main flow.

jet expanding into still air can be calculated by using characteristic theory[25]. This gives a good approximation to the real jet boundary, but it needs a tedious mathematical manipulation. The work involved for calculating the jet boundary for each nozzle and pressure ratio appears to be considerable in practical application. Also, it is still only approximate because a vicous mixing takes place along the boundary and there is some question about continuation of the characteristic net beyond the intercepting shock. Further, to the present flow model shown in Fig. 1.4 such as being subjected to the supersonic main flow, the above mentioned method can not be directly applied.

A simplified theory has been proposed by Adamson et al.[26] of the jet expanding into still air without recourse to the tedious calculation of the characteristic theory. It has been shown that the shape of the jet boundary calculated by the approximate method agrees well with the results of the characteristic theory and the experiment, provided that the expansion is not very high. Here, the same approximation will be applied to the jet injected transversely into the supersonic main flow. Then, it will be shown that the relation between the angle of inclination of the jet boundary and the average Mach Number in the corresponding cross section can be expressed by the same formula as presented by Adamson et al. In order to obtain the shape of

the up-stream side boundary of the jet, the following procedure will be taken in the present study.

First, the mass of the jet is assumed to be concentrated to the jet center-line; consider the balance of the drag and the centrifugal force acting on each element of fluid of the center-line filament; and derive the formula which expresses the curvature of this center-line as function of its angle of inclination, Mach Number and the distance from the nozzle exit. Next, the curvature of the up-stream side boundary is estimated from that of the center-line under a certain simplified assumption. Finally, the shape of this boundary is determined by using the curvature and the relation between the angle of inclination and Mach Number given by the formula of Adamson et al., taking into account the effect of the boundary layer ahead of the injection flow as stated in the later part of this section.

Now, following the argument which has been made by Adamson et al., in the case of the jet into still air, the relation between the angle of inclination and the Mach Number in the corresponding cross section in the case of the jet subjected to the side-wise supersonic flow will be derived. Consider the flow at the lip of an injection nozzle with half angle δ_N and initial angle δ_I between injection direction and transverse direction to the main nozzle axis. At the nozzle lip, before expansion, the Mach Number is M_N and the corresponding Prandtl-Meyer angle is ω_N. After expanding to aft-separation shock pressure, the Mach Number is M_e with a corresponding Prandtl-Meyer angle of ω_e. Thus, the flow at the nozzle lip turns through an angle of $\omega_e-\omega_N$ relative to the injection nozzle wall, and the over-all flow expansion angle with respect to the plane perpendicular to the main flow is α, where

$$\alpha=\omega_e-\omega_N+\delta_N+\delta_I \qquad (1.1)$$

It should be noted that this initial condition of the equation (1.1) exactly corresponds to that obtained by Johannsen et al.[27], who solved the initial curvature of a jet boundary in dealing with the isentropic, irrotational, steady axially-symmetrical flow of a perfect gas in the neighbourhood of the center of such an axial jet expansion by the limiting condition of the polar co-ordinates reducing to the origin.

When an axisymmetrical under-expanding jet expands suddenly around a corner in a wall, it forms a pattern known as a Prandtl-Meyer expansion or centred wave, but is not a simple wave as an uniform two-dimensional supersonic flow. Here, it is assumed that the pressure is maintained constant along the jet boundary, as is the case of the jet into still air. Then, the flow is turned from this initial expansion angle by the intersection of expansion waves with the boundary, reflecting as compression waves, so that the condition of the constant pressure is satisfied. The present approximation depends on replacing the effects of the expansion waves intercepting the flow near the boundary by the effects of a quasi-one-dimensional area increase. Just as in one-dimensional nozzle flow, it is assumed that one can find the average Mach Number and pressure at any axial position in an expanding flow from the area ratio at the given point, instead of going through a characteristic calculation.

Immediately after leaving the injection nozzle exit, then, the flow at the lip has turned through the total angle α. However, as it follows this new direction, it is continually expanding. Hence, in an incremental distance downstream, ds, there is an increase in area, dA, with a corresponding decrease in pressure, $\partial P/\partial A\cdot dA$. $\partial P/\partial A$ can be calculated from quasi-one-dimensional relations if one considers a stream tube along the boundary of the jet to be the channel in question. Since the pressure is assumed to be constant along the jet boundary, this decrease in pressure must be balanced by an equivalent increase in pressure which can only be gained by turning the flow through an incremental angle, $d\theta$, thus forming a weak compression wave. This process of expansion and compression holds at any point on the boundary.

The equation for the pressure along the jet boundary may then be written as follows;

$$dP=0=(\partial P/\partial A)dA+(\partial P/\partial\theta)d\theta \qquad (1.2.a)$$

Since a change in area, dA, is equivalent to a change in Mach Number, dM, in quasi-one-dimensional relations, Eq. (1.2.a) can be written in terms of M and θ. Thus,

$$(\partial P/\partial M)dM+(\partial P/\partial\theta)d\theta=0 \qquad (1.2.b)$$

where $\partial P/\partial M$ is calculated from isentropic flow relations.

Next, if $p=P/P_{j0}$ where P_{j0} is the total pressure for the injection flow along the jet boundary, then Eq. (1.2.b) becomes

$$(\partial p/\partial M)dM+(\partial p/\partial\theta)d\theta=0 \qquad (1.2.c)$$

where P_{j0} is assumed constant along the jet boundary.

For isentropic flow, p is related to M as fol-

lows,

$$p=\left\{1+\frac{\gamma_j-1}{2}M^2\right\}^{-\gamma_j/(\gamma_j-1)} \qquad (1.3.a)$$

so that

$$(\partial p/\partial M)dM=(\partial p/\partial M^2)dM^2 =-\frac{\gamma_j}{2}\frac{pdM^2}{\left\{1+\frac{\gamma_j-1}{2}M^2\right\}} \qquad (1.3.b)$$

From linearized theory, the change in pressure due to a small change in direction is

$$\Delta p=(\gamma_j pM^2/\sqrt{M^2-1})\Delta\theta \qquad (1.4.a)$$

Hence, in terms of a vanishingly small change in pressure and direction

$$\partial p/\partial\theta=\gamma_j pM^2/\sqrt{M^2-1} \qquad (1.4.b)$$

Substituting Eqs. (1.3.b) and (1.4.b) in the constant pressure condition of Eq. (1.2.c), one obtains a differential equation of θ and M.

$$\frac{d\theta}{dM^2}=\frac{\sqrt{M^2-1}}{2M^2\left\{1+\frac{\gamma_j-1}{2}M^2\right\}} \qquad (1.5.a)$$

Letting $\beta=\sqrt{M^2-1}$, integration of the differential equation gives

$$\theta=\sqrt{\frac{\gamma_j+1}{\gamma_j-1}}\,\mathrm{Arctan}\left(\beta\Big/\sqrt{\frac{\gamma_j+1}{\gamma_j-1}}\right)-\mathrm{Arctan}\,(\beta) -\left\{\sqrt{\frac{\gamma_j+1}{\gamma_j-1}}\,\mathrm{Arctan}\left(\beta_e\Big/\sqrt{\frac{\gamma_j+1}{\gamma_j-1}}\right)-\mathrm{Arctan}\,(\beta_e)\right\} \qquad (1.5.b)$$

where $\beta_e=\sqrt{M_e^2-1}$. It should be remarked here that the above formula is the same as that obtained by Adamson et al. for the jet into still air and that some modification of Eq. (1.5.b) is tried in the later part of this section so that the effect of the predominant boundary layer ahead of the injection port may be taken into account.

In order to give a trajectory of the jet boundary without being subjected to the main flow, so called "jet into still air", the average Mach Number at each point on the center trajectory of the jet is given from quasi-one-dimensional isentropic flow relations. Therefore, an approximate boundary is given by Eqs. (1.5)[26]. In the present flow model, since the jet is subjected to the dynamic pressure of the main flow, its effect must be taken into account. Because there is no analytical method to predict the present flow model, the center trajectory of such jet is investigated first. Consider the forces acting on an infinitesimal length ds_t of the jet stream along the center trajectory. Here, only the balancing forces normal to the jet axis will be considered. Then, if the mass of the jet stream element of ds_t is considered to be centred on the trajectory, balancing forces acting on an element in a direction perpendicular to the stream tube axis,

$$D-mg\sin(\delta_I-\theta_t)=mv^2/R_j \qquad (1.6)$$

where $v=v(s_t)$ is the local jet velocity, $R_j=R_j(s_t)$ is the radius of curvature of the jet stream tube center-line, D is aerodynamic drag acting on the jet and θ_t is a deflection angle of the jet from the initial angle. Thus, $ds_t=R_j d\theta_t$, and $D\equiv C_D(\delta_I-\theta_t)q_\infty\cos^2(\delta_I-\theta_t)hds_t$, where h is the width of the jet stream tube measured in the plane perpendicular to the plane in the sketch in Fig. 1.5.

Neglecting the gravity force compared to the drag and the centrifugal force, and with the assumption, Eq. (1.6) becomes

$$\frac{d\theta_t}{d\bar{s}_t}=\frac{C_D(\delta_I-\theta_t)\cos^2(\delta_I-\theta_t)(h/d_N)}{\frac{\pi M}{2M_j}\sqrt{\frac{1+\frac{\gamma_j-1}{2}M_j^2}{1+\frac{\gamma_j-1}{2}M^2}}}\left(\frac{\rho_\infty u_\infty^2}{\rho_j v_j^2}\right) \qquad (1.7)$$

where $\bar{s}_t=s_t/d_N$, ρ_∞ and u_∞ are the density and the velocity of the main stream, respectively, and ρ_j and v_j are the density and the velocity of the injectant at nozzle exit, and M_j is the corresponding Mach Number at the nozzle exit.

Assuming that each element of the jet acts as an element of an infinite cylinder aligned at the local angle to the flow, experimental data are available for this situation, and the following curve fits are taken as an adequate representation of these data by Schetz[11]:

$$C_D=1.2+\{M_\infty\cos(\delta_I-\theta_t)\}^{7/2},\quad 0<M_\infty\cos(\delta_I-\theta_t)\leq 1 \qquad (1.8.a)$$

$$C_D=1.06+1.14\{M_\infty\cos(\delta_I-\theta_t)\}^{-3},\quad M_\infty\cos(\delta_I-\theta_t)\geq 1 \qquad (1.8.b)$$

where M_∞ is the Mach Number of the main flow.

Eq. (1.7) shows the curvature of the jet stream center-line with being subjected to the dynamic pressure of the main flow. The parameters are trajectory pass length, ds_t, tangent angle to the x axis, $\delta_I-\theta_t$, width of the jet stream, h and average Mach Number of the jet at that point. From subsonic experiments, Abramovich[12] suggests that the shape of the cross section may be taken as an ellipse with a ratio of the major to the minor axes of 5 to 1, and the width of such jet stream is approximately given

$$h/d_N=2.25+0.22\bar{s}_t \qquad (1.9)$$

Now, the initial angle condition of the jet boundary stream (1.1), the jet boundary condition of θ_b and average Mach Number M of Eqs. (1.5) to give constant static pressure level, and the curvature equation (1.7) of the jet center-line are given. If the curvature of the jet boundary trajectory were equal to that of the jet center-line of Eq. (1.7), then the shape of the jet boundary would be easily given. However, such condition will be satisfied only at the far downstream of the jet flow. Therefore, the curvature of the jet boundary is investigated from the analogy of that of the jet center-line, in reviewing of the flow model of Fig. 1.4.

Eq. (1.7) can be rewritten as follows;

$$\frac{d\theta_t}{d\bar{s}_t}=C_D(\delta_I-\theta_t)\cos^2(\delta_I-\theta_t)\bar{h}(\bar{s}_t)\times\sqrt{\frac{\gamma_j-1}{2}+\frac{1}{M^2}}\left\{\frac{M_j\left(\frac{\rho_\infty u_\infty^2}{\rho_j v_j^2}\right)}{\frac{\pi}{2}\sqrt{1+\frac{\gamma_j-1}{2}M_j^2}}\right\}$$

where { } is constant if GITVC condition is given, hence

$$\frac{d\theta_t}{d\bar{s}_t}\propto C_D(\delta_I-\theta_t)\cos^2(\delta_I-\theta_t)\bar{h}(\bar{s}_t)\sqrt{\frac{\gamma_j-1}{2}+\frac{1}{M^2}}$$

It means that, the curvature of the jet center-line with being subjected to the dynamic pressure of the main flow, $(d\theta_t/d\bar{s}_t)$, is proportional to a separable variables type function of $(\delta_I-\theta_t)$, $\bar{s}_t$, and average Mach Number M, if these are considered as independent ones. However, θ_t is dependent variable of M as seen from Eq. (1.5), and $\bar{s}_t$ also is related to θ_t and M. As far as the problem is limited to the jet flow down to the first Riemann wave (Mach disc) in the present GITVC problem, one can approximately consider as $\bar{s}_t\simeq\bar{s}_b$, and the average Mach Number of the jet boundary stream is nearly equal to that of the jet stream, where $\bar{s}_b$ is trajectory pass length along the jet boundary stream. If it is supposed that the curvature of the jet boundary has the similar proportionality from the analogy of that of the jet center-line trajectory, the difference may result from only angle of the jet boundary stream to the main flow, then

$$\frac{d\theta_b}{d\bar{s}_b}\propto C_D(\alpha-\theta_b)\cos^2(\alpha-\theta_b)\bar{h}(\bar{s}_b)\sqrt{\frac{\gamma_j-1}{2}+\frac{1}{M^2}}$$

If generally used GITVC conditions are considered, $90°>\alpha\gg\delta_I$ at the lip of the injection nozzle exit. As $\alpha-\theta_b\gg\delta_I-\theta_t$ near the lip flow, the following inequality is validly obtained:

$(d\theta_b/d\bar{s}_b)<(d\theta_t/d\bar{s}_t)$; near the lip flow.

The jet stream will be strongly subjected to the dynamic pressure of the main flow near the apex of the jet boundary shape to the main flow direction until the first Riemann wave position. Therefore, the shape of the cross section of the jet stream will be approximately similar to that of Abramovich's ellipse in this region. The general GITVC condition gives approximately $x_p<2d_N$, and $M_p<4.8$, where x_p and M_p are position and Mach Number of the first Riemann wave, respectively. The distance between the boundary and the jet axis at the first Riemann wave position is smaller than $2d_*$, if Abramovich's ellipse is considered. It suggests that the curvature of the boundary becomes larger than that of the jet stream center-line in the jet downstream region of after protrusion through the separated flow, as

$(d\theta_b/d\bar{s}_b)>(d\theta_t/d\bar{s}_t)$; near the apex of the jet boundary.

Both curvatures will finally approach to the same value after being subjected to the above inequalities. If the limiting condition is considered, then

$$\lim(d\theta_t/d\bar{s}_t)=\lim(d\theta_b/d\bar{s}_b)$$

$$(\delta_I-\theta_t)\to-(90°-\varepsilon)\qquad(\alpha-\theta_b)\to-(90°-\varepsilon)$$

where $0<\varepsilon\ll 90°$.

Because of the above limiting condition, the constants of both proportional relations should be equal. Therefore, the curvature of the jet boundary of the present flow model can be approximately expressed by Eq. (1.7) by replacing $(\delta_I-\theta_t)$ into $(\alpha-\theta_b)$ and $\bar{s}_t$ into $\bar{s}_b$, as

$$\frac{d\theta_b}{d\bar{s}_b}\cong\frac{C_D(\alpha-\theta_b)\cos^2(\alpha-\theta_b)\bar{h}(\bar{s}_b)}{\frac{\pi}{2}\frac{M}{M_j}\sqrt{\frac{1+\frac{\gamma_j-1}{2}M_j^2}{1+\frac{\gamma_j-1}{2}M^2}}}\left(\frac{\rho_\infty u_\infty^2}{\rho_j v_j^2}\right) \qquad (1.10)$$

The general GITVC condition gives actually $\alpha=25°\sim45°$, $\delta_I\geqq 0°$, then the above mentioned inequalities of both curvatures are satifished in the present region by Eqs. (1.7) and (1.10).

Here, one should mention about the unspecified quantity of the initial condition of the jet, M_j, at the nozzle exit. In the case of the present flow model, there exists the predominant boundary layer ahead of the injection flow. Therefore, the relation of Adamson et al., Eq. (1.5.b), can not be directly substituted into Eq. (1.10). It is to say that the initial condition of

the jet is not M_e but has a little lower value than M_e, because of the effect of the boundary layer. A simplified assumption of $M_e=M_j$ is used in Eq. (1.5.b), while holding the relation of the initial flow direction of the up-stream side jet boundary of Eq. (1.1), in the present study, and also $M_j=M_N$ according to a conclusion of many trial and error calculations of the present jet boundary trying to match the results of the later introduced two-dimensional flow visualization. This means that the initial expansion of the jet may be restrained by the boundary layer. Thus, the initial Mach Number in the turning portion of the jet boundary is taken as; $M_j=M_N$ in Eqs. (1.5) and (1.10). Therefore, letting $\bar{s}_b\equiv\bar{s}$ and $\theta_b\equiv\theta$, substituting Eqs. (1.5), (1.8) and (1.9) into Eq. (1.10), and integration gives an approximate trajectory of the present up-stream side jet boundary as

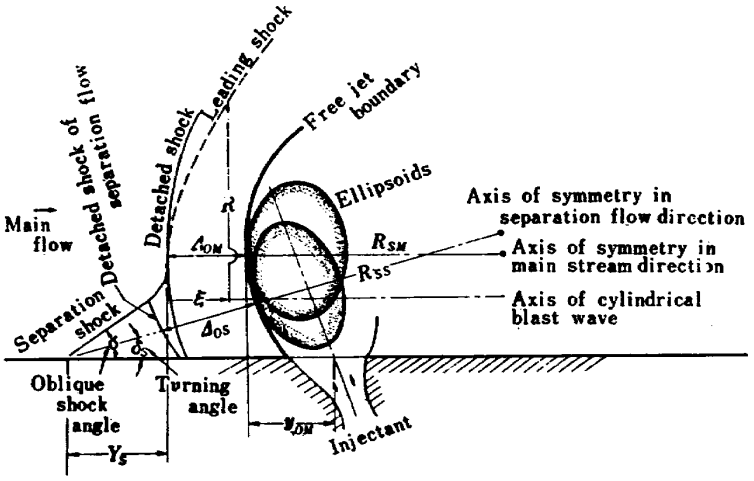

Fig. 1.6 Analytical model for describing flowfield ahead of injection flow.

$$\bar{s}^2+20.45\bar{s}\cong\frac{\pi}{0.44}\frac{\gamma+1}{\gamma}\gamma_j\frac{P_{j0}}{P_{c0}}M_N\times\frac{\left(1+\frac{\gamma-1}{2}M_\infty^2\right)^{1/(\gamma-1)}}{\left(1+\frac{\gamma_j-1}{2}M_N^2\right)^{(\gamma_j+1)/2(\gamma_j-1)}}\times\int_{M_N}^{M}\frac{\frac{\sqrt{M^2-1}}{\left(1+\frac{\gamma_j-1}{2}M^2\right)^{3/2}}}{C_D(\alpha-\theta)\cos^2(\alpha-\theta)}dM \tag{1.11}$$

where P_{c0} is the total pressure of the main flow, γ is the specific heats ratio of the main flow, and M_∞ is Mach Number of undisturbed supersonic main flow.

Assuming that the jet boundary is enveloped by the stream tube, of which circular cross section corresponds to a situation of Mach Number, M, Eqs. (1.1)-(1.11) with the assumption, predict the jet boundary and the intercepting shock as an envelope of right running characteristic. The under-expanding jet expands along the jet stream and further the jet over-expands until the first Riemann wave stands and is recompressed to the mixing region pressure, the jet can be considered as a valid obstruction to the supersonic main flow. The length, from the injection nozzle exit to the first Riemann wave, may be here called the penetrating length of gas injection. The generation of the leading shock wave and the separation shock wave will be induced by this obstruction. In order to predict the complicated flowfield ahead of the injection flow, two ellipsoids are approximately considered. They are inscribed the jet boundary as shown in Fig. 1.6.

The symmetrical axes of two inscribed ellipsoids are directed to the main flow and the separated flow, respectively. The ellipsoid is approximately determined by the jet circular cross sectional area. Its radius, r, is calculated from quasi-one-dimensional isentropic relations. At each axis intersecting point, $a=r$, $b=\sqrt{r\cdot R_j}$, where a and b are the semiminor axis and the semimajor axis of the ellipsoid, respectively, and R_j is the radius of curvature. The graphical method to describe the detached shock shapes for the ellipsoids at zero angle of attack, presented by Kaattari[13] was applied to the present study. The shock standoff distance from the main ellipsoid, Δ_{0M}, the shock radius on axis of symmetry in the main stream direction, R_{sM}, and the separation flow detached shock standoff distance from body, Δ_{0s}, the separation flow shock radius on axis of symmetry in the separation flow direction, R_{ss}, were calculated. The separation condition was calculated from Mager's model.

The calculated parameters of the injection flow, detached shock standoff distances and radii, and separation conditions of the experiment are listed in Table 1.1. Actually, d_N in Eqs. (1.9), (1.10), and (1.11) was calculated by $d_{N\,\mathrm{eff}}$ from the measured weight flow rate, $\dot{w}_j$, as $d_{N\,\mathrm{eff}}=(4\dot{w}_j/\pi\rho_j v_j)^{1/2}$. The flow rate of the injectant was measured by orifice flow meter with quadrant nozzle, which was calibrated by gas meter of 50 Nm³/hr (Shinagawa Seisakusho).

The comparison with the shadowgraphs are shown in Fig. 1.7.

The leading shock shapes also were calculated by applying cylindrical blast wave analogy, here

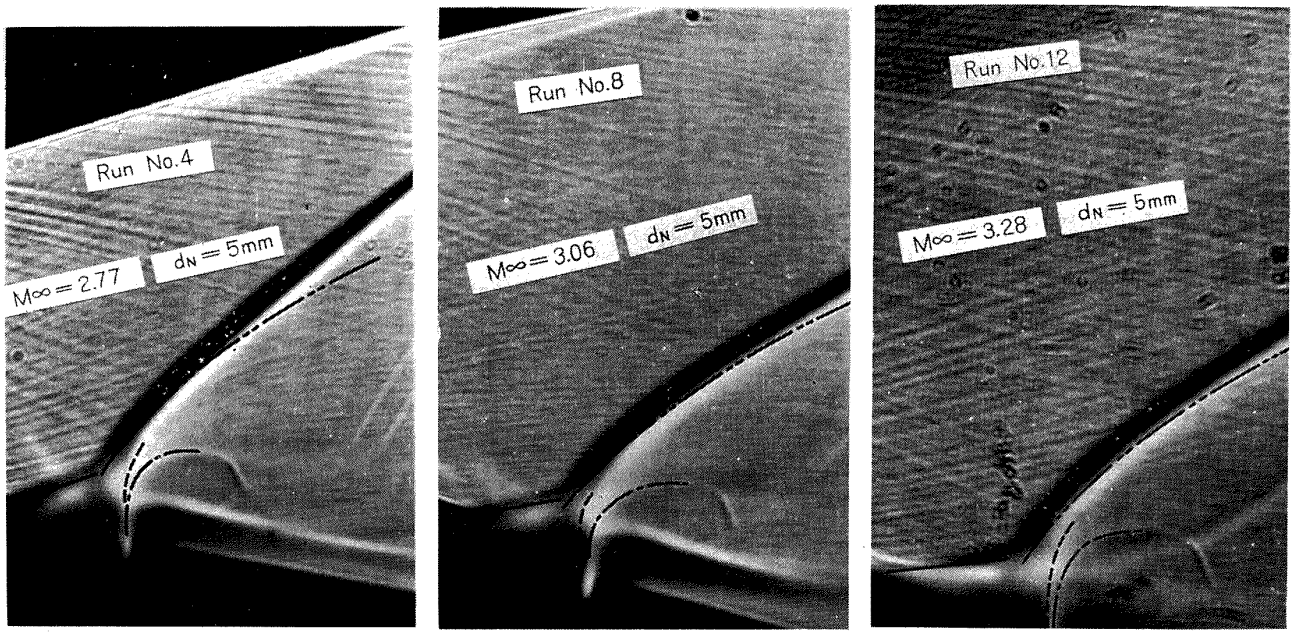

Fig. 1.7 Disturbed flowfield ahead of injection flow and comparison with analysis.

axis of cylindrical blast wave was taken parallel to the nozzle wall[9] and the apex of leading shock wave was set at the intersecting point of the main detached shock and an axis parallel to the nozzle wall through the symmetrical point of the separation flow ellipsoid (see Fig. 1.6). The leading shock shapes will be discussed more in detail in the next section. Although the phenomena occur in the limited small region, these calculations may be concluded to agree well with the experimental results.

2. THREE-DIMENSIONAL INVESTIGATION OF SECONDARY GAS INJECTION FLOW BY THE USE OF CONICAL LENS METHOD

Nomenclature

A_∞ =cross sectional area of rocket nozzle at injection
a_M =semiminor axis of main ellipsoid
b_M =semimajor axis of main ellipsoid
d_b =diameter of blunt nose
d_N =diameter of injection nozzle exit
$d_{N\mathrm{eff}}$ =effective diameter of injection nozzle at exit
d_* =throat diameter of injection nozzle
$(\boldsymbol{e}_1, \boldsymbol{e}_2, \boldsymbol{e}_3)$=fundamental unit vectors
H =axial length of injection port location
J =nondimensional constant
L =axial length of conical lens
l, m, n=directional cosines of the refracted ray in the lens wall
M_e =Mach Number of injectant to expand aft-separation pressure
M_N =Mach Number at injection nozzle exit
M_p =Mach Number of injectant where Riemann wave is standing
M_s =Mach Number of aft-separation flow
M_∞ =Mach Number of free stream
$\dot{m}_j$ =injectant mass flow rate
$\dot{m}_0$ =main stream mass flow rate
n_λ =refractive index of the lens material
R =cylindrical blast wave radius
R_{SM} =detached shock radius in front of main ellipsoid
R_* $=(\dot{m}_j/\dot{m}_0 \cdot u_e/u_\infty \cdot A_\infty)^{1/2}$
r_M =maximum inner radius of conical lens
r_0 =minimum inner radius of conical lens
$\boldsymbol{r}_1$ =unit vector of the incident ray passing through a point P, (1, 0, 0).
$\boldsymbol{r}_1'$ =unit vector of the refracted ray passing through the point P, (l, m, n).
S =distance between screen position and conical lens
S_1 =surface of leading shock
S_2 =separation front
$t-\phi$ =parameters of cylindrical co-ordinates for inner surface of conical lens
u_e =axial component of the velocity at the rocket nozzle exit in the absence of injection.
u_∞ =axial component of the free stream velocity at injection point
$\mathfrak{X}$ =position vector of outer surface of conical lens
$\mathfrak{x}$ =position vector of inner surface of conical lens

$\mathfrak{r}_1$ $=(x=x,\ y=y_1,\ z=z_1)$ position vector of a ray in the bore parallel to x axis

$\mathfrak{r}_1'$ $=(x=x_1+ls,\ y=y_1+ms,\ z=z_1+ns)$ position vector of the refracted ray in the lens wall

$(x, y)_{0M}$ =apex of main ellipsoid

$(x, y)_{0s}$ =apex of separated flow ellipsoid

Y_s =distance between separation shock apex and detached shock front for main flow

α_N =half angle of rocket nozzle

γ =specific heats ratio of main flow gas

Δ_{0M} =shock standoff distance from main ellipsoid

δ_I =injection angle to the plane perpendicular to rocket nozzle axis

δ_N =half angle of injection nozzle at exit

δ_s =turning angle of separated flow

ζ =ray path length in the lens wall

ζ_0 =ray path length in the lens wall at $\phi=0$

λ =nondimensional constant

ξ =axial distance from apex of cylindrical blast wave analogy

Ω =injection angle to the transverse plane of the incoming parallel light rays

SITVC of rocket is generally applied to supersonic conical flow. The actual flowfield, in that case, especially the leading shocks and the mixing flowfield in downstream, is different from that of two-dimensional nozzle flow. Much work has been done to investigate the phenomena associated with such injection, the flowfield produced is still not well understood. With regard to secondary injection problems, optical observation has been used as a powerful method for investigation. However, all of the studies reported to date have been worked out by using two-dimensional nozzle flow[14]~[18].

A conical lens method developed by the author[8],[9], for observing phenomena in a conical pipe flowfield such as rocket nozzle, has been introduced in this section. Two types of conical lens, which are made of schlieren glass, have been machined and polished. One is called here as simple type. Three lenses of this type were machined and polished. Another is called here as rotatable type. One lens of this type was machined and polished. Optical performance of these lenses had been investigated before three-dimensional investigation of secondary gas injection flowfield was conducted.

The secondary gas injection produces very complicated flowfield very near the injection port as stated in the previous section. Because of deteriorating lens performance near the injection port, only leading shocks were observed by the conical lens method. Based on the experimental and analytical study of two-dimensional nozzle flow presented in the previous section, the leading shock waves induced by secondary gas injection into a conical nozzle supersonic flow, through the orifice at sonic velocity vertical to the nozzle axis, were observed and compared with analysis in the last part of this section.

2.1. Derivation of Conical Lens Equations

The principle of conical lens method is schematically shown in Figs. 2.1 and 2.2. Fig. 2.1 shows a cross-sectional view of an ordinary pipe of transparent wall, where the incoming parallel

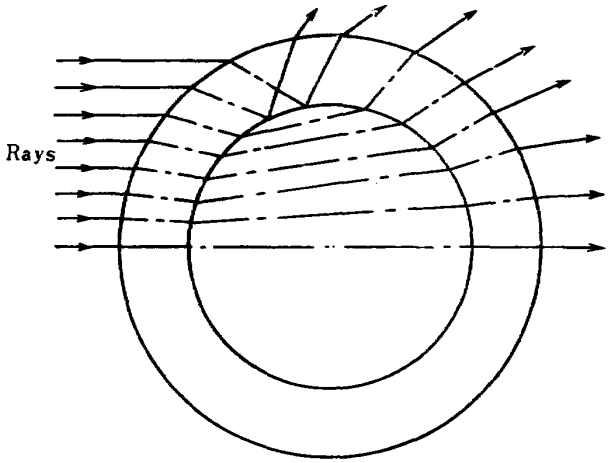

Fig. 2.1 Dispersion of incoming parallel rays through ordinary pipe of transparent wall.

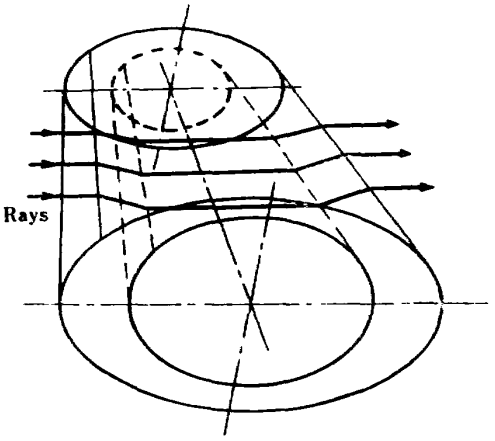

Fig. 2.2 Parallel rays through conical lens.

light rays are being dispersed due to refraction or reflection on the outer and inner surfaces. Fig. 2.2 shows a conical lens. The inner surface is conical and the outer surface is generated such that the incoming parallel light rays go parallel through the bore by compensating one another at twice refractions on the outer and the inner surfaces, and go out parallel by the same refractions. Using differential geometry

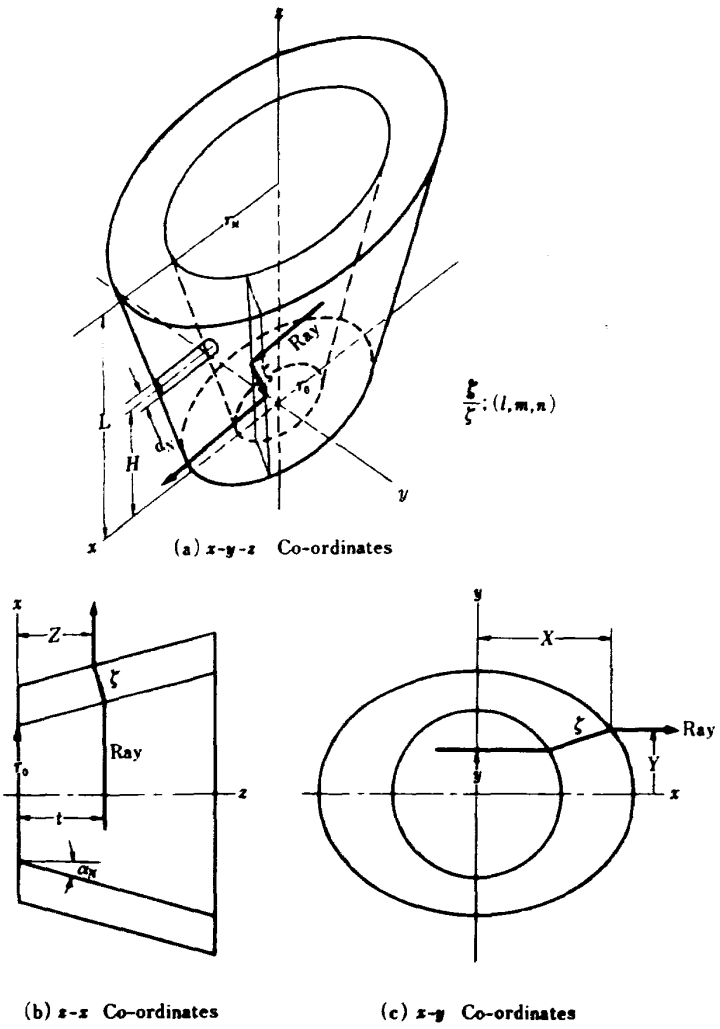

Fig. 2.3 Conical lens co-ordinates

and vector analysis, conical lens equations have been derived. Co-ordinates of the lens equations are shown in Fig. 2.3.

The position vector, $\mathfrak{x}$, of the inner conical surface is given by

$$\mathfrak{x}: \quad \left.\begin{aligned} x&=(r_0+t\tan\alpha_N)\cos\phi\,,\\ y&=(r_0+t\tan\alpha_N)\sin\phi\,,\\ z&=t \end{aligned}\right\} \qquad (2.1)$$

where α_N is cone half angle, r_0 is a reference inner radius of conical surface and t and ϕ are curvilinear co-ordinates of the surface.

The differential geometry gives the first fundamental quantities of the inner surface as

$$\left.\begin{aligned} E&=\mathfrak{x}_\phi\cdot\mathfrak{x}_\phi=(r_0+t\tan\alpha_N)^2\,,\\ F&=\mathfrak{x}_\phi\cdot\mathfrak{x}_t=0\,,\\ G&=\mathfrak{x}_t\cdot\mathfrak{x}_t=1+\tan^2\alpha_N \end{aligned}\right\} \qquad (2.2)$$

and

$$g=EG-F^2=(1+\tan^2\alpha_N)(r_0+t\tan\alpha_N)^2 \qquad (2.3)$$

where $\mathfrak{x}_\phi=\partial\mathfrak{x}/\partial\phi$ and $\mathfrak{x}_t=\partial\mathfrak{x}/\partial t$ express tangent vectors to the ϕ-curve and the t-curve at a point (ϕ, t), respectively. The unit normal vector at this point $(\mathfrak{x})_N$ is

$$\begin{aligned}(\mathfrak{x})_N&=\mathfrak{x}_\phi\times\mathfrak{x}_t/\sqrt{g}\\ &=\cos\alpha_N(\cos\phi e_1+\sin\phi e_2-\tan\alpha_N e_3)\end{aligned} \qquad (2.4)$$

where e_1, e_2, and e_3 are the fundamental unit vectors. The analysis deals with only the half path of a light ray for simplicity.

An arbitrary position vector $\mathfrak{x}_1$, which expresses the path of a ray traversing perpendicularly to the bore axis and passing through an arbitrary point $P(x_1, y_1, z_1)$ on the inner surface is given by

$$\mathfrak{x}_1(x, y_1, z_1)\,, \qquad x^2+y_1^2<(r_0+z_1\tan\alpha_N)^2 \qquad (2.5)$$

The position vector, $\mathfrak{x}_1'$, of the path of the refracted light ray, after it passed through the point P, is given by

$$\mathfrak{x}_1'(x=x_1+ls,\ y=y_1+ms,\ z=z_1+ns) \qquad (2.6)$$

where l, m, and n are the directional cosines of the position vector $\mathfrak{x}_1'$ and s is a parameter. Snell's law determines the relations among $\mathfrak{x}_1$, the normal vector at the point P on the inner surface $[\mathfrak{x}(P)]_N$, and $\mathfrak{x}_1'$ as follows:

Scalar product of two vectors gives

$$\cos\theta_A=[\mathfrak{x}(P)]_N\cdot r_1=\cos\alpha_N\cos\phi \qquad (2.7)$$

$$\begin{aligned}\cos\theta_B&=[\mathfrak{x}(P)]_N\cdot r_1'\\ &=\cos\alpha_N(l\cos\phi+m\sin\phi-n\tan\alpha_N)\end{aligned} \qquad (2.8)$$

where r_1 and r_1' represent the unit vectors $r_1(1, 0, 0)$ of the incident ray expressed by the position vector $\mathfrak{x}_1$ and $r_1'(l, m, n)$ of the refracted ray expressed by the position vector $\mathfrak{x}_1'$, respectively, and θ_A and θ_B are angles between $[\mathfrak{x}(P)]_N$ and r_1, and $[\mathfrak{x}(P)]_N$ and r_1', respectively.

Because the two planes defined by vector products $[\mathfrak{x}(P)]_N\times r_1$ and $[\mathfrak{x}(P)]_N\times r_1'$ should be parallel, one obtains after comparing components of the two vector products $[\mathfrak{x}(P)]_N\times r_1$ and $[\mathfrak{x}(P)]_N\times r_1'$, and using the relationship $l^2+m^2+n^2=1$ and Eq. (2.8)

$$\left.\begin{aligned} l&=\cos\alpha_N\cos\phi\cos\theta_B\\ &\quad+(1-\cos^2\alpha_N\cos^2\phi)\left(\frac{1-\cos^2\theta_B}{1-\cos^2\alpha_N\cos^2\phi}\right)^{1/2}\\ m&=\cos^2\alpha_N\sin\phi\cos\phi \end{aligned}\right\}$$

$$\times\left\{\frac{\cos\theta_B}{\cos\alpha_N\cos\phi}-\left(\frac{1-\cos^2\theta_B}{1-\cos^2\alpha_N\cos^2\phi}\right)^{1/2}\right\}\Bigg\}$$

$$n=-\sin\alpha_N\cos\alpha_N\cos\phi$$

$$\times\left\{\frac{\cos\theta_B}{\cos\alpha_N\cos\phi}-\left(\frac{1-\cos^2\theta_B}{1-\cos^2\alpha_N\cos^2\phi}\right)^{1/2}\right\}\Bigg\} \tag{2.9}$$

The refractive index n_λ of the lens material is defined by

$$n_\lambda=\sin\theta_A/\sin\theta_B \tag{2.10}$$

Combining Eqs. (2.7) and (2.10), one obtains

$$\cos\theta_B=(n_\lambda^2-1+\cos^2\alpha_N\cos^2\phi)^{1/2}/n_\lambda \tag{2.11}$$

Letting Q be a point at which the refracted light ray passes the outer surface of the lens, one obtains the position vector $\mathfrak{x}(Q)$ of Q as

$$\mathfrak{x}(Q)=\mathfrak{x}(P)+\zeta\cdot\boldsymbol{r}_1' \tag{2.12}$$

where ζ is a distance between P and Q.

Because the light ray leaving Q should be parallel to the incident light ray vector $\boldsymbol{r}_1$, the normal vectors at the point P of $\mathfrak{x}$ and at the point Q of $\mathfrak{X}$ should be parallel. One obtains thus

$$[\mathfrak{X}(Q)]_N\times[\mathfrak{x}(P)]_N=0 \tag{2.13.a}$$

Rewriting gives

$$\{[\mathfrak{X}(Q)]_\phi\times[\mathfrak{X}(Q)]_t\}\times[\mathfrak{x}(P)]_N=0 \tag{2.13.b}$$

The triple product of the vectors gives

$$\{[\mathfrak{x}(P)]_N\cdot[\mathfrak{X}(Q)]_\phi\}\cdot[\mathfrak{X}(Q)]_t-\{[\mathfrak{x}(P)]_N\cdot[\mathfrak{X}(Q)]_t\}\cdot[\mathfrak{X}(Q)]_\phi=0 \tag{2.14}$$

Because $[\mathfrak{X}(Q)]_\phi$ and $[\mathfrak{X}(Q)]_t$ are independent vectors, each scalar product of Eq. (2.14) vanishes, thus one obtains

$$\left.\begin{aligned}[\mathfrak{x}(P)]_N\cdot[\mathfrak{X}(Q)]_\phi=0\\ [\mathfrak{x}(P)]_N\cdot[\mathfrak{X}(Q)]_t=0\end{aligned}\right\} \tag{2.15.a}$$

Rewriting gives

$$\left.\begin{aligned}[\mathfrak{x}(P)]_N\cdot[\partial(\zeta\boldsymbol{r}_1')/\partial\phi]=0\\ [\mathfrak{x}(P)]_N\cdot[\partial(\zeta\boldsymbol{r}_1')/\partial t]=0\end{aligned}\right\} \tag{2.15.b}$$

Equations (2.15.b) are partial differential equations of ζ. Suppose ζ is separable:

$$\zeta=\xi(\phi)\eta(t)$$

One can see easily that ζ is a function of only ϕ from the second equation of (2.15.b). Integration of the first differential equation of (2.15.b) gives

$$\frac{\zeta}{\zeta_0}=\frac{\sqrt{n_\lambda^2-\sin^2\alpha_N}\,(\cos\alpha_N\cos\phi+\sqrt{n_\lambda^2-1+\cos^2\alpha_N\cos^2\phi}\,)}{\sqrt{n_\lambda^2-1+\cos^2\alpha_N\cos^2\phi}\times(\cos\alpha_N+\sqrt{n_\lambda^2-\sin^2\alpha_N}\,)} \tag{2.16}$$

where $0<\phi<\pi/2$ because of symmetrical property of the surface. One obtains, finally, the required surface for a given conical surface of $\mathfrak{x}$, which can be expressed by the following position vector:

$$\mathfrak{X}(\phi,t)=\mathfrak{x}(\phi,t)+\zeta(\phi)\boldsymbol{r}_1'(\phi) \tag{2.17}$$

in rectangular co-ordinates

$$\left.\begin{aligned}X&=(r_0+t\tan\alpha_N)\cos\phi+\zeta l\\ Y&=(r_0+t\tan\alpha_N)\sin\phi+\zeta m\\ Z&=t+\zeta n\end{aligned}\right\} \tag{2.17'}$$

2.2. Conical Lenses and Optical Calibration of the Lenses

The conical lens equation of (2.17) is a ruled surface of which generating lines pass through a closed guiding curve. Therefore, it is easy for machining and polishing. Four lenses have been machined and polished. They have been made

Table 2.1 Measured refractive indexes of lens material

Material: BSC-7, best annealed, NIKON

Wave length (mμ)	Refractive index
404.7 (*Hg, h*)	1.5302 (n_h)
435.8 (*Hg, g*)	1.5266 (n_g)
486.1 (*H, F*)	1.5223 (n_f)
546.1 (*Hg, e*)	1.5187 (n_e)*
587.6 (*He, d*)	1.5168 (n_d)
656.3 (*H, C*)	1.5143 (n_c)
768.2 (*K, A'*)	1.5114 ($n_{A'}$)

* Designed, measuring accuracy ±0.0005.
Presented by Nippon Kogaku K.K.

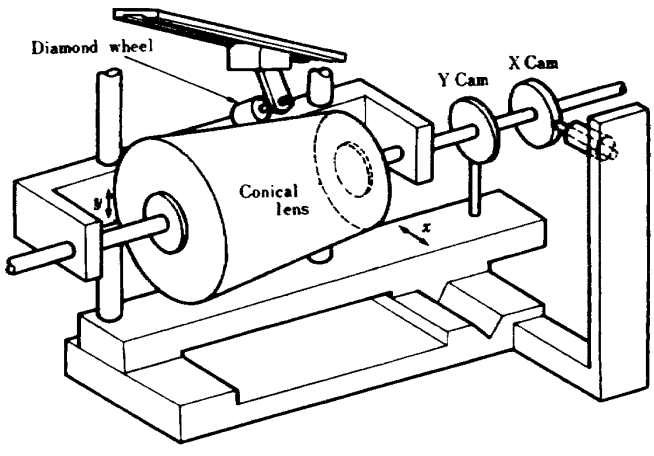

Fig. 2.4 Schematic of conical lens polishing machine.

of schlieren glass (BSC-7, best annealed, NIKON), of which refractive indexes for various wave lengths are shown in Table 2.1. Fig. 2.4 shows a schematic of the conical lens polishing machine. Three of them are called here as simple type, and have the same configuration except secondary gas injection orifice. Fig. 2.5 shows the photograph of simple type conical lens, of which minimum inner radius is 17.6 mm, maximum inner radius is 61.1 mm, cone half angle is 14°53′, and $\zeta_0=30$ mm.

The fourth one is called here as rotatable type. The rotatable type is made in two pieces, the outer lens and an inner sleeve. Fig. 2.6 and Fig. 2.7 show a schematic of rotatable conical lens attached to the wind-tunnel, and the photograph of the machined rotatable conical lens, re-

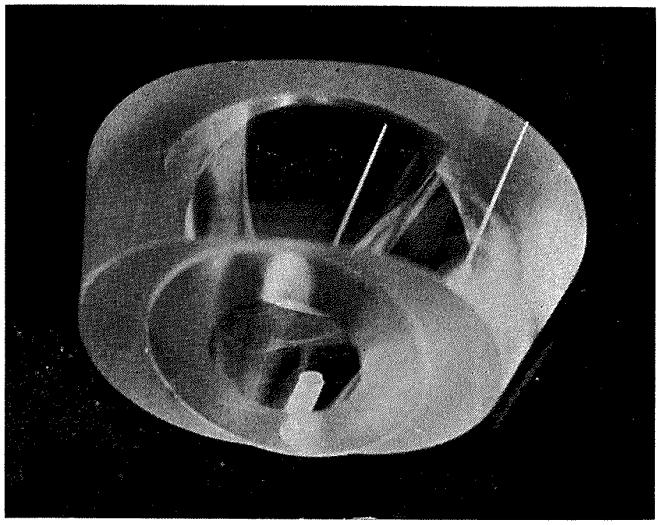

Fig. 2.5 No. 3 simple type conical lens.

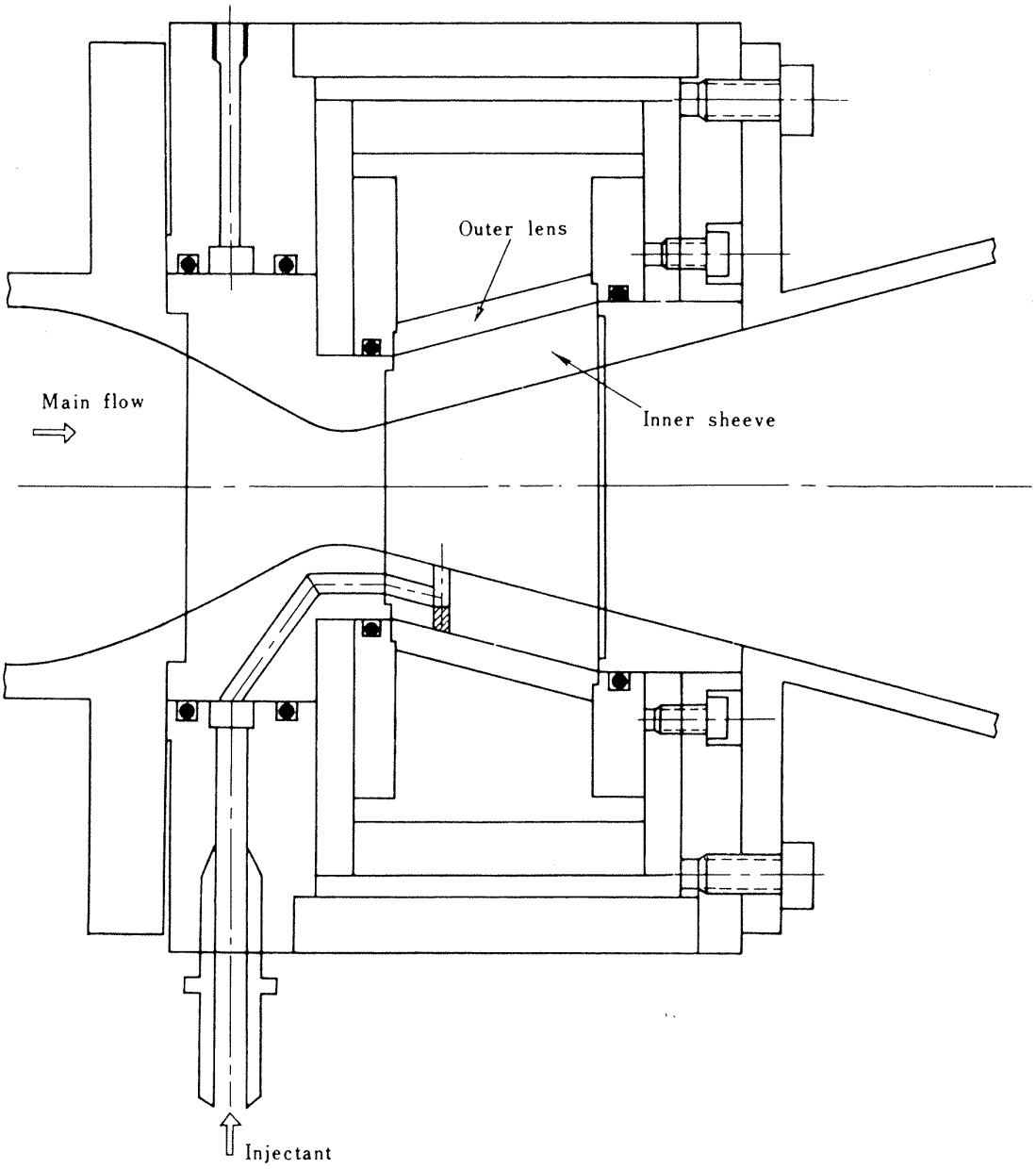

Fig. 2.6 Schematic of rotatable type conical lens nozzle.

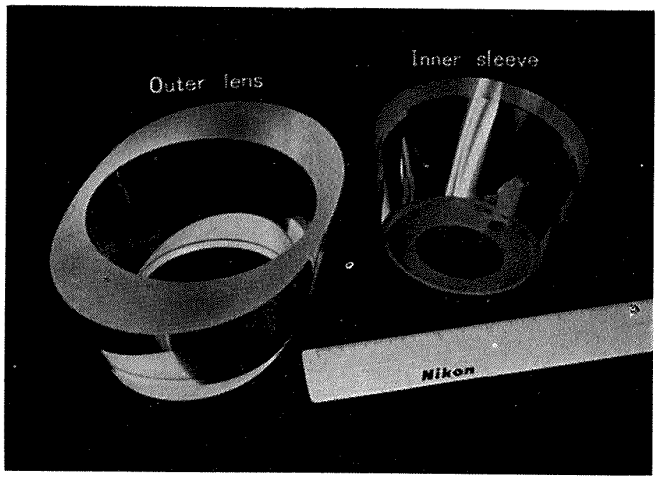

Fig. 2.7 No. 4 rotatable type conical lens.

spectively. The inner sleeve is free to rotate in order to take evolved shadowgraphs of shock waves induced by a secondary gas injection in conical supersonic flow. Upon rotating the inner sleeve, the secondary injection port rotates around the nozzle axis. In order to decrease the amount of distorsion resulting from the air-glass interfaces, a clear oil (α-chloronaphthalene ($n=1.49$) +phtalic acid dioxime ($n=1.63$), mixing ratio is 4:1 with a refractive index of 1.520 for the H_g, e line) was inserted between the outer lens and the inner sleeve. Table 2.2 shows the designed and the measured lens parameters of the polished four lenses.

Before SITVC experiment by the use of the

Table 2.2 Conical lens parameteas

Lens No.	1	2	3	4
r_0 (designed)	17.4695 mm	17.4695 mm	17.4695 mm	17.4695 mm
r_0 (measured)	17.374 mm	17.418 mm	17.606 mm	17.5175 mm
minimum radius error	−0.0955 mm	+0.0515 mm	+0.1365 mm	+0.048 mm
ζ_0 (designed)	30.000 mm	30.000 mm	30.000 mm	45.000 mm
ζ_0 (measured)	—	—	—	—
α_N (designed)	15°	15°	15°	15°
α_N (measured)	14°53′	15°1′52″	14°52′44″	14°54′06″
cone half angle error	−7′	+1′52″	−7′16″	−5′54″
dead angle zone (designed)	∓10°	∓10°	∓10°	∓10°
dead angle zone (measured)	∓20°	−10° +13°	−15° +20°	∓15°
L (measured)	50.55 mm	50.55 mm	49.77 mm	52.305 mm
R_M (measured)	122.673 mm	123.03 mm	122.204 mm	154.50 mm
d_N (measured)	5.3 mm	4.3 mm	3.1 mm	5.2 mm
H (measured)	16.0 mm	18.0 mm	18.0 mm	16.0 mm

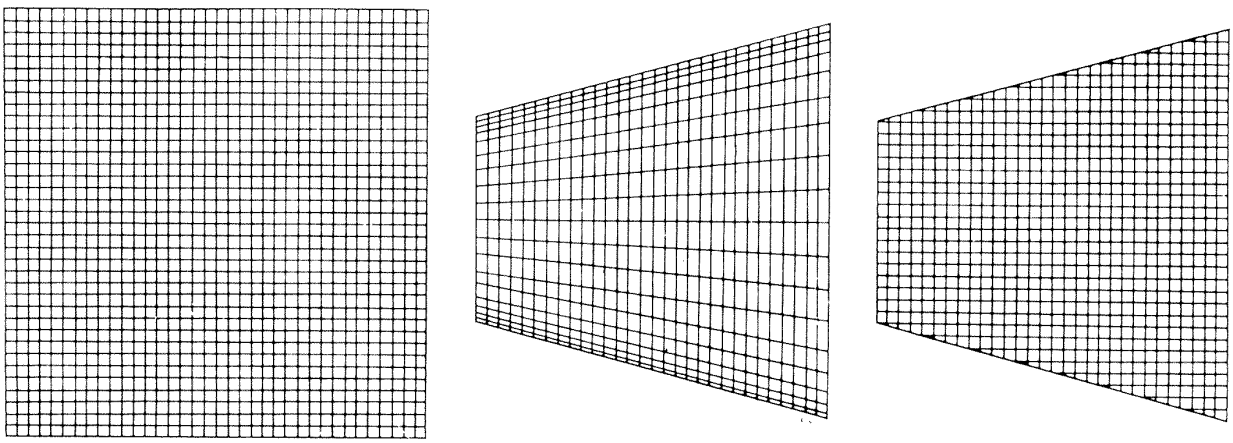

(a) Square sheet glass of 2-mm square grating

(b) Trapezium sheet glass of 10° pitch SIN. chart & 2-mm pitch lines engraved

(c) Trapezium sheet glass of 2-mm square grating

Fig. 2.8 Sheet glasses for optical calbration.

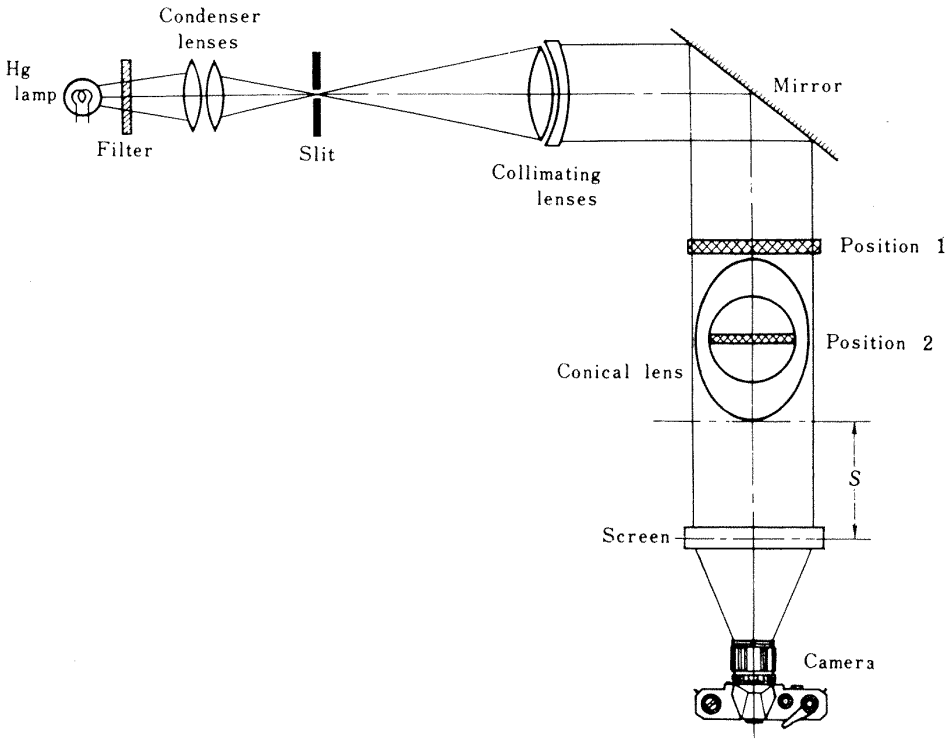

Fig. 2.9 Schematic of calibration method.

conical lenses was set about, optical calibration of the lenses had been conducted. Three kinds of sheet glasses have been used as shown in Fig. 2.8 (a), (b), and (c). Fig. 2.8 (a) shows a square sheet glass of 2 mm square grating. Fig. 2.8 (b) shows a trapezium sheet glass of 10° pitch SIN. chart and 2 mm pitch lines engraved. Fig. 2.8 (c) shows a trapezium sheet glass of 2 mm square grating. By using these sheet glasses, the calibration of optical performance of the conical lenses have been done as shown in Fig. 2.9.

The square sheet glass of 2 mm square grating (Fig. 2.8 (a)) has been used to check distorsion due to machining error. Placing it in position 1 of Fig. 2.9, the screen position has been varied from $S=0$ mm to $S=600$ mm. Fig. 2.10 shows a back-lighted (parallel light rays through filter, peak wave length=550 mμ, from a collimating system) picture showing the distorsion of the grating at $S=0$ mm.

If an incident angle (ϕ) of the incoming ray on surface of the lens approaches to 90°, then the dispersion due to machining error becomes large. The region, where dispersion predominates, is called here as dead angle zone. In order to check the dead angle zone, the trapezium sheet glass of Fig. 2.8 (b) has been used by placing it at position 2 of Fig. 2.9. Photographs have been taken by varying the distance from $S=0$ mm to $S=600$ mm. If there were no dead angle zone, $\pm 90°$ SIN. chart could be clearly taken. Fig. 2.11 shows the picture through No. 2 lens of simple type at $S=0$ mm. The dead angle zone (measured) of No. 2 lens of Table 2.2 has been measured from Fig. 2.11 of zero length distance.

The trapezium sheat glass of 2 mm square

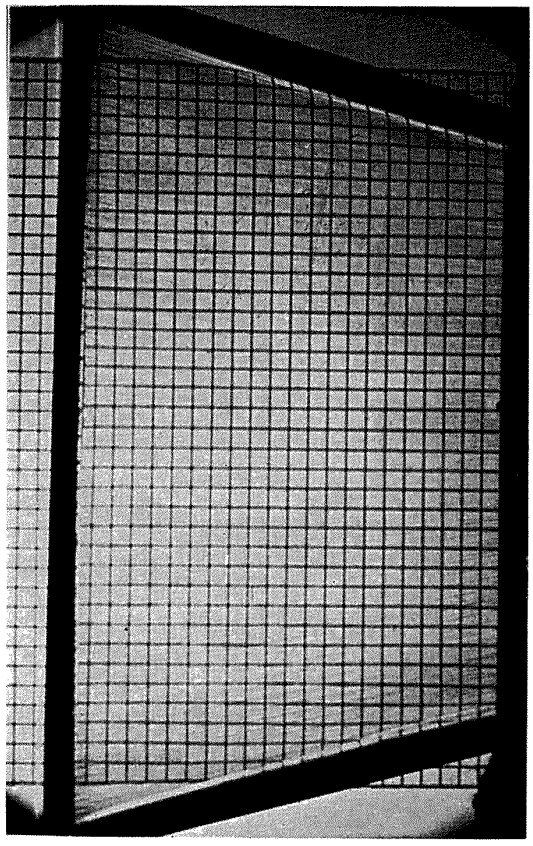

Fig. 2.10 Distorsion of the 2 mm square grating, Lens No. 2, $S=0$ mm.

Fig. 2.11 Calibration of the dead angle zone, Lens No. 2, $S=0$ mm.

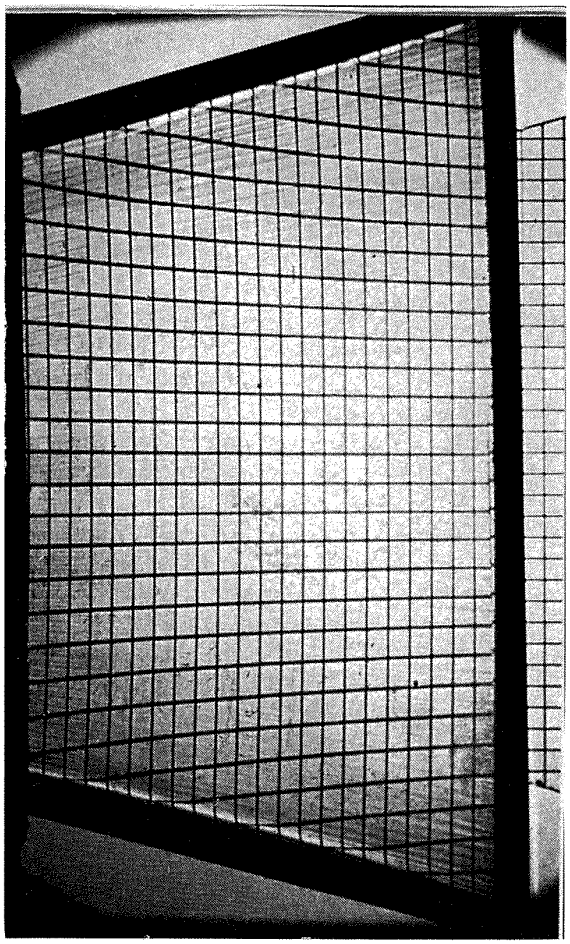

Fig. 2.12 Calibration of image co-ordinates, Lens No. 2, $S=0$ mm.

grating has been used to transform the image co-ordinates into the object co-ordinates. As it can be seen from Eqs. (2.9), (2.11), (2.16), and (2.17), the object co-ordinates in the conical pipe $(t-\psi)$ are implicit functions of the image co-ordinates $(X-Y-Z)$. Because it is only an image that one can take photographes by the use of conical lens method, transformating reference is needed. Placing the trapezium sheet glass of 2 mm square grating at position 2 of Fig. 2.9, photographs have been taken by varying the distance from $S=0$ mm to $S=600$ mm. Fig. 2.12 shows the transformating reference. As it is expected of the calibration, the longer the distance S, the bigger the distorsion.

As to the optical calibration of rotatable conical lens, on rotating inner sleeve by pitch 10°, exactly the same procedure of the above stated calibration for simple type conical lens has been conducted. Figs. 2.13, 2.14, and 2.15 show the photographs for calibration of rotatable type conical lens.

2.3. Three-Dimensional Investigation of Leading Shock Waves Induced by Secondary Gas Injection by the Use of Conical Lenses

Leading shock waves induced by secondary air injection have been optically observed by the conical lenses calibrated in the previous part of this section. The test apparatus used was the same as in the two-dimensional experiment except that the nozzle part was replaced by lens nozzle as shown in Figs. 2.16 and 2.17. In order to avoid dispersion due to wave lengths, the transmission type interference filter has been used, which transmits the 548.5 ± 0.8 mμ wave. More than hundred test runs of three simple type and one rotatable type conical lenses have been carried out.

An analysis is tried to predict the leading shock waves observed by the conical flow experiment. Using Eqs. (1.1)-(1.11) with the previously mentioned assumption, and further assuming that the jet is enveloped by the stream tubes, the free jet boundary and the penetrating length has been easily predicted by the analysis of the first section of the present study. As-

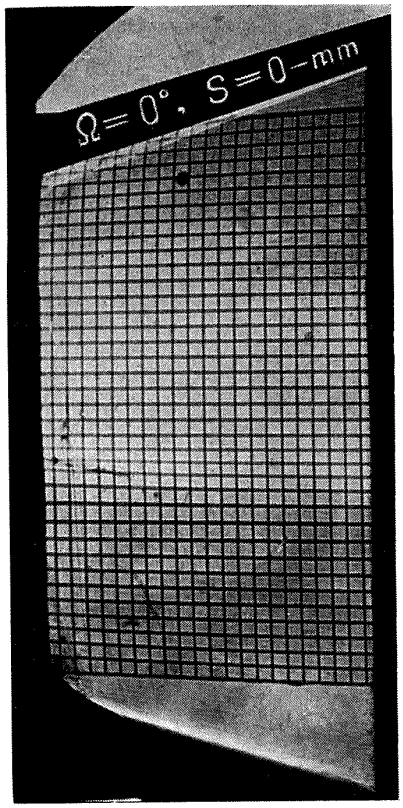

①

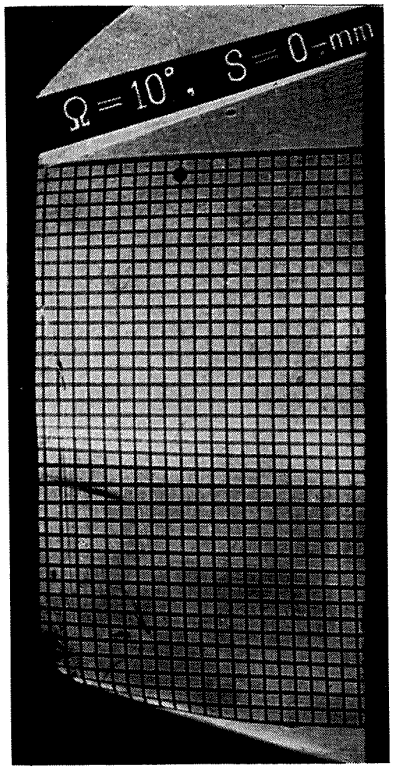

②

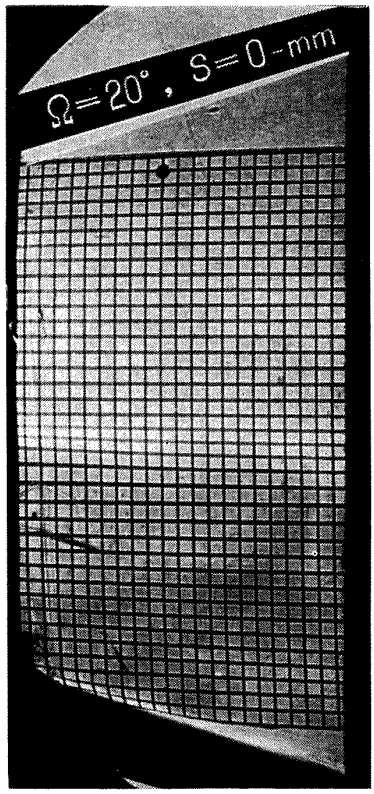

③

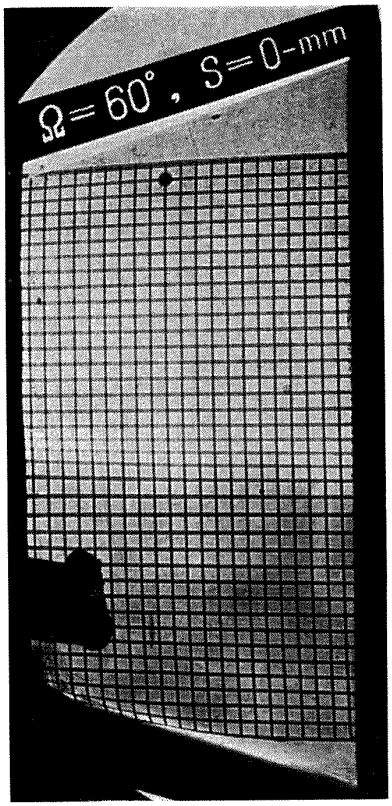

⑦

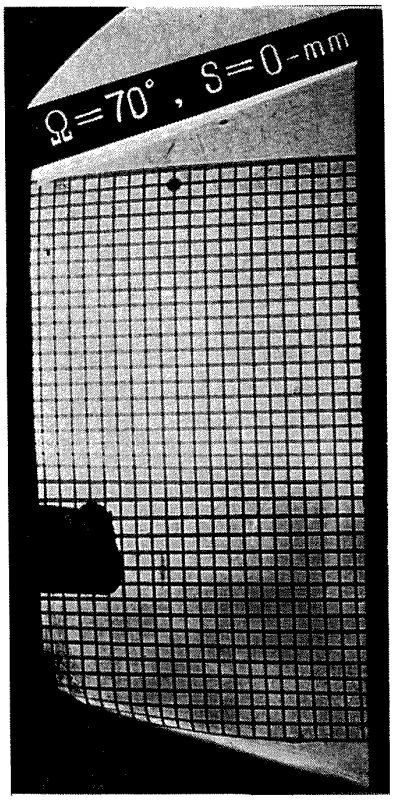

⑧

Fig. 2.13 Distorsion of the 2 mm square grating

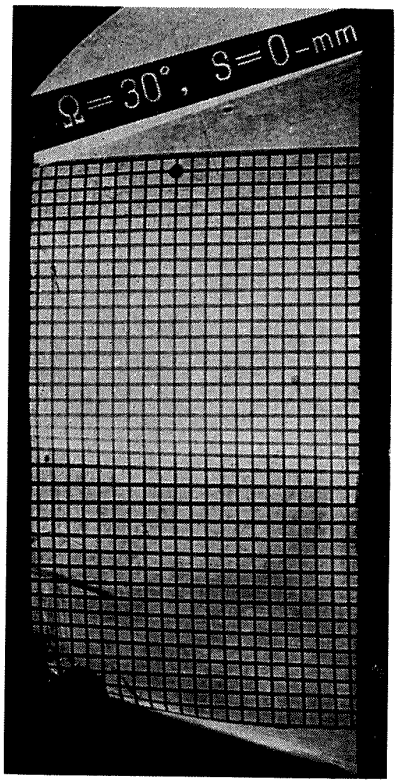

④

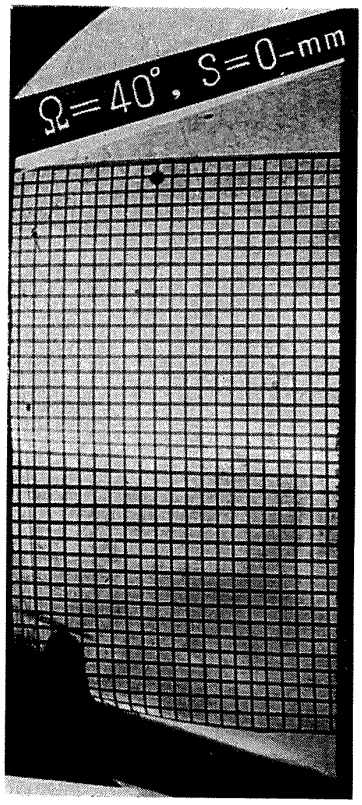

⑤

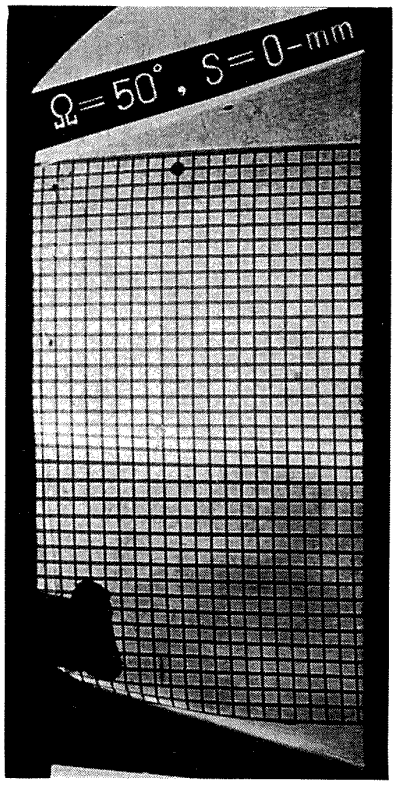

⑥

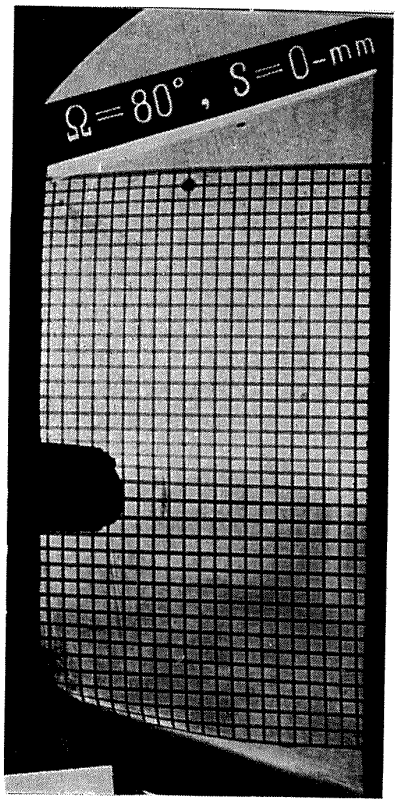

⑨

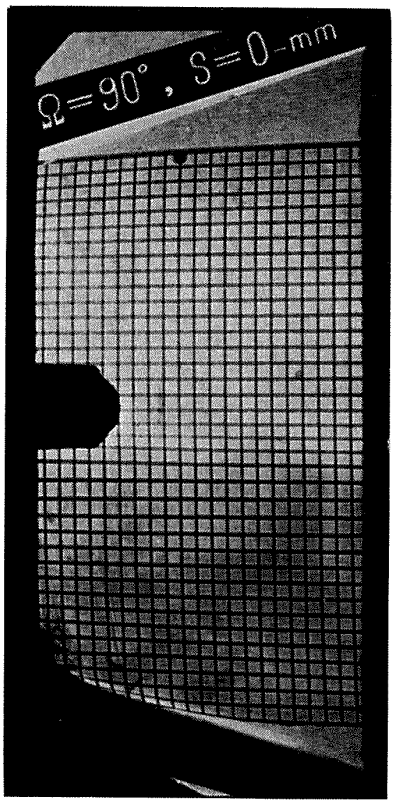

⑩

of No. 4 rotatable type conical lens, $S=0$ mm.

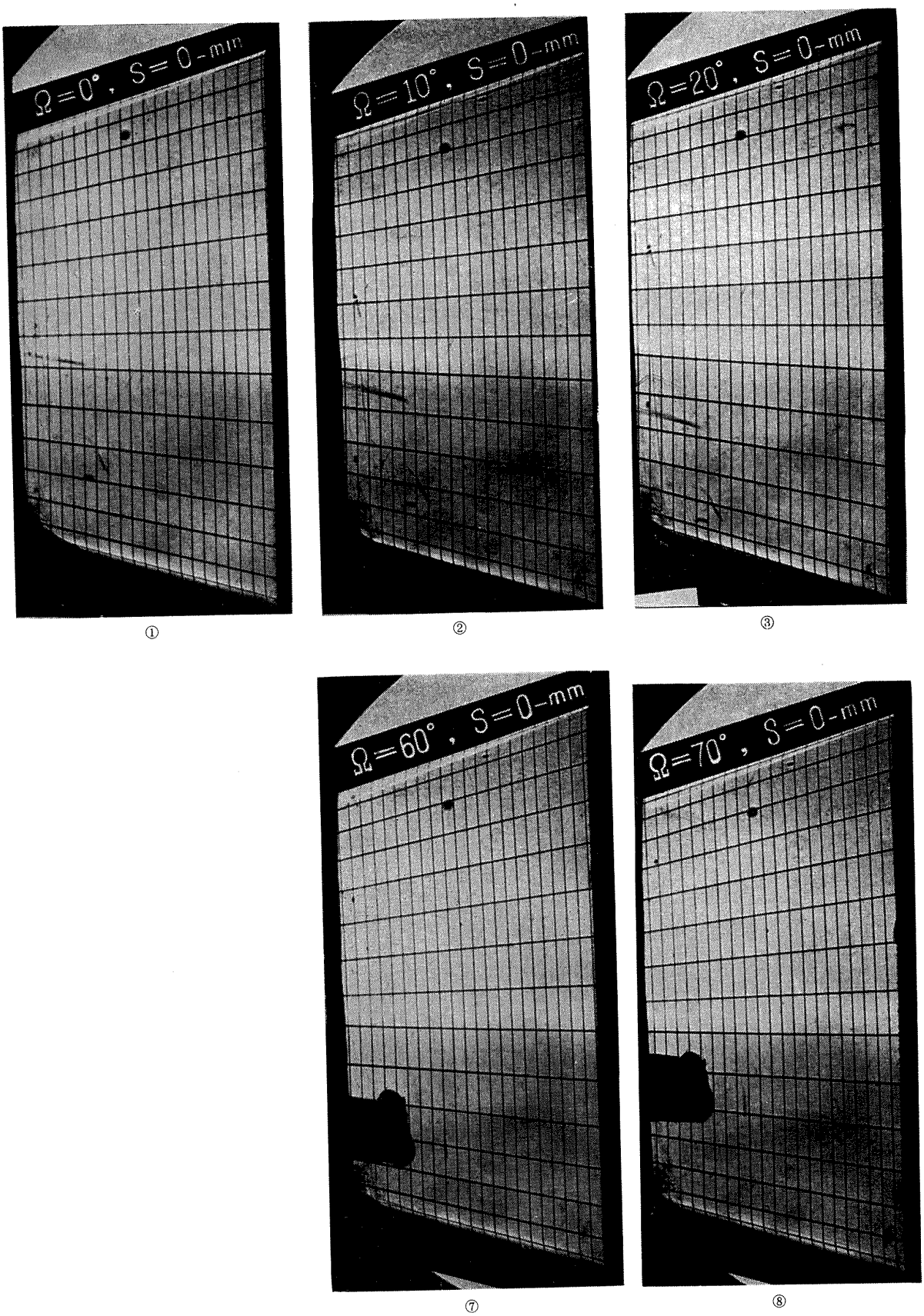

Fig. 2.14 Calibration of the dead angle zone

④

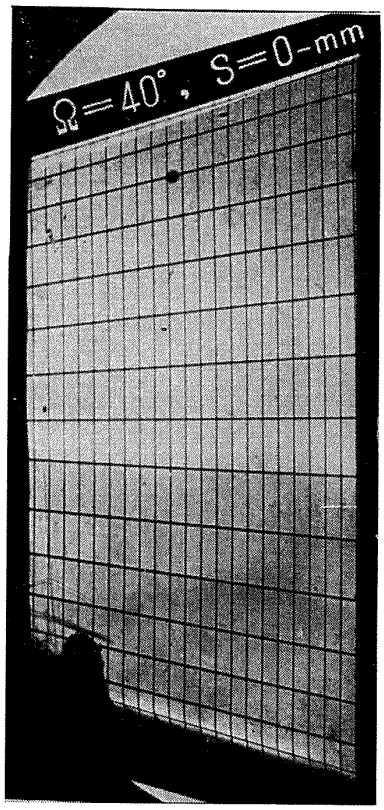

⑤

⑥

⑨

⑩

of No. 4 rotatable type conical lens, $S=0$ mm.

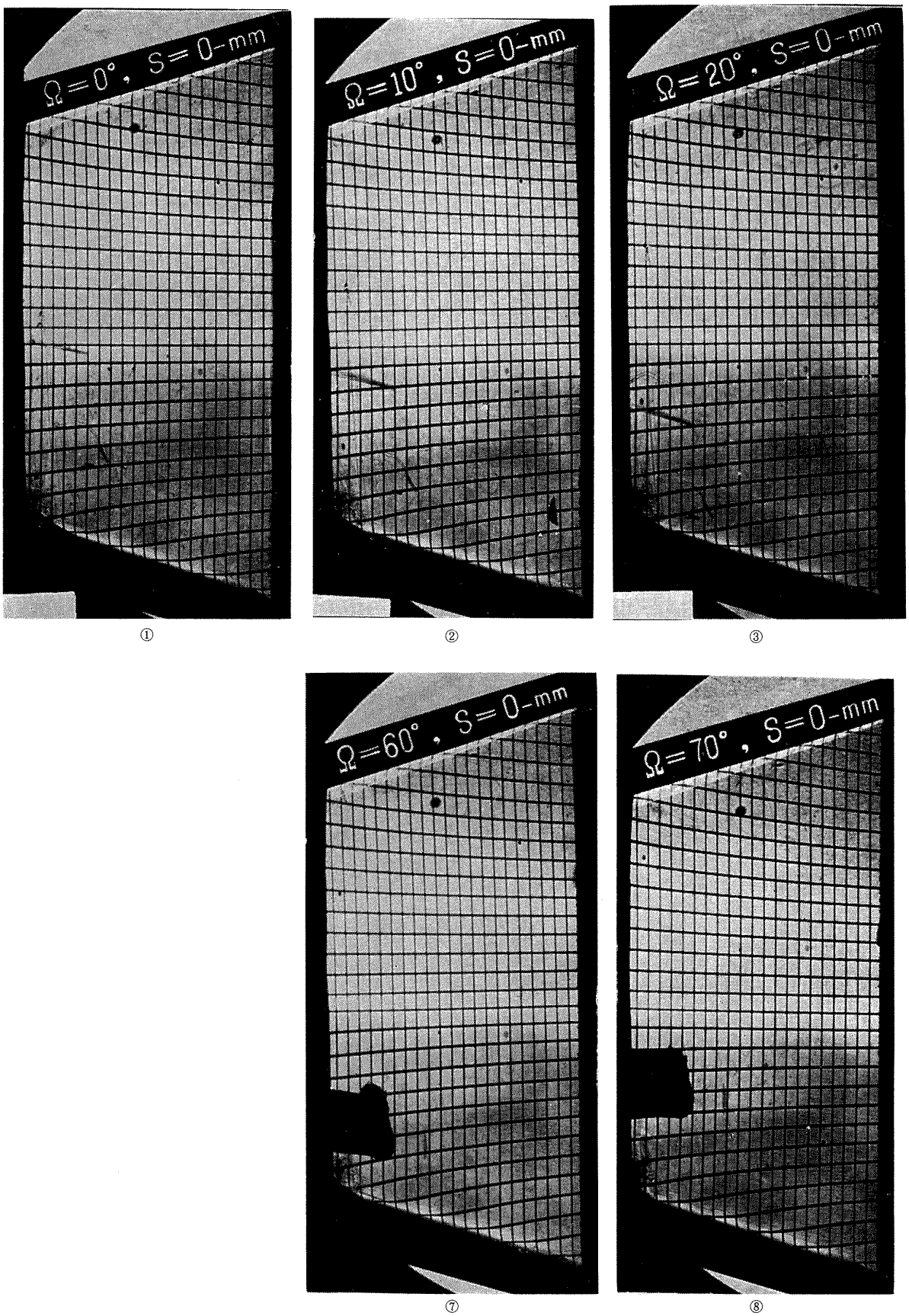

Fig. 2.15 Calibration of image co-ordinates (2 mm square

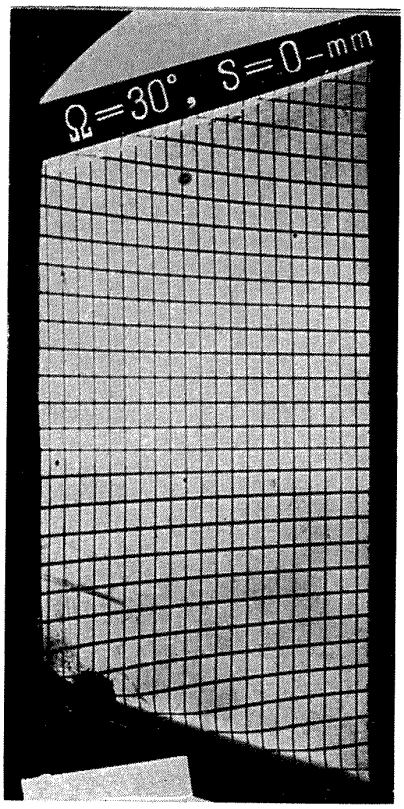

④

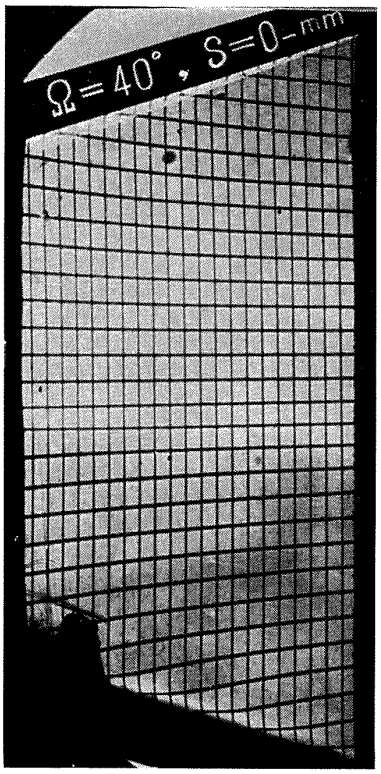

⑤

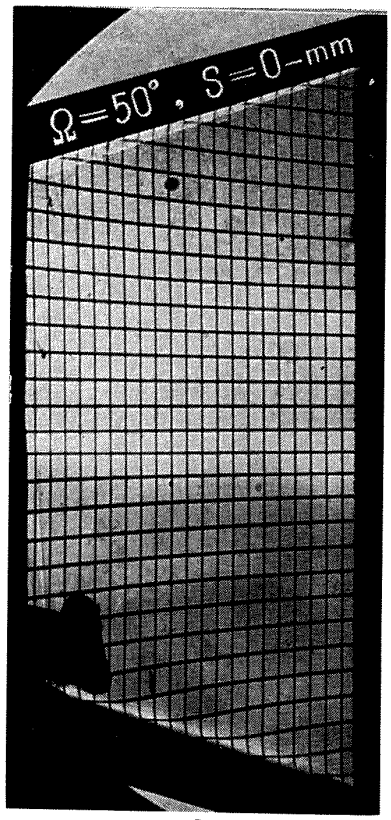

⑥

⑨

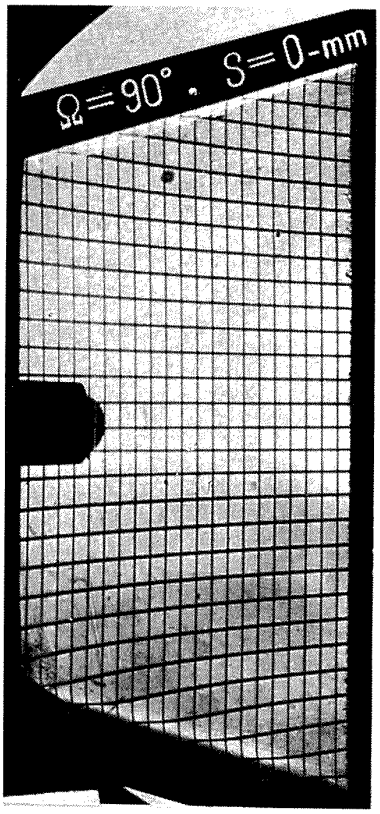

⑩

grating) of No. 4 rotatable type conical lens, $S=0$ mm.

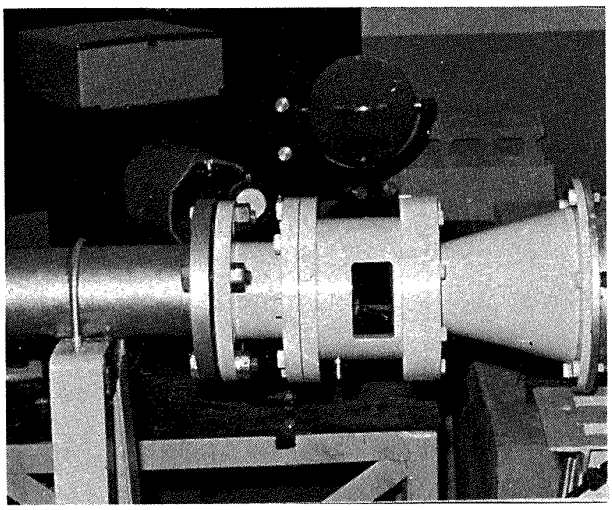

Fig. 2.16 Simple type conical lens nozzle.

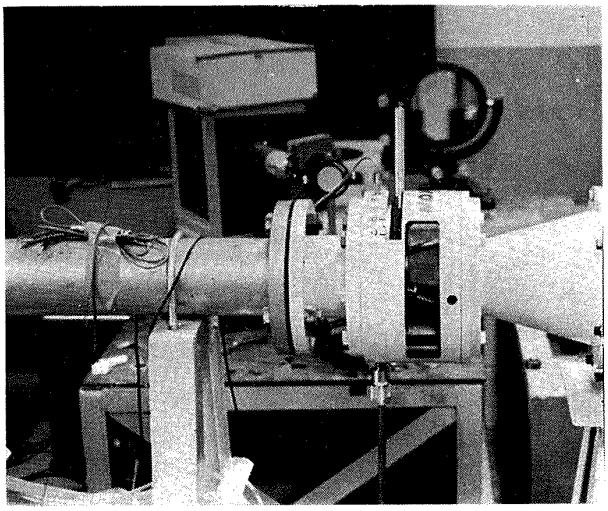

Fig. 2.17 Rotatable type conical lens nozzle.

suming that the under-expanding jet expands along the jet stream and further the jet over-expands until the Riemann wave stands and is recompressed to the aft-leading shock mixing region pressure, the jet can be considered as a valid obstruction to the supersonic main flow. The generation of the leading shock wave will be induced by this obstruction. According to the analytical model presented in the first section of the present study, some analytical treatment has been tried to predict the leading shock shape.

In order to predict the leading shock waves, the blast wave analogy has been used. Lees and Kubota[19] investigated bow shock waves generated by a hemi-spherer-cylinder at $M_\infty=7.7$, and indicated that the leading shock shape was predicted very accurately by the blast wave similarity analysis. The author extended this analysis to the leading shock waves induced by protruding a projection into medium Mach Numbers supersonic conical flow[20]. The following equation was used in the reference;

$$\frac{R}{d_b}=\left(\frac{2\gamma}{\pi J}\right)^{1/4}\left\{1-\lambda\left(\frac{\pi J}{2\gamma}\right)^{1/2}\frac{1}{M_\infty{}^2}\frac{\xi}{d_b}\right\}^{1/2}\left(\frac{\xi}{d_b}\right)^{1/2} \tag{2.18}$$

where R is cylindrical blast wave radius, d_b is the diameter of the blunt nose, and ξ is axial distance of cylindrical blast wave analogy. The d_b was calculated as a diameter of the sphere, which had the same frontal areas as that of the jet extending from the nozzle exit to the first Mach disc.

Broadwell[2], Karamcheti and Hsia[3], and Hsia, Seifert and Karamcheti[15] calculated the shape of the induced shock by secondary injection, also by using the results of the analogy between the unsteady flowfield of a cylindrical blast wave and steady, axisymmetric inviscid, small disturbance, hypersonic flowfield past a blunt-nosed slender body of revolution. In applying the blast wave analogy to SITVC problem, however they accounted the energy term as equal to the magnitude of the axial momentum of the secondary injection per unit time. Hsia, Seifert, and Karamcheti used the following equation for their theory;

$$\frac{R}{R_*}=\left(\frac{4\gamma}{\pi J}\right)^{1/4}\left\{1-\lambda\left(\frac{\pi J}{4\gamma}\right)^{1/2}\frac{1}{M_\infty{}^2}\frac{\xi}{R_*}\right\}^{1/2}\left(\frac{\xi}{R_*}\right)^{1/2} \tag{2.19}$$

where $R_*=(\dot{m}_j/\dot{m}_0\cdot u_e/u_\infty\cdot A_\infty)^{1/2}$, u_e is the axial component of the velocity at the rocket nozzle exit in the absence of injection, $\dot{m}_0$ is the main stream mass flow rate, and A_∞ is the area of main nozzle at injection. In order to calculate leading shock shapes by Eqs. (2.18) and (2.19), ξ is started from the intersecting point of the main detached shock and the axis parallel to the wall through the separation flow symmetrical point. Fig. 1.6 shows the relations of injection flow, two inscribed ellipsoids, main detached shock, separation detached shock, separation shock angle, and the starting point of leading shock. $J=0.88$ and $\lambda=-1.989$ for $\gamma=1.4$ have been used in the calculation[21],[22].

Table 2.3 shows the typical test runs of experiment carried out by using the three simple type conical lenses. The blunt body parameters of injection jet and disturbances ahead of the injection port have been calculated by the analysis of the previous section. The shadowgraphs taken by simple type conical lenses are shown in Fig. 2.18, which have been directly projected through conical lens to the film (Kodak, TRI-X Pan, 2.25×3.25 in.) with exposure time 1/90 seconds. Only at Run No. 3, the lens has been

Table 2.3 Test results under-expanding air injection into simple type conical lens nozzle

Run No.	1	2	3	4	5	6	7	8	9
Lens No.	1	1	1	2	2	2	3	3	3
$P_{c0}=P_{j0}$ (kg/cm²ab)	18.8	18.0	13.5	15.7	16.2	16.0	16.5	16.7	12.7
M_∞	2.25	2.25	2.25	2.31	2.31	2.31	2.31	2.31	2.31
M_N	1	1	1	1	1	1	1	1	1
M_e	1.88	1.88	1.88	1.93	1.93	1.93	1.93	1.93	1.93
d_N (mm)	5.3	5.3	5.3	4.3	4.3	4.3	3.1	3.1	3.1
d_* (mm)	5.3	5.3	5.3	4.3	4.3	4.3	3.1	3.1	3.1
δ_N (degrees)	0	0	0	0	0	0	0	0	0
δ_I (degrees)	15.0	15.0	15.0	15.0	15.0	15.0	15.0	15.0	15.0
$\dot{m}_j$ (Nm³/s)$\times 10^{-3}$	43.0	41.7	34.0	35.8	37.0	36.4	—	—	—
$d_{N\,\mathrm{eff}}$	3.97	3.98	4.15	3.95	3.95	3.94	2.87*	2.87*	2.87*
δ_s (degrees)	20.1	20.1	20.1	20.1	20.1	20.1	20.1	20.1	20.1
σ (degrees)	47.0	47.0	47.0	46.0	46.0	46.0	46.0	46.0	46.0
M_s	1.45	1.45	1.45	1.49	1.49	1.49	1.49	1.49	1.49
M_p	3.10	3.10	3.10	3.19	3.19	3.19	3.19	3.19	3.19
Ellipsoid (Main)									
$a_M/d_{N\,\mathrm{eff}}$	0.793	0.793	0.793	0.812	0.812	0.812	0.812	0.812	0.812
$b_M/d_{N\,\mathrm{eff}}$	1.14	1.14	1.14	1.18	1.18	1.18	1.18	1.18	1.18
$x_{0M}/d_{N\,\mathrm{eff}}$	0.487	0.487	0.487	0.524	0.524	0.524	0.524	0.524	0.524
$y_{0M}/d_{N\,\mathrm{eff}}$	0.665	0.665	0.665	0.685	0.685	0.685	0.685	0.685	0.685
Ellipsoid (Separated)									
$x_{0s}/d_{N\,\mathrm{eff}}$	0.200	0.200	0.200	0.229	0.229	0.229	0.229	0.229	0.229
$y_{0s}/d_{N\,\mathrm{eff}}$	0.614	0.614	0.614	0.633	0.633	0.633	0.633	0.633	0.633
$\Delta_{0M}/d_{N\,\mathrm{eff}}$	0.41	0.41	0.41	0.399	0.399	0.399	0.399	0.399	0.399
$R_{sM}/d_{N\,\mathrm{eff}}$	2.52	2.52	2.52	2.56	2.56	2.56	2.56	2.56	2.56
Penetrating length/$d_{N\,\mathrm{eff}}$	0.706	0.706	0.706	0.763	0.763	0.763	0.763	0.763	0.763
$A_D/d^2_{N\,\mathrm{eff}}$	2.01	2.01	2.01	2.22	2.22	2.22	2.22	2.22	2.22

* Flow rates missed, discharge coefficients of Table 1.1 (3ϕ) is applied.

rotated around the lens axis by 180° to check the dispersion characteristics of the incoming ray direction.

The calculated leading shock waves also are compared in the photographs. According to the discussion of the first section, the axis of cylindrical blast wave analogy is taken parallel to the nozzle wall. Because Fig. 2.18 shows the image co-ordinates of the shock waves induced in the lens, the calculated leading shock shapes of Eqs. (2.18), and (2.19) are transformed into the image co-ordinates by using the lens equations (2.1)-(2.17).

By using calibration grating of Fig. 2.8 (c), placing the film holder in the same position where the photographs of Fig. 2.18 were taken, the comparison of the shadowgraphs of leading shocks with the analysis is shown in Fig. 2.19 in the object co-ordinates also. Figs. 2.18 and 2.19 show that the calculated leading shock waves from Eq. 2.18, based on the under-expanding gas injection model of the first section of the present study, extremelly well agree with the experimental results of three-dimensional conical nozzle flow. This experimental conclusion may answer to the question presented by Hsia, Seifert, and Karamcheti[15], as to whether or not it is valid to assume that the blast wave axis is parallel to the nozzle axis for all conditions of injection.

A series of evolved shadowgraphs of induced shocks has been taken by the use of No. 4 rotatable type conical lens. Table 2.4 shows the typical test runs of the experiment; injection conditions, injected free jet parameters, separation conditions, and the injection angles to the transverse plane of the incoming parallel light rays, Ω. The injection angle, Ω, is varied from 0° to 90°. The evolved shadowgraphs are shown in

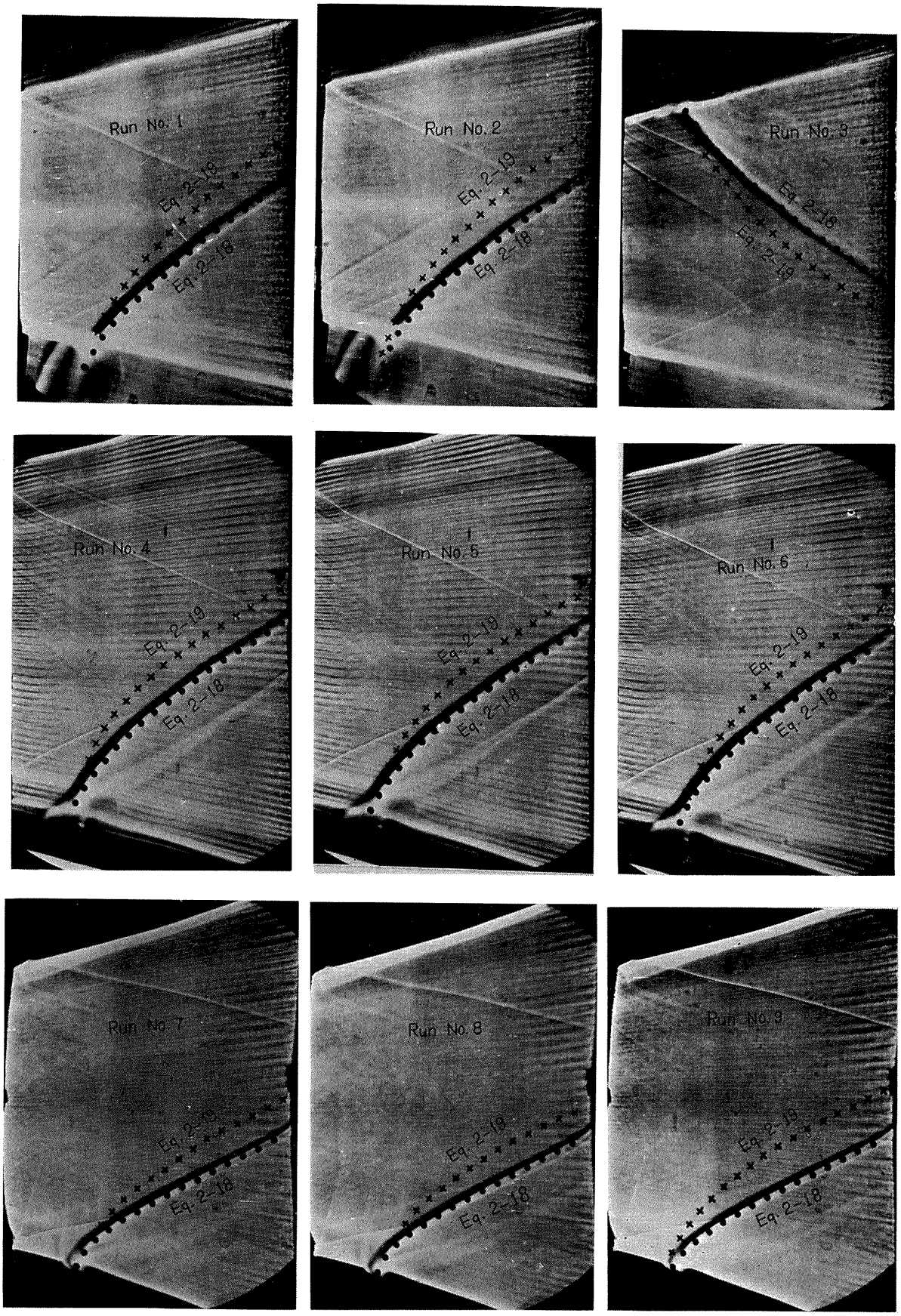

Fig. 2.18 Leading shock waves induced by secondary air injection into simple type conical lenses and comparison with Eqs. (2.18), and (2.19).

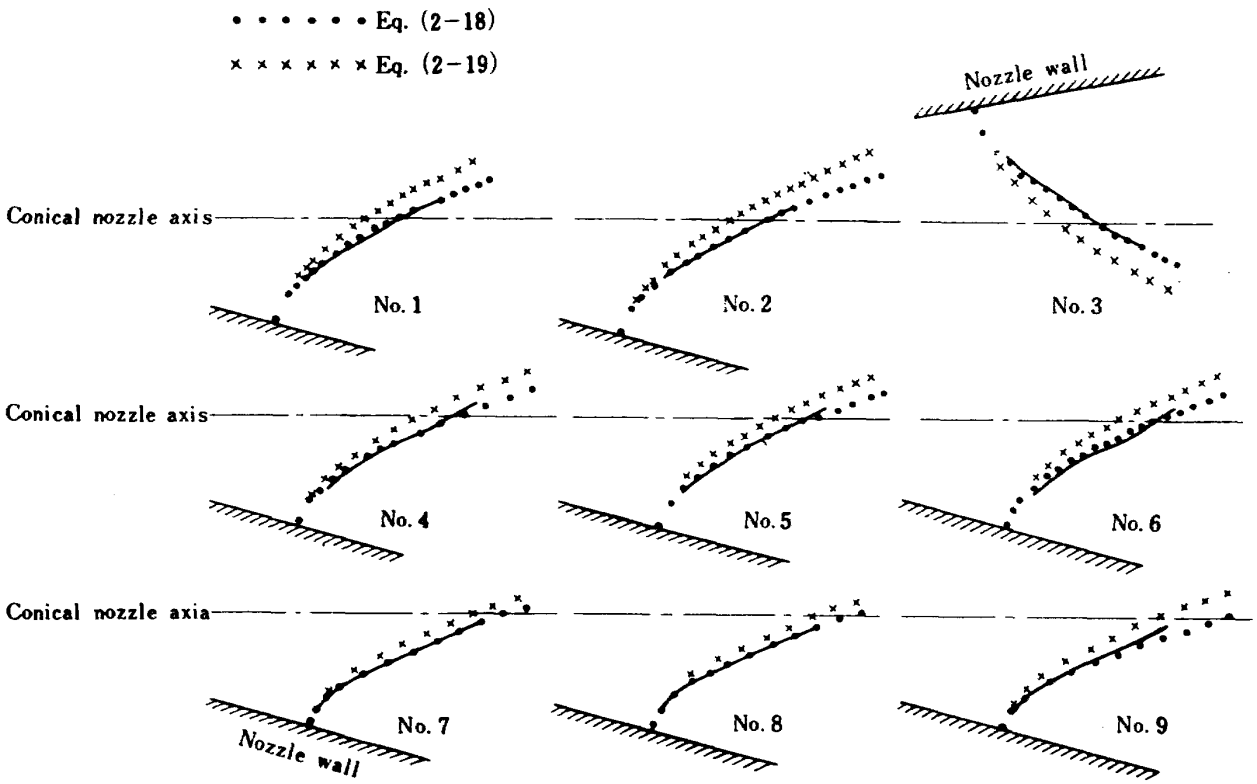

Fig. 2.19 Leading shocks in the object co-ordinates (Simple type conical lenses).

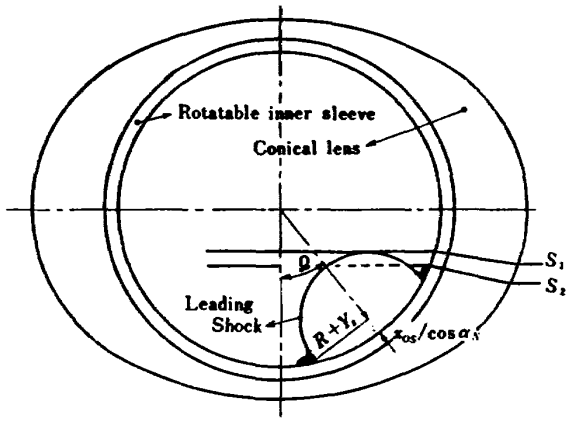

Fig. 2.20 Shock front (S_1) surface and separation front (S_2) of rotatable conical lens experiment.

Fig. 2.21.

The theoretically calculated leading shock front (S_1, by Eq. 2.18) and separation front (S_2, see Fig. 2.20) also are compared in the photographs. By using the calibration grating of Fig. 2.8 (c), placing the film holder in the same position where the photographs of Fig. 2.21 were taken, the comparison of the shadowgraphs of the leading shocks with the theoretically calculated leading shock front (S_1) and the separation fronts (S_2) are shown in Fig. 2.22 in the object co-ordinates also.

The figures show that; if Ω increases, the shock front becomes larger than that calculated by axisymmetric blast wave theory. As it can easily understood, as far as $P_{c0}=P_{j0}$, the fluctuations of the induced shock shapes depend only on the injected mass flow rate, $\dot{m}_j$, as an order of those of $d_{N\text{eff}}$. Table 2.4 shows that the fluctuation of $d_{N\text{eff}}$ is within 0.75%. Therefore, it can be concluded that the series of tests of Fig. 2.22 have the identity with accuracy of 0.75%. Under the justification of this identity, the series of tests in the object co-ordinates of Fig. 2.22 can be plotted down in cross sectional views. Fig. 2.23 shows cross sectional views of the leading shock in the object co-ordidates, where ε is expansion ratio of the section. These cross sectional views show that the axisymmetricity of the leading shock wave induced by the secondary injection loses and the cross section looks like that of an oblate spheroid.

The parameters of the oblateness of the induced shocks are shown in Fig. 2.24. An ellipse is assumed to envelope the experimental surfaces at each cross section. The maximum and the minimum semimajor axes which envelope the maximum and the minimum experimental surfaces, respectively, are plotted to the axial blast wave axis. The semiminor axes are taken as the experimental radii at $\Omega=0°$. Fig. 2.24 shows that the shock surface has an approximately elliptical cross section with axes ratio of 1.5. This experimental result also answer to the question presented by Hsia, Seifert, and Karamcheti[15],

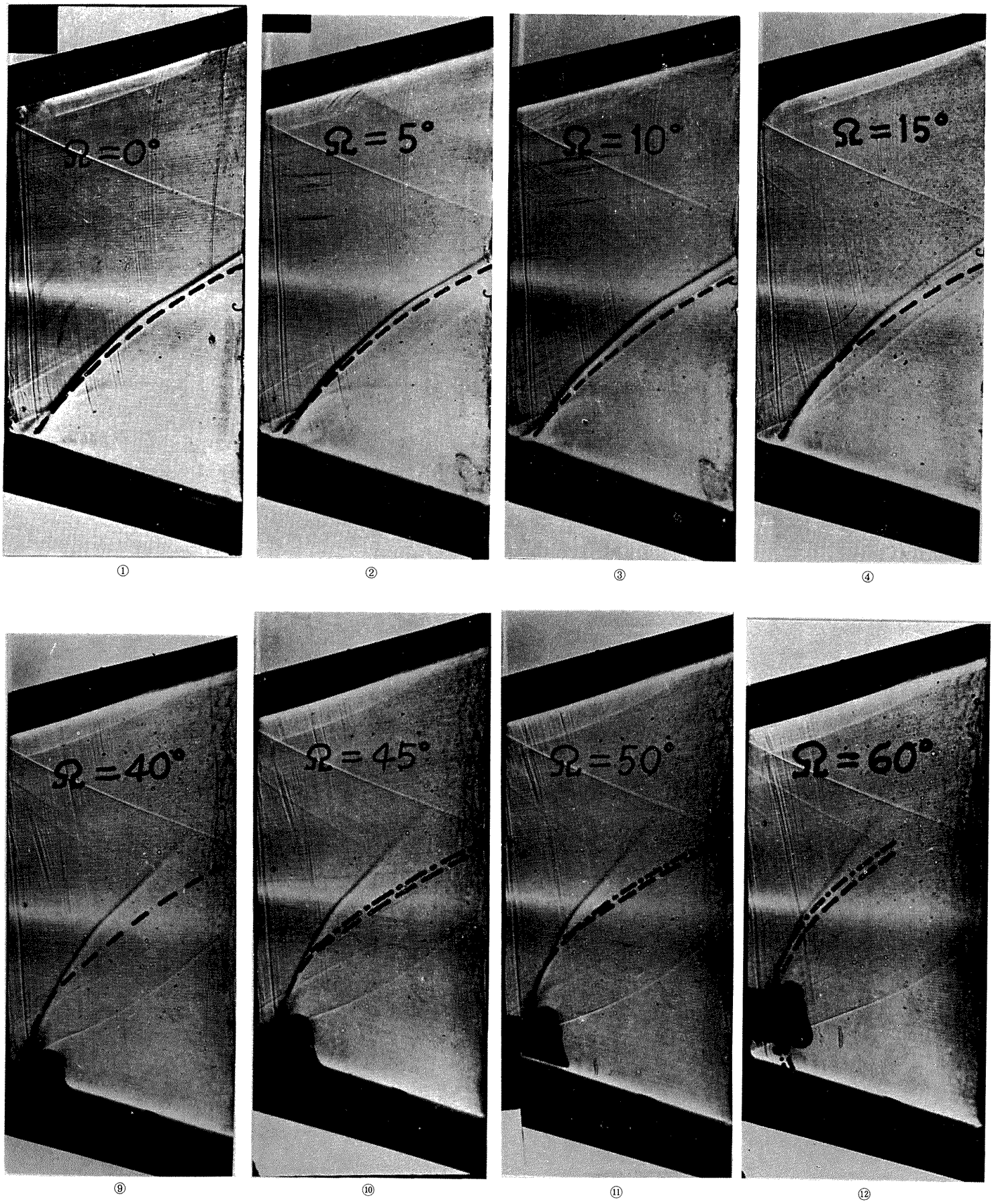

Fig. 2.21 A series of evolved shadowgraphs of the shock waves induced by the secondary

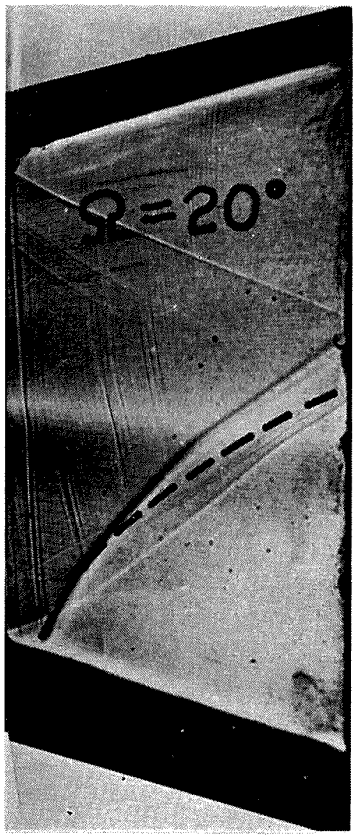

⑤

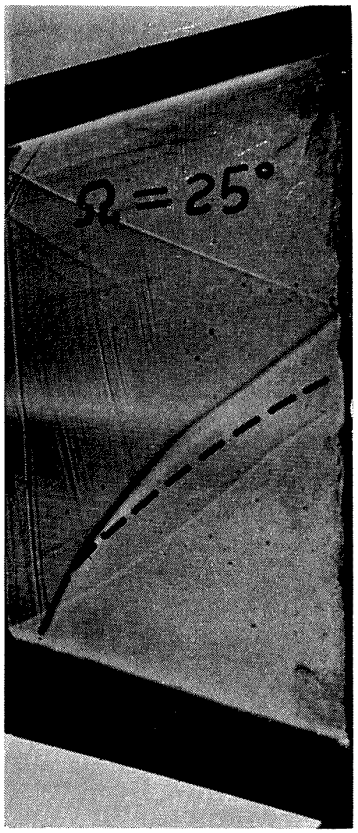

⑥

⑦

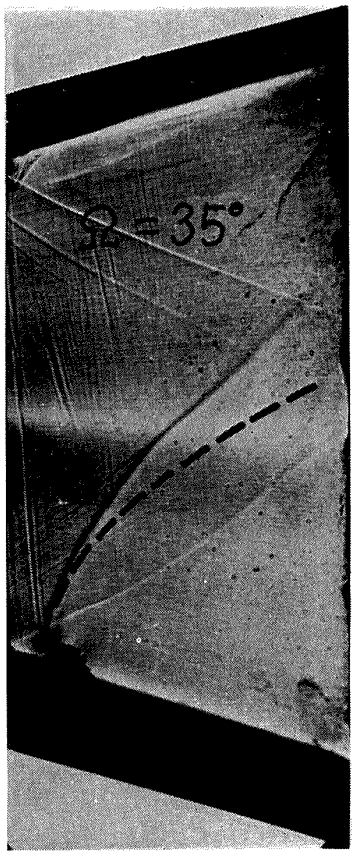

⑧

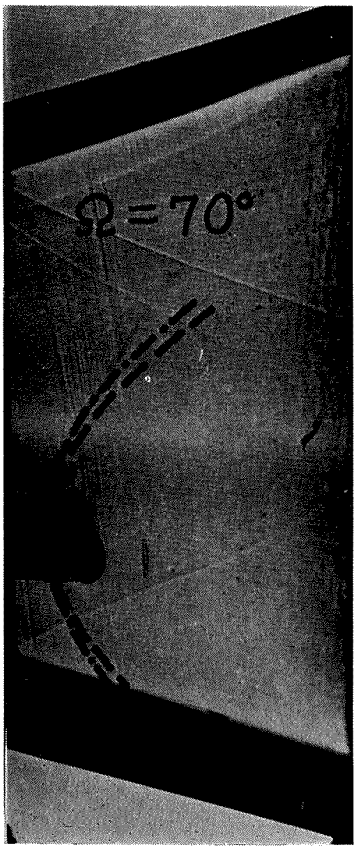

⑬

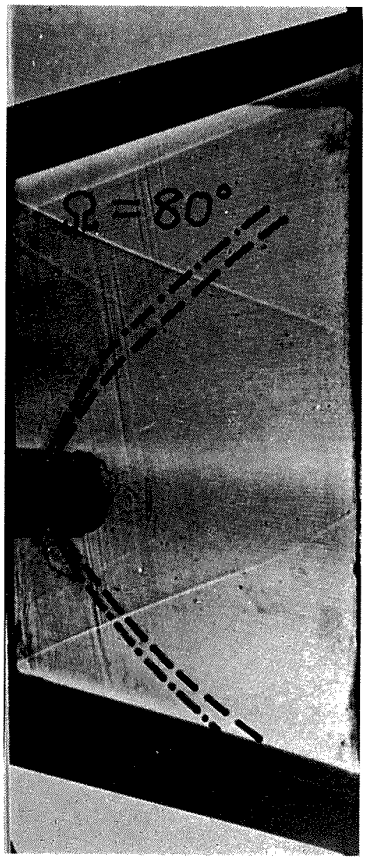

⑭

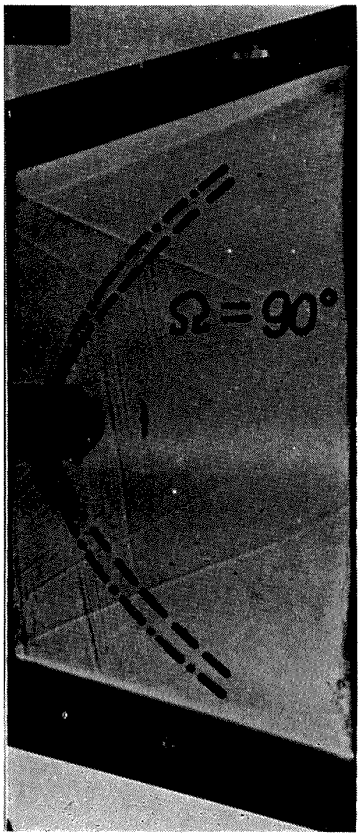

⑮

gas injection in the image co-ordinates (broken curves show S_1 and one dotted ones show S_2).

Table 2.4 Test results of under-expanding air injection into rotatable type conical lens nozzle

Ω (degrees)	0	5	10	15	20	25	30	35	40	45	50	60	70	80	90
$P_{c0}=P_{J0}$ (kg/cm²ab)	11.30	11.28	11.23	11.06	11.19	11.76	11.37	11.23	11.28	11.08	11.08	11.48	11.28	10.10	10.05
M_∞	2.26	2.26	2.26	2.26	2.26	2.26	2.26	2.26	2.26	2.26	2.26	2.26	2.26	2.26	2.26
M_N	1.00	1.00	1.00	1.00	1.00	1.00	1.00	1.00	1.00	1.00	1.00	1.00	1.00	1.00	1.00
Me	1.88	1.88	1.88	1.88	1.88	1.88	1.88	1.88	1.88	1.88	1.88	1.88	1.88	1.88	1.88
d_N (mm)	5.2	5.2	5.2	5.2	5.2	5.2	5.2	5.2	5.2	5.2	5.2	5.2	5.2	5.2	5.2
d_* (mm)	5.2	5.2	5.2	5.2	5.2	5.2	5.2	5.2	5.2	5.2	5.2	5.2	5.2	5.2	5.2
δ_N (degrees)	0.0	0.0	0.0	0.0	0.0	0.0	0.0	0.0	0.0	0.0	0.0	0.0	0.0	0.0	0.0
δ_I (degrees)	15	15	15	15	15	15	15	15	15	15	15	15	15	15	15
$\dot{m}_J$ (N m³/s)$\times 10^{-2}$	2.76	2.61	2.64	2.65	2.64	2.80	2.67	2.65	2.75	2.73	2.75	2.82	2.78	2.44	2.43
$d_{N\,\mathrm{eff}}$ (mm)	4.08	3.98	4.01	4.04	4.01	4.03	4.01	4.02	4.07	4.09	4.11	4.09	4.05	4.05	4.06
δ_s (degrees)	20.1	20.1	20.1	20.1	20.1	20.1	20.1	20.1	20.1	20.1	20.1	20.1	20.1	20.1	20.1
σ (degrees)	46.9	46.9	46.9	46.9	46.9	46.9	46.9	46.9	46.9	46.9	46.9	46.9	46.9	46.9	46.9
M_s	1.45	1.45	1.45	1.45	1.45	1.45	1.45	1.45	1.45	1.45	1.45	1.45	1.45	1.45	1.45
M_p	3.11	3.11	3.11	3.11	3.11	3.11	3.11	3.11	3.11	3.11	3.11	3.11	3.11	3.11	3.11
Ellipsoid (Main)															
$a_M/d_{N\,\mathrm{eff}}$	0.793	0.793	0.793	0.793	0.793	0.793	0.793	0.793	0.793	0.793	0.793	0.793	0.793	0.793	0.793
$b_M/d_{N\,\mathrm{eff}}$	1.14	1.14	1.14	1.14	1.14	1.14	1.14	1.14	1.14	1.14	1.14	1.14	1.14	1.14	1.14
$x_M/d_{N\,\mathrm{eff}}$	0.489	0.489	0.489	0.489	0.489	0.489	0.489	0.489	0.489	0.489	0.489	0.489	0.489	0.489	0.489
$y_M/d_{N\,\mathrm{eff}}$	0.689	0.689	0.689	0.689	0.689	0.689	0.689	0.689	0.689	0.689	0.689	0.689	0.689	0.689	0.689
Ellipsoid (Separated)															
$a_s/d_{N\,\mathrm{eff}}$	0.578	0.578	0.578	0.578	0.578	0.578	0.578	0.578	0.578	0.578	0.578	0.578	0.578	0.578	0.578
$b_s/d_{N\,\mathrm{eff}}$	0.869	0.869	0.869	0.869	0.869	0.869	0.869	0.869	0.869	0.869	0.869	0.869	0.869	0.869	0.869
$x_{0s}/d_{N\,\mathrm{eff}}$	0.201	0.201	0.201	0.201	0.201	0.201	0.201	0.201	0.201	0.201	0.201	0.201	0.201	0.201	0.201
$y_{0s}/d_{N\,\mathrm{eff}}$	0.629	0.629	0.629	0.629	0.629	0.629	0.629	0.629	0.629	0.629	0.629	0.629	0.629	0.629	0.629
$\Delta_{0M}/d_{N\,\mathrm{eff}}$	0.410	0.410	0.410	0.410	0.410	0.410	0.410	0.410	0.410	0.410	0.410	0.410	0.410	0.410	0.410
$R_{sM}/d_{N\,\mathrm{eff}}$	2.49	2.49	2.49	2.49	2.49	2.49	2.49	2.49	2.49	2.49	2.49	2.49	2.49	2.49	2.49
$\Delta_{0s}/d_{N\,\mathrm{eff}}$	0.605	0.605	0.605	0.605	0.605	0.605	0.605	0.605	0.605	0.605	0.605	0.605	0.605	0.65	0.605
$R_{ss}/d_{N\,\mathrm{eff}}$	2.64	2.64	2.64	2.64	2.64	2.64	2.64	2.64	2.64	2.64	2.64	2.64	2.64	2.64	2.64
Penetrating length/$d_{N\,\mathrm{eff}}$	0.714	0.714	0.714	0.714	0.714	0.714	0.714	0.714	0.714	0.714	0.714	0.714	0.714	0.714	0.714
$Y_s/d_{N\,\mathrm{eff}}$	0.362	0.362	0.362	0.362	0.362	0.362	0.362	0.362	0.362	0.362	0.362	0.362	0.362	0.362	0.362
$A_D/d_{N^2\,\mathrm{eff}}$	2.04	2.04	2.04	2.04	2.04	2.04	2.04	2.04	2.04	2.04	2.04	2.04	2.04	2.04	2.04

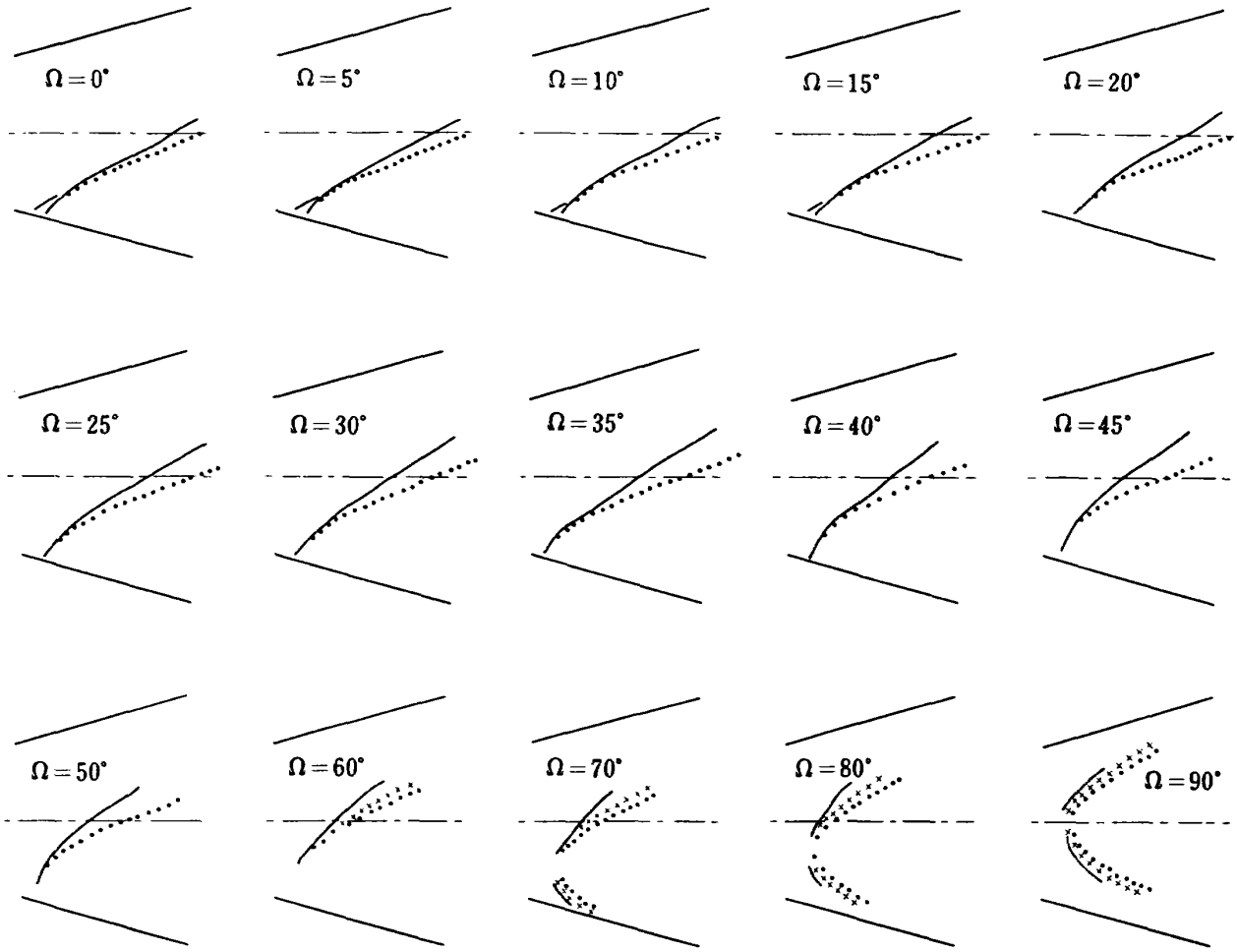

Fig. 2.22 A series of evolved leading shocks in the object co-ordinates (Rotatable type conical lens).

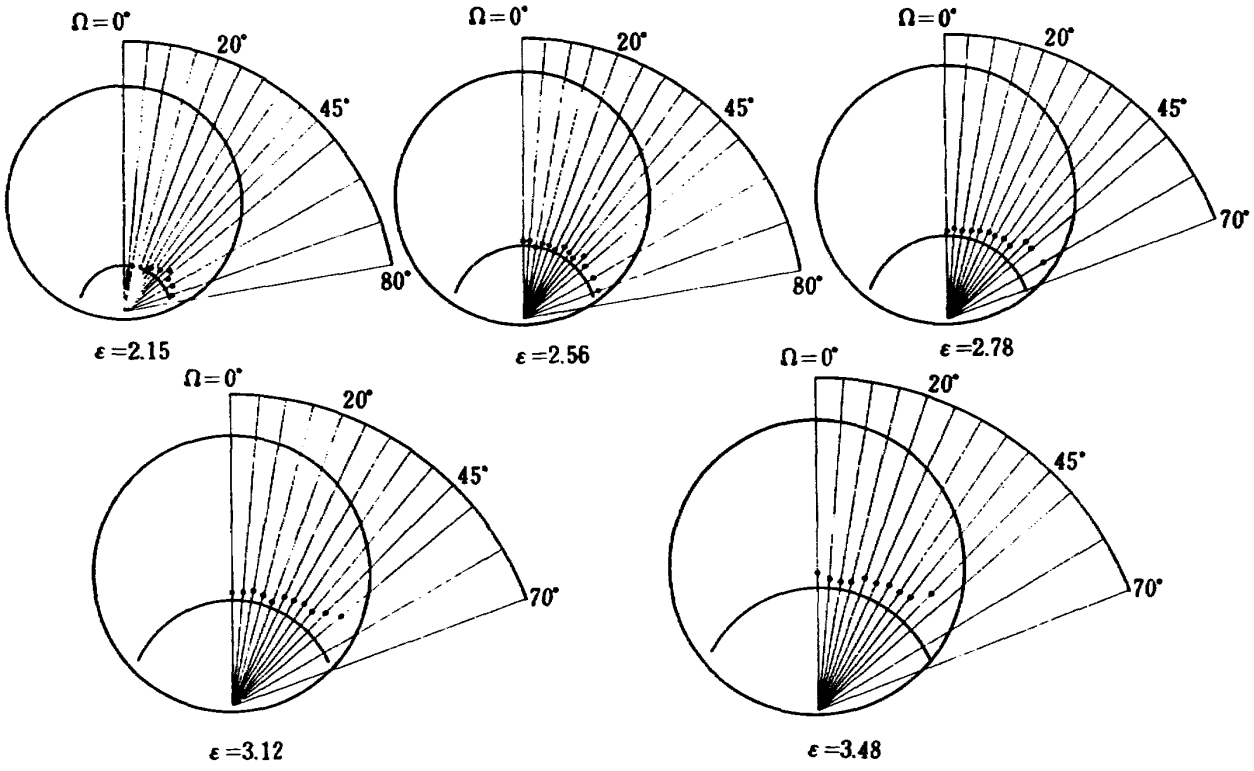

Fig. 2.23 Cross sectional views of leading shocks.

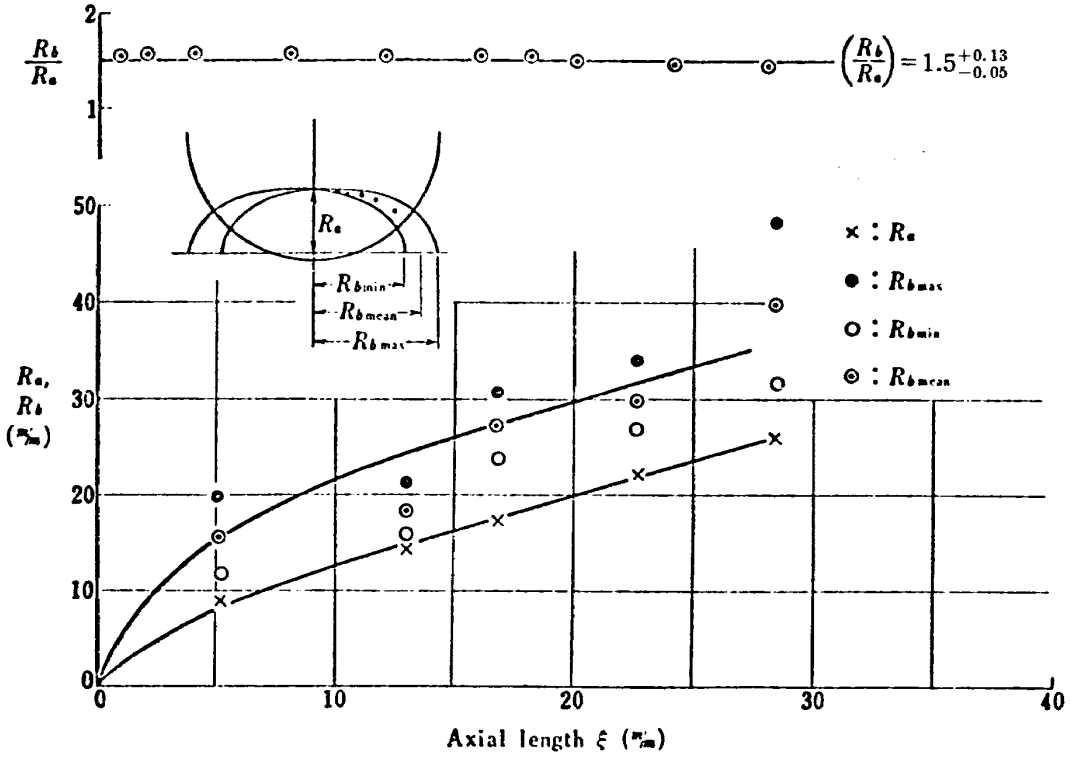

Fig. 2.24 Oblateness of induced shocks.

"it is not clear whether the shock surface can be assumed to be axisymmetrical".

3. AN ESTIMATION OF CONTROL FORCES PRODUCED BY SECONDARY GAS INJECTION AND GITVC EXPERIMENT

Nomenclature

A_D =frontal area of the jet from the injection nozzle exit to the first Mach disc
A_j =area of injection nozzle exit
A^7 $=2\int_{\xi=\xi_0}^{\xi=\xi_{ex}}[R(\xi+Y_s)-R(\xi)]d\xi$
a_M =semiminor axis of main ellipsoid
b_M =semimajor axis of main ellipsoid
d_N =diameter of injection nozzle exit
$d_{N\,\mathrm{eff}}$ =effective diameter of injection nozzle exit
F_m =axial thrust of rocket motor
F_s =measured side force of SITVC test
F_{th} =theoretical side force of SITVC test
F_1 =generated side force by pressure increase in separated region
F_2 =generated side force by pressure increase between separated shock and separated region ahead of detached shock
F_3 =generated side force by pressure increase in aft-detached region ahead of injection flow
F_4 =generated side force by pressure increase acting on injection nozzle exit
F_5 =generated side force by injection flow reaction
F_6 =generated side force by pressure increase in interference region of downstream flow
$\sum F$ =total produced control force by SITVC
M_N =Mach Number at injection nozzle exit
P_{c0} =total pressure of main stream
P_{j0} =total pressure of injection flow
P_j =static pressure of injection flow at injection nozzle exit
P_s =static pressure of turbulent boundary layer separation
P_{st} =aft-detached shock pressure ahead of injection flow
$\bar{P}_{st}$ $=\{(2P_s+P_{st})/3+(2P_s+P_j)/3\}/2$; average pressure in aft-detached shock region
P_1 =static pressure of region 1
P_2 =static pressure of the aft-separation region
$\bar{P}_2$ =average pressure between separation shock and separated turbulent boundary layer
R =cylindrical blast wave radius
T_{0j} =total temperature of injection flow
v_j =injection jet velocity at injection nozzle exit
$\dot{w}_j$ =weight flow rate of injectant
x_p =penetrating length of injectant
$(x, y)_{0M}$ =apex of main ellipsoid
Y_s =distance between separation shock apex

and detached shock front
α_N =half angle of rocket nozzle
γ =specific heats ratio of main flow gas
γ_j =specific heats ratio of injectant gas
Δ_{0M} =shock standoff distance from main ellipsoid
δ_I =injection angle to the cross section of rocket nozzle
δ_N =half angle of injection nozzle at exit
δ_s =turning angle of separated flow
ε_e =rocket nozzle expansion ratio at exit
ε_j =rocket nozzle expansion ratio at injection point
ξ_0 =cylindrical blast wave axial length at the beginning of region 7
ξ_{ex} =cylindrical blast wave axial length at rocket nozzle exit
σ =angle of oblique shock to incoming flow

Under-expanding gas injection flow, which is subjected to the dynamic pressure of supersonic main stream, complicated flow-field ahead of the injection flow and the induced leading shock waves were analysed and compared with the results of flow visualization, in the previous two sections. The analysis showed pretty well correlation with the experimental results. Based on the above analysis, it is tried to estimate produced control forces of GITVC in this section. Disturbed flow regions, considered especially to contribute the additional generation of side forces due to secondary gas injection, are shown schematically in Fig. 3.1.

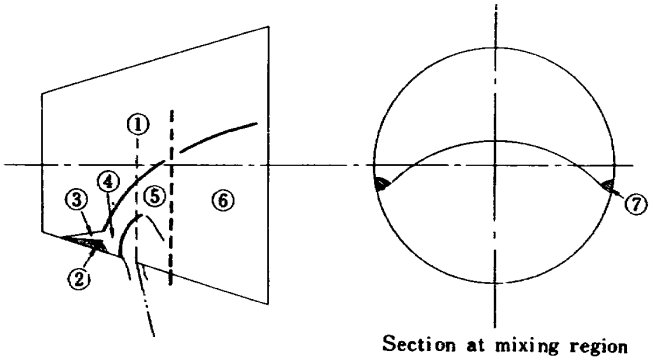

Fig. 3.1 Regions contributed to forces.

Region 1 shows undisturbed nozzle flow, 2 shows separated turbulent boundary layer region ahead of detached shock induced by injection flow obstruction, 3 shows oblique shock region by the separation, 4 shows aft-detached shock region ahead of injection flow obstruction, 5 shows over-expanding region of injection flow, 6 shows mixing region in the downstream, and 7 shows interference region between leading shock and the turbulent boundary layer on the nozzle wall to the exit section. The configuration of each region can be calculated from the previous two sections.

The static pressure of region 1, P_1, can be calculated from isentropic relation of one-dimensional nozzle flow. The separation agles, δ_s, the separation pressure, P_s, the oblique shock angle due to separation, σ, and the aft-separation shock pressure, P_2, can be calculated from the Mager's analysis and the oblique shock wave relations. The pressure decrease of over-expanding region 5 is assumed approximately to balance the pressure increase due to the leading shock recompression and weak recompression along the jet boundary and further the interference region between turbulent boundary layer and the leading shock wave.

Zukoski and Spaid[14] showed from their experiment that the pressure of region 6 was almost equivalent to the undisturbed flowfield. Fig. 3.2 shows a typical GITVC test run of two-dimensional nozzle flow, measuring static pressures of the disturbed and the undisturbed flows. Fig. 3.2 (a) shows a schlieren photograph showing positions of static pressure measuring ports. Fig. 3.2 (b) shows static pressures of the disturbed flows of the experiment of (a). If static pressures of the undisturbed flow, #3 to #6, are compared with the static pressures of the disturbed flow, #3′ to #6′, respectively, the experiperiment of Zukoski and Spaid is assured by Fig. 3.2. Therefore, no contribution of the region 6 was considered. Region 7 may be only contribution to the generation of control force after over-expanding region. The pressure, P_7, may be calculated by the Mager's model.

The area on which the pressure difference acts to cause the control force, in the regions of 2 and 3, is bounded by the intersection of a separation shock cone and separated turbulent boundary layer region of cone with the conical wall of the nozzle. For simplicity, the projected area bounded by a separation shock cone and a nozzle cone is calculated by cone and cylinder presented by Wu, Chapkis, and Mager[1]. This simplification is valid as long as the nozzle cone is small. For estimation of area, A_7, an analytical model of Fig. 3.3 is considered. Therefore,

$$A_7=2\int_{\xi=\xi_0}^{\xi=\xi_{ex}}[R(\xi+Y_s)-R(\xi)]d\xi \qquad (3.1)$$

Now, six forces contibuting to the production of control force by GITVC are as follows:

$$F_1=(P_s-P_1)Y_s^2\tan\delta_s\cos\alpha_N\,; \qquad (3.2)$$

pressure increase in separated region.

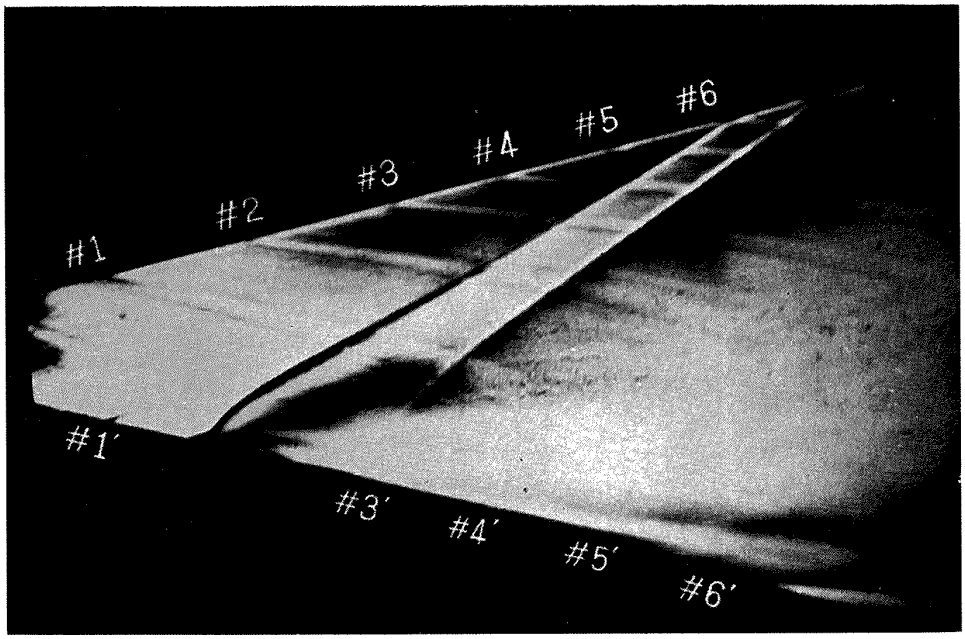

(a)

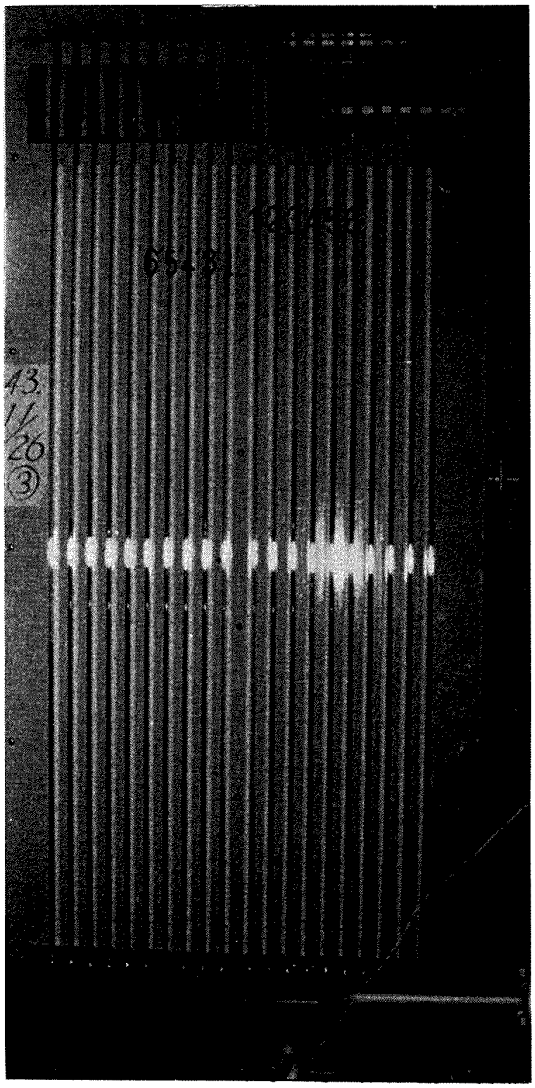

(b)

Fig. 3.2

(a) Schlieren photograph of GITVC by two-dimensional nozzle flow.
(b) Static pressures of disturbed and undisturbed flows.

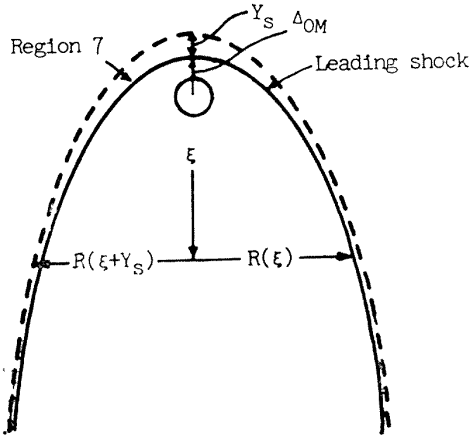

Fig. 3.3 Estimation of area A_7.

$$F_2=(\bar{P}_2-P_1)\{Y_s^2(\tan\sigma-\tan\delta_s)\}\cos\alpha_N\ ; \quad (3.3)$$

pressure increase between separation shock and separated region ahead of detached shock.

$$F_3=(\bar{P}_{st}-P_1)\{(\Delta_{0M}+y_{0M})^2\pi/2-A_j/2\}\cos\alpha_N\ ; \quad (3.4)$$

pressure increase in aft-detached shock region ahead of injection flow.

$$F_4=(P_j-P_1)A_j\cos\delta_I\ ; \quad (3.5)$$

pressure difference acting on injection nozzle exit area.

$$F_5=\dot{w}_j v_j/g\cdot\cos\delta_I\ ; \quad (3.6)$$

reaction of injectant.

$$F_6=(P_s-P_1)A_7\ ; \quad (3.7)$$

pressure increase in interference region 7.

Total produced control force is,

$$\sum F=F_1+F_2+F_3+F_4+F_5+F_6$$

where Y_s is the distance of separated region along the wall, y_{0M} is the apex of main ellipsoid, A_j is the injection nozzle exit area, $\dot{w}_j$ is the injectant weight flow rate, and A_7 is the area of interference region 7, projected to the nozzle axis plane perpendicular to the injection direction. The average pressures are derived by an assumption of parabolic distribution profile as follows:

$$\bar{P}_2=(2P_s+P_2)/3\ ,$$

and

$$\bar{P}_{st}=\{(2P_s+P_{st})/3+(2P_s+P_j)/3\}/2$$

GITVC experiment was conducted by using 4-components thrusts measuring stand (axial force, pitching, yawing, and rolling moments). Fig. 3.4 shows the test stand. The solid propellant rocket motors were used for the test. The average thrust of the tested rocket motors was about 300 kg. N_2 gas was used as an injectant. The tested conditions and the theoretically calculated control forces by the previously discussed estimation method are listed in Table 3.1. In the theoretical calculations, the second type flow of disturbance as stated in the first section of the present study was assumed, for the lack of information of turbulent boundary layer thickness of the present case. The difference between the measured control force, F_s, and the theoretically calculated force, F_{th}, are about 30 percent in the range of $F_s/F_m=0.01$ and about 60 percent in the small range of $F_s/F_m=0.005$, where F_m is main axial thrust. This may be caused by an invalid assumption of second type disturbance for the small quantity of injection rate and also by the side force measuring technique. The thrust misalignment may be predominant in these small thrust level rockets. A 6-components thrusts measuring stand may be needed to measure the accurate produced control forces.

Because the conducted experiment was limited, the results of GITVC tests conducted by NASA[23] were compared with the theoretical calculation. Tables 3.2-3.5 show the GITVC conditions, the

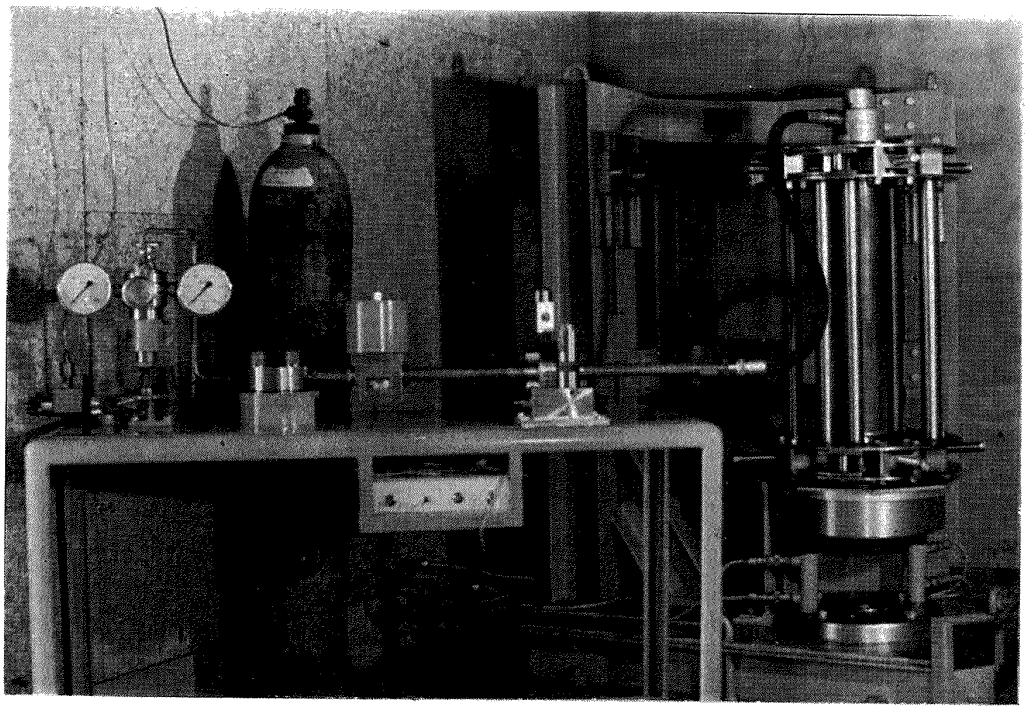

Fig. 3.4 GITVC test on vertical 4-components thrust measuring stand.

Table 3.1 GITVC test and calculated control forces

Rocket motor throat dia.=20.7 mm, $\varepsilon_j=4.63$, $\varepsilon_e=8$
Average axial thrust=311 kg, $\alpha_N=7.5°$, $\gamma=1.17$

Injectant: N_2, Sonic and vertical, $T_{0j}=288°K$, $d_n=2$ mm, $\sigma=48°27'$, $\delta_s=29°19'$, $P_s/P_1=2.17$, $P_2/P_1=4.261$, $P_{st}/P_1=7.667$

GITVC conditions					Calculated injection flow parameters								Control forces (Theoretical)						
P_{c0} kg/cm² ab	P_{j0} kg/cm² ab	$\dot{w}_j$ kg/s	$d_{N\,\mathrm{eff}}$ m/m	F_s kg	$\frac{\Delta_{0M}}{d_{N\,\mathrm{eff}}}$	$\frac{y_{0M}}{d_{N\,\mathrm{eff}}}$	$\frac{x_{0M}}{d_{N\,\mathrm{eff}}}$	$\frac{X_p}{d_{N\,\mathrm{eff}}}$	$\frac{Y_s}{d_{N\,\mathrm{eff}}}$	$\frac{A_d}{d_{N\,\mathrm{eff}}^2}$	$\frac{a_M}{d_{N\,\mathrm{eff}}}$	$\frac{b_M}{d_{N\,\mathrm{eff}}}$	F_1 kg	F_2 kg	F_3 kg	F_4 kg	F_5 kg	F_6 kg	ΣF kg
67.2	41.5	0.0275	1.921	2.97	0.269	0.638	0.464	0.791	0.412	2.250	0.724	1.112	0.0103	0.0165	0.4337	0.6294	0.9050	0.0097	2.00
65.5	52.0	0.0350	1.933	3.71	0.340	0.731	0.698	1.128	0.619	3.425	0.793	1.351	0.0230	0.0369	0.7569	0.7269	1.1533	0.0108	2.71
62.2	31.0	0.0190	1.847	1.98	0.210	0.586	0.324	0.556	0.287	1.518	0.678	0.945	0.0043	0.0069	0.2162	0.3725	0.6261	0.0072	1.23
63.0	21.0	0.0140	1.661	1.50	0.125	0.531	0.145	0.254	0.129	0.612	0.600	0.681	0.0007	0.0011	0.0621	0.1867	0.3427	0.0035	0.596
61.2	27.0	0.0145	1.300	1.84	0.179	0.565	0.256	0.460	0.227	1.190	0.650	0.731	0.0013	0.0021	0.0803	0.1572	0.4778	0.0046	0.723
59.5	35.5	0.0205	1.794	2.75	0.261	0.628	0.499	0.749	0.398	2.106	0.724	1.094	0.0075	0.0119	0.4306	0.4135	0.6755	0.0084	1.655

Table 3.2 GITVC test and calculated control forces (Test No. 1 of Ref. 23)

Rocket motor throat dia.=1.955 in., $\varepsilon_j=4.60$, $\varepsilon_e=8$
Average axial thrust=2870 lb, $\alpha_N=15°$, $\gamma=1.17$

Injectant: Hot gas, Sonic and vertical, $T_{0j}=1630°F$, $d_N=0.3066$ in., $\gamma_j=1.17$, $P_s/P_1=2.201$, $P_2/P_1=4.349$, $P_{st}/P_1=7.966$, $M_N=1.0$, $\sigma=47°54'$, $\delta_s=29°12$

GITVC conditions					Calculated injection flow parameters								Control forces (Theoretical)							
P_{00} psia	P_{j0}^1 psia	P_{j0}^2 psia	$\Delta\dot{w}_j$ lb/s	F_s lb	$\frac{\Delta_{0M}}{d_N}$	$\frac{y_{0M}}{d_N}$	$\frac{x_{0M}}{d_N}$	$\frac{X_p}{d_N}$	$\frac{Y_s}{d_N}$	$\frac{A_d}{d_N^2}$	$\frac{a_M}{d_N}$	$\frac{b_M}{d_N}$	F_1 lb	F_2 lb	F_3 lb	F_4 lb	F_5 lb	F_6 lb	ΣF lb	$\pm F$th lb
590	499	351	0.107	25	0.404 0.283	1.147 0.819	1.152 0.693	1.519 0.906	0.445 0.207	5.093 2.731	1.054 0.918	1.697 1.310	0.247 0.053	0.087 0.084	22.653 16.164	19.542 12.847	8.115	0.069 0.006	50.575 29.154	21.42
590	291 81		0.158	36	0.238 —	0.722 —	0.529 —	0.682 —	0.136 —	1.948 —	0.859 —	1.140 —	0.023 —	0.036 —	9.950 —	10.403 1.914	11.98	0.014 —	32.405 —	30.49
590	303 71		0.170	36	0.332 —	0.740 —	0.549 —	0.735 —	0.141 —	2.138 —	0.859 —	1.162 —	0.026 —	0.040 —	13.877 —	11.231 1.493	12.893	0.0098 —	38.076 —	36.58
590	53 325		0.196	45	— 0.267	— 0.775	— 0.615	— 0.814	— 0.171	— 2.410	— 0.887	— 1.232	— 0.037	— 0.057	— 13.090	11.789 0.733	14.865	— 0.0098	— 39.848	39.12

Table 3.3 GITVC test and calculated control forces (Test No. 2 of Ref. 23)

Rocket motor throat dia.=2.065 in, $\varepsilon_j=4.60$, $\varepsilon_e=8$
Average axial thrust 3000 lb, $\alpha_N=15°$, $\gamma=1.17$

Injectant: Hot gas, Supersonic and vertical, $T_{0j}=1560°$F, $d_N=0.36$ in, $\gamma_j=1.17$, $P_s/P_1=2{,}201$, $P_2/P_1=4{,}349$, $P_{st}/P_1=7{,}966$, $M_N=1.833$, $\sigma=47°54'$, $\delta_s=29°12'$

GITVC conditions					Calculated injection flow parameters								Control forces (Theoretical)							
P_{c0} psia	P_{j0}[1] psia	P_{j0}[2] psia	$\Delta\dot{w}_j$ lb/s	F_s lb	$\frac{\Delta_{0M}}{d_N}$	$\frac{y_{0M}}{d_N}$	$\frac{x_{0M}}{d_N}$	$\frac{X_p}{d_N}$	$\frac{Y_s}{d_N}$	$\frac{A_d}{d_N^2}$	$\frac{a_M}{d_N}$	$\frac{b_M}{d_N}$	F_1 lb	F_2 lb	F_3 lb	F_4 lb	F_5 lb	F_6 lb	ΣF lb	$\pm F$th lb
645	702		0.504	105	0.433	0.994	1.001	0.984	0.339	2.092	1.690	2.146	0.223	0.182	31.949	10.259	63.296	−0.074	105.86	103.52
		79			—	—	—	—	—	—	—	—	—	—	—	2.340		—	—	
645	748		0.533	115	0.433	1.056	1.098	1.080	0.397	2.330	1.762	2.260	0.297	0.456	38.377	11.080	66.930	−0.070	117.07	115.60
		64			—	—	—	—	—	—	—	—	—	—	—	1.467		—	—	
645	798		0.584	130	0.479	1.129	1.205	1.180	0.425	2.551	1.830	2.390	0.339	0.522	45.768	11.968	73.340	−0.097	131.84	132.01
		36			—	—	—	—	—	—	—	—	—	—	—	−0.171		—	—	
645	825		0.583	135	0.498	1.169	1.282	1.245	0.478	2.699	1.905	2.482	0.430	0.661	51.096	12.451	73.210	−0.124	137.72	137.95
		35			—	—	—	—	—	—	—	—	—	—	—	−0.229		—	—	
645	843		0.591	139	0.499	1.198	1.309	1.271	0.490	2.755	1.905	2.505	0.452	0.695	53.713	12.770	74.221	−0.133	141.72	142.13
		32			—	—	—	—	—	—	—	—	—	—	—	−0.405		—	—	
645	857		0.589	142	0.489	1.220	1.330	1.273	0.499	2.728	1.905	2.523	0.468	0.721	55.551	13.012	73.970	−0.137	143.57	143.92
		33			—	—	—	—	—	—	—	—	—	—	—	−0.346		—	—	

Table 3.4 GITVC test and calculated control forces (Test No. 3 of Ref. 23)

Rocket motor throat dia.=2.050 in, $\varepsilon_j=4.90$, $\varepsilon_e=8$
Average axial thrust 2550 lb, $\alpha_N=15°$, $\gamma=1.17$

Injectant: Hot gas, Sonic and vertical, $T_{0j}=1{,}885°$F, $d_N=0.4151$ in, $\gamma_j=1.17$, $P_s/P_1=2.201$, $P_2/P_1=4.349$, $P_{st}/P_1=7.966$, $M_N=1.0$, $\sigma=47°54'$, $\delta_s=29°12'$

GITVC conditions					Calculated injection flow parameters								Control forces (Theoretical)							
P_{c0} psia	$P_{j0}{}^1$ psia	$P_{j0}{}^2$ psia	$\Delta\dot{w}_j$ lb/s	F_s lb	$\frac{\Delta_{0M}}{d_N}$	$\frac{y_{0M}}{d_N}$	$\frac{x_{0M}}{d_N}$	$\frac{X_p}{d_N}$	$\frac{Y_s}{d_N}$	$\frac{A_a}{d_N{}^2}$	$\frac{a_M}{d_N}$	$\frac{b_M}{d_N}$	F_1 lb	F_2 lb	F_3 lb	F_4 lb	F_5 lb	F_6 lb	ΣF lb	$\pm F$th lb
523	15	493	0.607	159	0.437	1.311	1.333	1.733	0.548	5.890	1.093	1.821	0.609	0.952	101.94	34.461	48.769	−0.254	186.48	187.76
					—	—	—	—	—	—	—	—	—	—	—	−1.279		—	—	
523	509	15	0.605	162	0.465	1.367	1.425	1.809	0.571	6.201	1.133	1.892	0.661	1.034	116.09	35.658	48.608	−0.283	201.76	203.04
					—	—	—	—	—	—	—	—	—	—	—	−1.279		—	—	
523	94	415	0.386	96	0.387	1.068	1.041	1.371	0.380	4.476	1.018	1.610	0.293	0.382	61.943	28.637	31.013	−0.122	122.15	117.32
					—	—	—	—	—	—	—	—	—	—	—	4.827		—	—	
523	377	125	0.301	79	0.357	0.967	0.909	1.197	0.311	3.805	0.983	1.504	0.196	0.256	46.386	25.798	24.183	−0.077	96.74	89.52
					—	—	—	—	—	—	—	—	—	—	—	7.224		—	—	
523	282	220	0.072	20	0.254	0.764	0.603	0.778	0.168	2.259	0.887	1.220	0.057	0.074	19.991	18.704	5.784	−0.008	41.60	16.65
					—	0.662	0.410	0.531	0.087	1.451	0.805	1.003	0.015	0.020	10.868	18.942		−0.107	24.95	
523	495	26	0.575	152	0.448	1.318	1.385	1.740	0.551	5.912	1.133	1.870	0.638	0.804	103.49	34.613	46.198	−0.263	185.48	185.91
					—	—	—	—	—	—	—	—	—	—	—	−0.429		—	—	

Table 3.5 GITVC test and calculated control forces (Test No. 4 of Ref. 23)

Rocket motor throat dia.=2.048 in, $\varepsilon_j=3.77$, $\varepsilon_e=8$
Average axial thrust 2600 lb, $\alpha_N=15°$, $\gamma=1.17$

Injectant: Hot gas, Supersonic and vertical, $T_{0j}=1915°F$, $d_N=0.4008$ in, $\gamma_j=1.17$, $P_s/P_1=2.074$, $P_2/P_1=3.944$, $P_{st}/P_1=6.666$, $M_N=1.398$, $\sigma=50°36'$, $\delta_s=29°$

GITVC conditions					Calculated injection flow parameters								Control forces (Theoretical)							
P_{c0} psia	$P_{j0}{}^1$ psia	$P_{j0}{}^2$ psia	$\Delta\dot{w}_j$ lb/s	F_s lb	$\frac{\Delta_{0M}}{d_N}$	$\frac{y_{0M}}{d_N}$	$\frac{x_{0M}}{d_N}$	$\frac{X_p}{d_N}$	$\frac{Y_s}{d_N}$	$\frac{A_d}{d_N{}^2}$	$\frac{a_M}{d_N}$	$\frac{b_M}{d_N}$	F_1 lb	F_2 lb	F_3 lb	F_4 lb	F_5 lb	F_6 lb	ΣF lb	$\pm F$th lb
533		469	0.448	106	0.397	1.011	0.916	0.884	0.315	2.801	1.263	1.681	0.263	0.498	46.85	16.980	48.85	0.036	113.49	113.81
	75				—	—	—	—	—	—	—	—	—	—	—	−0.324		—	—	
533	395	175	0.226	57	0.340	0.850	0.708	0.654	0.209	1.977	1.173	1.479	0.116	0.220	29.66	13.263	24.64	0.067	67.97	63.90
					—	—	—	—	—	—	—	—	-	—	—	4.069		—	—	
533	100	476	0.399	98	0.407	1.029	0.931	0.899	0.322	2.845	1.263	1.691	0.274	0.434	48.73	17.245	43.50	0.031	110.26	109.49
					—	—	—	—	—	—	—	—	—	—	—	0.774		—	—	
533	353	239	0.114	28	0.297	0.774	0.581	0.532	0.163	1.558	1.091	1.334	0.071	0.134	21.30	11.890	12.43	0.071	45.89	30.50
					0.192	0.623	0.312	0.245	0.050	0.640	0.916	0.973	0.007	0.012	8.45	6.881		0.036	15.39	
533	600	29	0.604	156	0.814	1.388	1.322	1.300	0.547	4.330	1.414	2.009	0.793	1.500	98.70	22.743	65.86	−0.179	189.42	187.07
					—	—	—	—	—	—	—	—	—	—	—	−2.344		—	—	
533	260	396	0.194	50	0.340	0.852	0.710	0.656	0.210	1.982	1.173	1.811	0.121	0.221	29.11	13.780	21.15	0.066	64.45	53.03
					0.160	0.591	0.242	0.157	0.025	0.345	0.857	0.859	0.002	0.003	5.96	5.431		0.020	11.42	

calculated injection flow parameters, and the estimated control forces by the theory. These tests were conducted on 6-components thrusts measuring stands. The average axial thrust of the tested solid propellant rocket motors was about 3000 lbs. Hot gas was used as an injectant, which was generated by solid propellant gas generator assembly. Injection was done through oppositely located couple ports by a proportional hot valve, and the control forces were generated by the difference of injectant weight flows, $\Delta\dot{w}_j$. The injection was vertical to the rocket nozzle axis, and was sonic (Tables 3.2 and 3.4) and supersonic (Tables 3.3 and 3.5). Because couple opposite injections were done, each produced control force was calculated, and the summed forces in each direction were compared with the measured side forces.

The theoretically calculated control forces of Tables 3.2-3.5 show good agreement with the experimental results. From the estimation, it can be concluded that the contribution of the separation regions (say, F_1, F_2, and F_6) to the production of control force might be under one percent of the total. The major part of the produced control force might be generated by F_3, F_4, and F_5 in GITVC.

4. LITVC EXPERIMENT AND AN ESTIMATION OF PRODUCED CONTROL FORCES OF LITVC

Nomenclature

A_j =area of injection nozzle exit
C_{Dx} =aerodynamic drag coefficient to x directional flow
C_{Dy} =aerodynamic drag coefficient to y directional flow
d_b =blunt nose diameter
d_L =diameter of injected droplet in liquid phase
d_{L+G} =diameter of injected droplet surrounded by vaporized gas
d_N =diameter of injection nozzle exit
$d_{N\,\mathrm{eff}}$ =effective diameter of injection nozzle exit
F_1 =side force produced in the detached shock region
F_2 =side force produced by injection reaction
F_3 =side force produced by injection pressure
F_4 =side force produced by recompression through leading shock
F_5 =side force produced in the injectant mixing flow
g =acceleration of gravity
M_1 =Mach Number of undisturbed main flow
M_2 =Mach Number of aft-leading shock flow
M_∞ =Mach Number of free stream
P_1 =static pressure of undisturbed main flow
P_2 =static pressure of aft-leading shock wave
P_{c0} =total pressure of main stream
P_{j0} =total pressure of injection flow
P_j =static pressure at injection nozzle exit
P_s =separation pressure
P_{st} =aft-detached shock pressure ahead of injection obstruction
Pr =Prandtl Number
Re =Reynolds Number
T_{c0} =total temperature of main stream
T_{j0} =total temperature of injection flow
t =time
u_∞ =horizontal velocity of free stream
v_j =jet velocity at injection nozzle exit
$\dot{w}_j$ =weight flow rate of injectant
x, y =co-ordinates of injectant trajectory
x_L, y_L =trajectory of injectant droplet
X_L, Y_L =enveloped surface of injectant trajectory
$(x, y)_{0M}$ =apex of main ellipsoid
Y_s =distance between separation shock apex and detached shock
α_N =half angle of rocket conical nozzle
γ =specific heats ratio of main stream gas
Δ_{0M} =shock standoff distance from main ellipsoid
δ_b =tangent of eveloped surface of liquid injectant
δ_I =injection angle to the cross section of rocket nozzle
δ_L =turning angle across leading shock wave
δ_s =turning angle of separated flow
ε_e =rocket nozzle expansion ratio at exit
ε_j =rocket nozzle expansion ratio at injection point
θ_r =half circular arc angle between couple injections
λ_L =evaporation rate for laminar flow
λ_T =evaporation rate for turbulent flow
ξ_L, η_L =co-ordinates of leading shock shape
ρ_G =density of injectant droplet in gas phase
ρ_j =density of injectant at injection nozzle exit
ρ_∞ =density of free stream
σ =angle of separation shock to incoming flow
σ_L =angle of the leading shock wave to incoming flow

LITVC is a little different in the control force producing mechanism from that of GITVC. In order to determine the shape of injected flow pattern, atomization and vaporization processes must be investigated for non combustible liquid

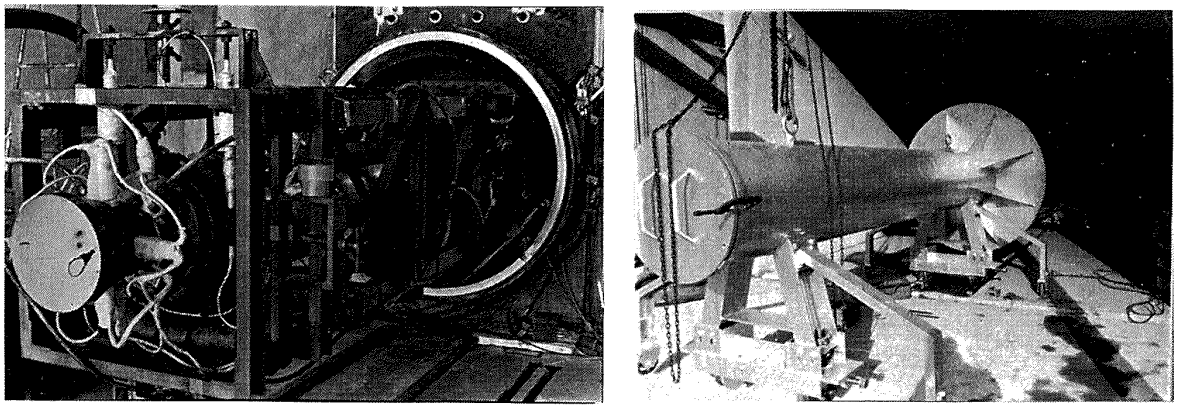

(a) (b)

Fig. 4.1 LITVC test apparatus of the first series.

injectant. Because the investigation of flow pattern of the liquid injection has not yet been tried in the present study, a reasonable analytical model of injection flow such as gas injection stated in the previous sections can not be presented here. Several estimation methods of LITVC have been reported[1],[4]. However, the complicated flowfield induced by LITVC has not been enough investigated. Therefore, some LITVC experiment was conducted and a simpler estimation of produced control forces is tried in this section, the present estimation method is essentially the same of Sehgal and Wu[4].

LITVC test runs were conducted by injecting Freon 114B2 on multi-components thrusts measuring stands. The first series of test runs were conducted on a horizontal 4-components thrusts measuring stand. Fig. 4.1 (a) and (b) show LITVC test apparatus of the first series. The average thrust of tested solid propellant rocket motor was about 5250 kg, nozzle throat diameter was 93 mm, nozzle half cone angle was 18°, and the exit expansion ratio was 15. Because high expansion ratio to the combustion pressure (average 45.6 kg/cm² ab), the cylindrical diffuser for high altitude simulation was set after rocket nozzle exit and the horizontal 4-components thrusts measuring stand was built in a cylindrical vacuum chamber (1.5 m in diameter × 3.5 m in length). Before ignition of the tested rocket, the chamber was exhausted to 10 mm Hg and the pressure of 40 mm Hg was kept during the firing test by the self diffusion effect of the exhausted gas. Freon 114B2 was injected through couple of ports spaced 40 mm in a circle of nozzle at one quadrant, directed to the rocket nozzle axis. The properties of injectant are listed in Table 4.1. The tested conditions and the measured control forces, F_s, are listed in Table 4.2.

The second and the third series of LITVC test runs were conducted on a horizontal 4-components thrusts measuring stand (Fig. 4.2) and on a horizontal 6-components thrusts measuring stand (Fig. 4.3), respectively. The average thrust of tested solid propellant rocket motor was about 5300 kg, nozzle throat diameter was 93 mm, nozzle half cone angle was 15°, and the exit expansion ratio was 10. The test runs of the second and the third series were done in sea level atmosphere condition. Injectant also was Freon 114B2. In the third series of the test, LITVC feed system was integrated around rocket nozzle as an on-board type (see Fig. 4.3). The tested conditions and the measured control forces, F_s, of the second and the third series are listed in Table 4.3, where * mark shows that of the third series of the test.

Table 4.1 Physical properties of Freon 114B2

Chemical formula	$CBrF_2 \cdot CBrF_2$
Molecular weight	259.9
Boiling point	47.5°C
Solidification point	−110.5°C
Specific gravity (22°C)	2.20
Viscosity (20°C)	0.76 CP
Specific heat	0.18 cal/gr°C
Heat of vaporization	25 cal/gr
Critical temperature	214.5°C
Critical pressure	35.9 kg/cm²ab
Gas density (air=1)	7.3
Coefficients of gas expansion	230 vap/liq. vol %

In order to see the difference of control force producing mechanism from the gas injection, a simple analysis to predict the injectant flow pattern is tried. Fig. 4.4 shows an analytical model. A liquid jet penetrates transversely supersonic main stream as a liquid sphere surrounded by vaporized gas. The trace of the vaporizing sphere is considered as a solid obstruction to

Table 4.2 LITVC test and calculated control forces

Rocket motor throat dia.=93 mm, $\gamma=1.3$, $\varepsilon_e=15$
Average thrust=5250 kg, $\alpha_N=18°$, $T_{c0}=3210°K$

Injectant: Freon 114B2, $\delta_I=0°$, $T_{0j}=300°K$
Double holes injection, hole pitch=40 mm

LITVC conditions								Calculated injection flow parameters										Control forces (Theoretical)					
P_{c0} kg/cm²ab	P_{j0} kg/cm²ab	ε_j	$\dot{w}_j$ kg/s	$\cos\theta_r$	d_N mm	$d_{N\,\mathrm{eff}}$ mm	F_s kg	$\frac{\Delta_{0M}}{d_{N\,\mathrm{eff}}}$	$\frac{y_{0M}}{d_{N\,\mathrm{eff}}}$	$\frac{x_{0M}}{d_{N\,\mathrm{eff}}}$	$\frac{Y_s}{d_{N\,\mathrm{eff}}}$	$\frac{d_b}{d_{N\,\mathrm{eff}}}$	$\left(\frac{P_s}{P_1}\right)_j$	$\left(\frac{P_2}{P_1}\right)_j$	$\left(\frac{P_{st}}{P_1}\right)_j$	$(\sigma)_j$ deg	$(\delta_s)_j$ deg	F_1 kg	F_2 kg	F_3 kg	F_4 kg	F_5 kg	ΣF kg
45.6	51	4	0.813	0.978	3	1.940	119.3	0.111	0.501	0.047	≈0	1	2.043	3.673	8.543	41.5	22.5	0.06	5.23	2.90	131	0.50	139.7
45.6	51	6	0.808	0.985	3	1.932	103.4	0.093	0.500	0.054	≈0	1	2.160	3.951	10.95	37.4	21.5	0.06	5.21	2.90	58.4	0.16	63.8
45.6	51	7.5	0.960	0.988	3	2.104	104.8	0.085	0.499	0.0628	≈0	1	2.215	4.074	12.33	35.5	20.9	0.06	6.20	3.50	30.5	0.12	40.4
45.6	51	9	0.977	0.990	3	2.120	86.6	0.078	0.501	0.0185	≈0	1	2.258	4.165	13.56	34.1	20.4	0.06	6.31	3.60	15.8	0.10	25.9
45.5	51	5	1.156	0.982	3.7	2.314	117.0	0.105	0.501	0.0411	≈0	1	2.111	3.835	9.843	39.1	22.0	0.10	7.43	4.20	92.7	0.43	104.9
45.5	51	5	0.697	0.982	2.4	1.796	104.0	0.105	0.501	0.0467	≈0	1	2.111	3.835	9.843	39.1	22.0	0.06	4.48	2.50	88.4	0.22	95.7
45.5	51	5	0.980	0.982	3.0	2.130	137.9	0.105	0.501	0.0120	≈0	1	2.111	3.835	9.843	39.1	22.0	0.08	6.30	3.50	86.7	0.35	96.9
45.5	51	5	0.405	0.982	1.7	1.369	61.0	0.105	0.501	0.0415	≈0	1	2.111	3.835	9.843	39.1	22.0	0.04	2.60	1.50	92.2	0.15	96.5

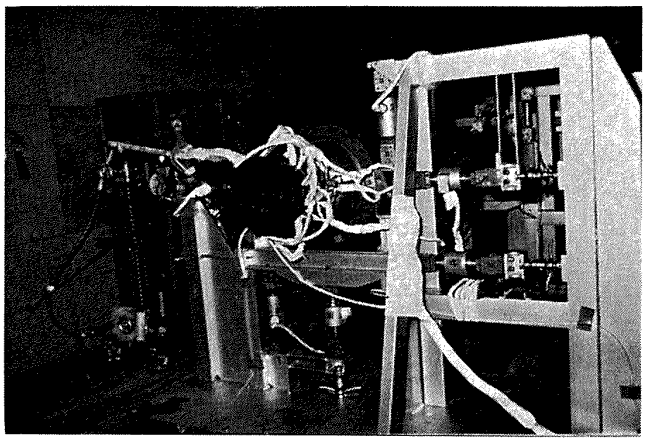

Fig. 4.2 LITVC test of the second series.

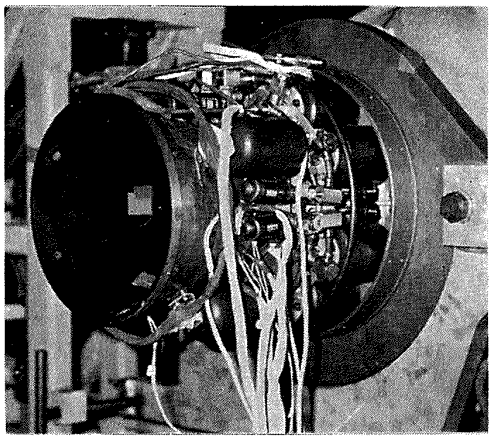

Fig. 4.3 LITVC test of the third series.

Table 4.3 LITVC test and calculated control forces

Rocket motor throat dia.=93 mm Average thrust=5300 kg $\gamma=1.3$, $\varepsilon_e=10$, $\alpha_N=14°44'$, $T_{c0}=3210°K$	Injectant: Freon 114B2 $\delta_I=0°$, $T_{0j}=300°K$ Double holes injection, pitch=36 mm

$\varepsilon_j=3.25$, $\cos\theta_T=0.977$, $\Delta_{0M}/d_{N\,\mathrm{eff}}=0.147$, $y_{0M}/d_{N\,\mathrm{eff}}=0.5$, $Y_s/d_{N\,\mathrm{eff}}=0$, $d_b/d_{N\,\mathrm{eff}}=1$,
$(P_s/P_1)_j=1.98$, $(P_2/P_1)_j=3.52$, $(P_{st}/P_1)_j=7.51$, $(\sigma)_j=43.75°$, $(\delta_s)_j=22.82°$

LITVC conditions							Control forces (Theoretical)					
P_{c0} kg/cm²ab	P_{j0} kg/cm²ab	$\dot{w}_j$ kg/s	d_N mm	$d_{N\,\mathrm{eff}}$ mm	$\frac{x_{0M}}{d_{N\,\mathrm{eff}}}$	F_s kg	F_1 kg	F_2 kg	F_3 kg	F_4 kg	F_5 kg	ΣF kg
46.03	30.0	1.325	3.27	2.747	0.060	197.8	0.34	13.27	3.29	110.8	0.26	128.0
44	30.2	1.328	3.27	2.745	0.059	189.0	0.34	13.30	3.32	105.7	0.25	122.9
54	25.0	1.209	3.26	2.751	0.078	156 *	0.34	11.01	2.66	148	0.28	162.3
51.6	25.0	1.206	3.26	2.748	0.078	158.5*	0.32	10.99	2.67	143.3	0.32	157.6
51.4	25.1	1.212	3.26	2.752	0.077	164.0*	0.32	11.07	2.69	138	0.32	152.4
55.0	25.8	1.269	3.25	2.796	0.071	163.2*	0.36	11.76	2.84	133.4	0.34	148.3
51.2	26.8	1.295	3.25	2.796	0.067	172.3*	0.34	12.23	2.98	122.8	0.34	138.7
50.8	26.9	1.298	3.25	2.797	0.067	177.2*	0.34	12.29	3.00	120.8	0.34	136.8

* Conducted on the 6-components thrusts measuring stand.

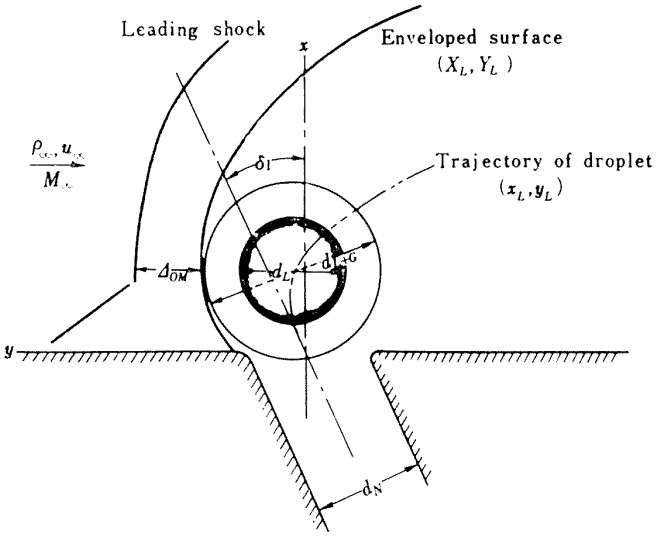

Fig. 4.4 Schematic of LITVC flow pattern.

the supersonic main flow. The separation of turbulent boundary layer ahead of injection, the detached shock, and the leading shock are induced by the obstruction.

If the motion of the vaporizing liquid sphere is considered,

$$d_L^2=d_N^2-\lambda_T t \tag{4.1}$$

where d_L is the diameter of droplet in liquid sphere at time t and λ_T is evaporation rate for turbulent flow (mm²/s). The equations of motion in x and y direction are, respectively,

$$\frac{d^2x}{dt^2}=\frac{3}{8}\frac{\rho_G}{\rho_j}C_{Dx}\frac{2(dx/dt)^2}{\sqrt{d_{N\,\mathrm{eff}}^2-\lambda_T t}} \tag{4.2}$$

$$\frac{d^2y}{dt^2}=-\frac{3}{8}\frac{\rho_G}{\rho_j}C_{Dy}\frac{2(u_\infty-dy/dt)^2}{\sqrt{d_{N\,\mathrm{eff}}^2-\lambda_T t}} \tag{4.3}$$

where $\lambda_T=\lambda_L(1+0.276Re^{1/2}Pr^{1/3})$ and $\lambda_L=1.2077$ mm²/s was used to Freon 114B2. C_{Dx} and C_{Dy} are given by Eqs. (1.8.a) and (1.8.b).

From continuity equation

$$\frac{d_{L+G}}{2}=\sqrt[3]{\left(\frac{d_L}{2}\right)^3+\left\{\left(\frac{d_{N\text{eff}}}{2}\right)^3-\left(\frac{d_L}{2}\right)^3\right\}\frac{\rho_j}{\rho_G}} \tag{4.4}$$

Equations (4.1)-(4.4) give the trajectory of the injected droplet and the diameter d_{L+G}. Thus, an envelope of external surface of the injectant, (X_L, Y_L), can be given.

The trajectory of the injected droplet and the envelope of the vaporizing liquid sphere for Freon 114B2 at the tested LITVC condition (Tables 4.2 and 4.3) was calculated on an electronic computer (HITAC 5020). As the atmization process of Freon 114B2 is not well understood, a droplet with the jet diameter is simply supposed. The motion and the growing diameter of the vaporizing liquid sphere were calculated by considering the effect of the side-wise supersonic main flow and the heat transfer from the hot main flow. An example of the calculated result is shown in Fig. 4.5. It shows that the vaporization is negligible at the location of the downstream side edge of the injection hole (the passed time from the injection is about 1×10^{-6} seconds), therefore the diameter of the vaporizing droplet is assumed here to be constant at that location. Then, the droplet is sharply turned by the side-wise supersonic main flow and became almost parallel to the main flow direction at the passed time of about 4×10^{-5} seconds (about 10 cm downstream).

Thus, one can reasonably regard the droplet with the jet diameter as the blunt nose in the case of Freon 114B2 LITVC, i.e. $d_b\simeq d_{N\text{eff}}$. $(x, y)_{0M}$ is obtained from the apex point of the envelope of the vaporizing droplet in the main flow direction, and Δ_{0M} also is obtained by the previously mentioned method of section 1. The increases of the pressure in the regions of the separation flow and the separated oblique shock were small even for GITVC, and those of LITVC of Freon 114B2 can be easily supposed to be much smaller because of the sharply turn of the injected jet, that is the penetration of the liquid is smaller than that of the gas jet. The contribution of these regions of LITVC to the control force is neglected here. In order to calculate the pressure increase of the detached region, $(P_s/P_1)_j$ and $(P_{st}/P_1)_j$ were calculated by the same way of section 3.

In addition to the side force produced by the detached shock region,

$$F_1=(\bar{P}_{st}-P_1)\{(\Delta_{0M}+y_{0M})^2\pi/2-A_j/2\}\cos\alpha_N \tag{4.5}$$

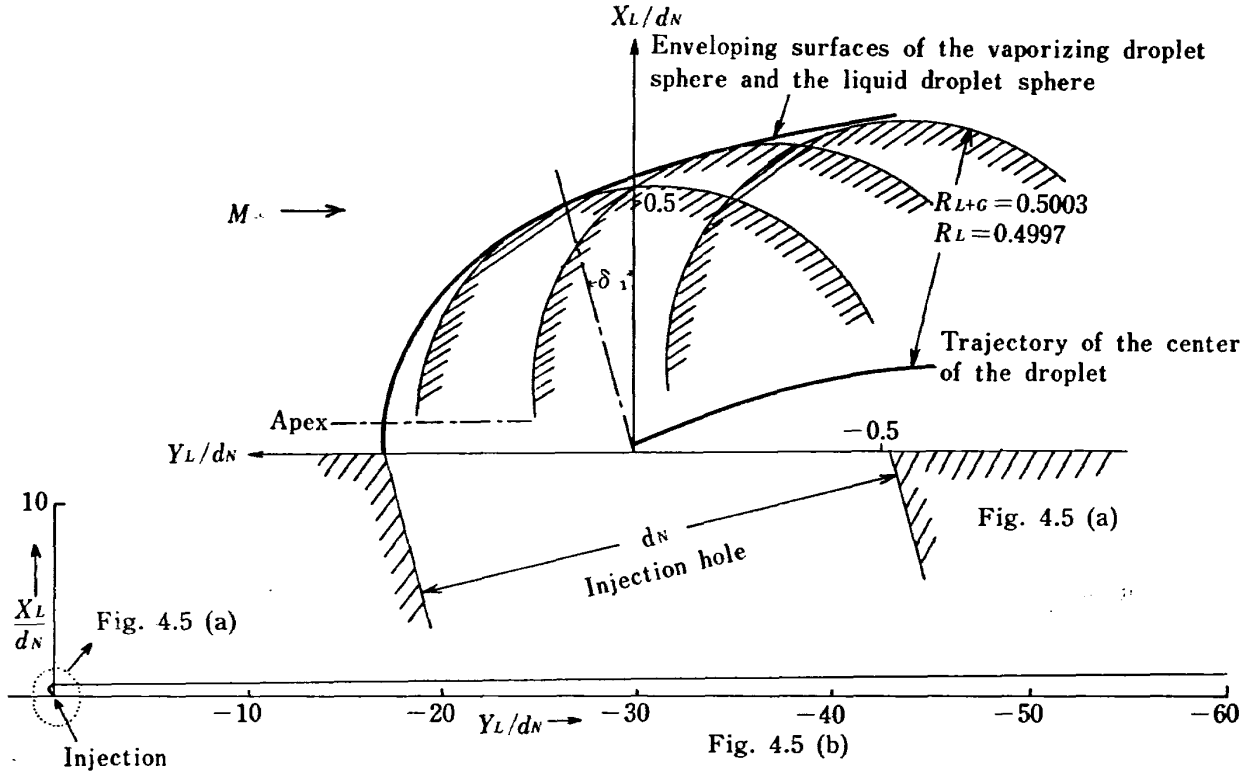

Fig. 4.5

(a) Enlarged envelope surfaces and the trajectory of the vaporizing droplet.
(b) Envelope of the vaporizing droplet.

by the injection reaction

$$F_2=\dot{w}_j v_j/g\cdot\cos\delta_I \tag{4.6}$$

and by the injection pressure

$$F_3=(P_j-P_1)A_j\cos\delta_I \tag{4.7}$$

where $\bar{P}_{st}$ is the same definition of the third section, much part of control force may be produced by recompression through the induced leading shock in the aft-leading shock region, F_4, and by weak recompression or expansion by the flow turning along the injectant mixing region, F_5. Fig. 4.6 shows a recompression process of the region.

From Eqs. (4.1)-(4.4), one can predict the enveloped surface of the vaporizing injected flow; i.e. (X_L, Y_L), and also from the cylindrical blast wave equation of (2.18), one can predict the leading shock shape, i.e. (ξ_L, η_L), as seen in Fig. 4.6. Undisturbed flow of Mach Number M_1 turns

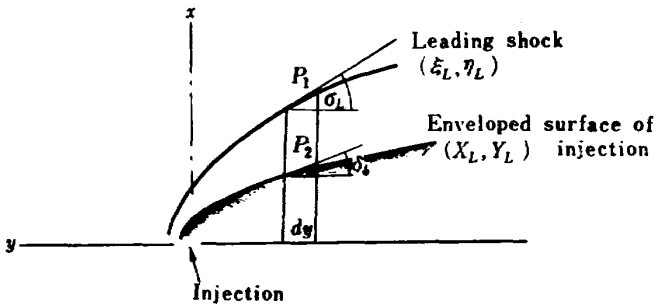

Fig. 4.6 Analytic estimation of produced control force in the down stream of injection point.

through the leading shock with oblique shock angle σ_L. Two conditions of M_1 and σ_L give turning angle across shock, δ_L, aft-leading shock pressure P_2, and Mach Number M_2 from oblique shock relations. If the tangent of enveloped surface of injectant to the wall, δ_b, is larger than δ_L, then a weak recompression occurs by turning

Table 4.4 Measured static pressures of leading shock recompression region of LITVC (2nd and 3rd series)

Measured static pressures at expansion ratio 4.96, $M_\infty=2.96$, $\gamma=1.3$						Theoretical	
P_{c0} kg/cm²ab	P_∞ kg/cm²ab	$P_{\#1}$ kg/cm²ab	$P_{\#2}$ kg/cm²ab	$P_{\#3}$ kg/cm²ab	$P_{\#4}$ kg/cm²ab	P_∞ kg/cm²ab	$\bar{P}_2$ kg/cm²ab
46.0	1.64	1.93	—	—	2.13	1.21	1.92
44.0	1.13	1.58	—	—	2.10	1.16	2.14
54.8	1.78	2.28	—	2.91	2.15	1.45	2.53
51.6	1.58	2.28	—	2.91	1.98	1.36	2.36
52.1	1.59	2.08	—	1.65	1.97	1.38	2.13
55.0	1.86	2.60	—	—	2.35	1.46	1.94
51.0	1.75	2.26	—	—	2.23	1.35	2.12
50.8	1.58	2.06	—	—	2.06	1.32	2.10

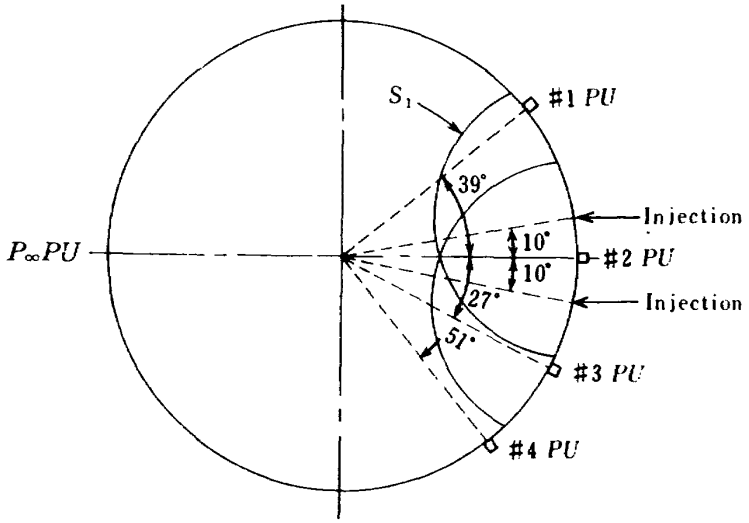

Expansion ratio = 4.96

aft-leading shock flow along the injection flow, and if δ_b is smaller than δ_L, then a weak expansion occurs, inversely. As long as the deflection angle is small, the linearized theory gives

$$P_2' = P_2\left\{1+\frac{\gamma P_2 M_2^2}{\sqrt{M_2^2-1}}(\delta_b-\delta_L)\right\} \quad (4.8)$$

Thus, the integration of the pressure increase in leading shock disturbed area,

$$F_4 = \cos\alpha_N \int_{\xi=(d_{0M}+d_N)}^{\xi=\xi_{ex}} 2(\bar{P}_2-P_1)(\eta_L-Y_L)d\xi \quad (4.9)$$

and of the injection flow area,

$$F_5 = \cos\alpha_N \int_{\xi=(d_{0M}+d_N)}^{\xi=\xi_{ex}} 2(P_2'-P_1)Y_L d\xi \quad (4.10)$$

where $\bar{P}_2=(P_2+P_2')/2$ and concave surfaces of main nozzle and of leading shock wave were not considered here for simplicity.

The static pressures of the disturbed area by leading shock waves were measured in the second and the third series of the present LITVC test runs. The calculated pressures from Eq. (4.8) also are compared in Table 4.4. It shows good agreement. The estimation of produced control forces, according to the above simple analysis, is compared to the results of LITVC test runs in Tables 4.2 and 4.3. The tables show that the agreement is worse than that of GITVC of the present study. The simple analysis for predicting liquid injection flow may be insufficient. Detailed investigation of injection flow pattern and induced leading shocks of LITVC, such as conducted in the previous sections, is needed to estimate more accurate LITVC control forces.

CONCLUDING REMARKS

While the experiment reported herein is in the limited range, from the analysis of the experimental results, the following can be concluded:

(1) From the optical observation of the two-dimensional nozzle flow test runs, it was found out that two kinds of disturbances existed. One is such that the penetrating height of under-expanding injectoin flow is almost the same order of the thickness of turbulent boundary layer near the injection port. Another is that an under-expanding injection flow protrudes deep into nozzle main flow, breaking through turbulent boundary layer. The results give an evidence that justifies the flow pattern model predicted by Charwat and Allegre[24].

(2) The first type of separation induced by secondary gas injection agrees well with the Mager's model separated by wedge shocks. It is supposed that one can estimate well the produced control forces of this type by the method of the reference 23.

(3) The separation shock angles of the second type may agree better with the Mager's model separated by conical shocks rather than with the wedge ones. But the difference may be within 10 degrees.

(4) As for the second type of flowfield, an analytical model is presented to predict free jet boundary of under-expanding injection gas flow protruding deep into nozzle main flow, penetrating length with standing Riemann wave, detached shock distances and radii ahead of injection flow, and interaction between separation shock and detached shocks. The analysis near the injection port agreed well with the experimental results of two-dimensional nozzle flow test runs.

(5) An exact conical lens equation is obtained, such that incoming parallel light rays traverse in parallel the bore of a conical pipe by compensating the refractions on the outer and the inner surfaces, and go out parallel by the same twice refractions.

(6) Using the characteristics of the conical lens equations, a method to generate conical lens surface has been developed. Four lenses have been machined and polished according to the principle. The performances of the lenses were investigated. If the incident angle approaches to 90 degrees, then the lens performance deteriorates, however the dead angle zones of the polished lenses were 10°-20°. Thus, it was found out that phenomenon in a conical pipe could be accurately observed by the use of the lenses.

(7) A series of evolved shapes of shock waves induced by secondary injection also could be taken by the use of rotatable conical lens.

(8) By comparing the shadowgraphs of the leading shock waves induced in a supersonic conical flow with an analysis to predict the shapes, it was shown that Eq. (2.18) agreed better with the three-dimensional tests than Eq. (2.19) of Hsia, Seifert, and Karamcheti, which had been in some time used for the prediction of SITVC.

(9) In applying the cylindrical blast wave ana

logy SITVC problem, the axis of symmetry must be parallel to the nozzle wall rather than the axis of rocket nozzle. This experimental conclusion may answer to the question, presented by Hsia, Seifert, and Karamcheti[15], as to whether or not it is valid to assume that the axis is parallel to the nozzle axis for all conditions of injection.

(10) It was found out, from a series of evolved shadowpraphs by the use of rotatable type conical lens, that the surface of the leading shock wave induced by the secondary air injection into the supersonic conical main flow was not that of axisymmetrical revolution but that of an oblate spheroid. In the tested region of the SITVC conditions, the cross section could be regarded as an ellipse, and the ratio of the semimajor to the semiminor was 1.5 with accuracy of 9%. This experimental result answer to the question presented by Hsia, Seifert, and Karamcheti[15], "it is not clear whether the shock surface can be assumed to be axisymmetrical".

(11) Being based on the investigation of underexpanding gas injection flows in the two-dimensional and conical nozzle flows, an estimation method for control forces of GITVC has been presented. Comparing the measured control forces of GITVC conducted by solid propellant rockets with the theoretical estimation, the presented method has been shown to be pretty well predictable.

(12) An experimental and analytical investigation of LITVC also was conducted to discuss the difference of control force producing mechanism from that of GITVC. The difference from that of GITVC, that is, a pressure increase aft-leading shock wave flowfield in the downstream of injection, has been shown to agree well with the experimental results of LITVC conducted by solid propellant rockets. However, due to the lack of information of leading shock wave induced by liquid injection, a simple analysis of estimating control force is worse than that of GITVC.

The approach presented in this study appears to offer an useful method for GITVC and a key to solve LITVC problem. To establish fully the method presented here, further investigations are needed. The followings are suggested to be further studied.

(1) Separation shock diffusing region into turbulent boundary layer should be studied.

(2) In the case of multi ports injections, interaction between injections should be studied.

(3) Disturbances induced by a chemically reactive injectant should be studied.

(4) Disturbances induced by liquid injection should be experimentally investigated.

ACKNOWLEDGEMENTS

The author wishes to express his thanks to the former Rocket Propulsion Division and National Space Development Agency for asisting in the support of this work.

An original manuscript of this paper was presented to the Graduate Faculty of Tokyo University as a thesis in partial fulfillment of the requirements for the degree of Doctor Engineering. The author would like to express his sincere appreciation to the chairman of his Thesis Committee, Professor Fumio Tamaki of Tokyo University, for his guidance, suggestions, and criticisms during the preparation of this paper.

He is indebted to Mr. Heihachiro Kamimura for assistance in the reduction of data and in taking the photographs which play such an important part in this work.

Finally, the author wishes to express his gratitude to his wife, Akio, who remained patient and encouraging throughout its preparation.

REFERENCES

[1] Wu, J., Chapkis R. L., and Mager, A., "Approximate Analysis of Thrust Vector Control by Fluid Injection," ARS Journal, December 1961, pp. 1677-1685.

[2] Broadwell J. E., "Analysis of the Fluid Mechanics of Secondary Injection for Thrust Vector Control," AIAA Journal Vol. 1, No. 5, May 1963, pp. 1067-1075.

[3] Karamcheti K., and Hsia H. T., "Integral Approach to an Approximate Analysis of Thrust Vector Control by Secondary Injection," AIAA Journal Vol. 1, No. 11, November 1963, pp. 2538-2544.

[4] Sehgal R., and Wu J., "Thrust Vector Control by Liquid Injection into Rocket Nozzles," Journal of Spacecraft and Rockets Vol. 1, No. 5, September-October 1964, pp. 545-551.

[5] Werle M., "A Critical Review of Analytical Methods for Estimating Control Forces Produced by Secondary Injection," U.S. Naval

Ordnance Laboratory, Maryland, NOLTR 68-5, January 1968.

[6] Neilson J. H., Gilchrist A., and Lee C. K., "A Theory for the Side Force Produced in Two-Dimensional nozzles by Secondary Gas Injection," The Aeronautical Journal of the Royal Aeronautical Society, Vol. 72, March 1968, pp. 267-274.

[7] Mager A., "On the Model of the Free, Shock-Separated, Turbulent Boundary Layer," Journal of the Aeronautical Sciences, February 1956, pp. 181-184.

[8] Yamanaka T., and Azuma H., "A Method for Observing Phenomena in an Arbitrary Pipe Flowfield of Revolution," Journal of Spacecraft and Rockets, Vol. 4, No. 9, 1967, pp. 1272-1274.

[9] Yamanaka T., "Flow Visualization of Shock Waves Induced by a Secondary Gas Injection by the Use of Conical Lens," Proceedings of the 8th International Symposium on Space Technology and Science, Tokyo, 1969, edited by Takano A., and others, (AGNE Publishing Inc., Tokyo, 1969), pp. 379-389.

[10] Yamanaka T., Saito M., Suzuki T., and Ito T., "An Experimental and Analytical Investigation of Estimating Control Forces Produced by Secondary Injection," XXth Congress of the International Astronautical Federation, Mar del Plata, Argentina, October 1969.

[11] Schetz J. A., "Penetration of Gaseous Jets Injected into a Supersonic Stream," Journal of Spacecraft and Rockets, Vol. 3, No. 11, November 1966, pp. 1658-1665.

[12] Abramovich G. N., The Theory of Turbulent Jets, (Massachusetts Institute of Technology Press, Cambridge, Mass., 1963), Chap. 12, Sec. 4.

[13] Kaattari G. E., "Method for Predicting Shock Shapes and Pressure Distributions for a Wide Variety of Blunt Bodies at Zero Angle of Attack," NASA TN D-4539, April 1968.

[14] Zukoski E. E., and Spaid F. W., "Secondary Injection of Gases into a Supersonic Flow," AIAA Journal, Vol. 2, No. 10, 1964, pp. 1689-1696.

[15] Hsia H. T., Seifert H. S., and Karamcheti K., "Shocks Induced by Secondary Fluid Injection," Journal of Spacecraft and Rockets, Vol. 2, No. 1, 1965, pp. 67-72.

[16] Guhse R. D., "An Experimental Investigation of Thrust Vector Control by Secondary Injection," Jet Propulsion Center, Purdue University, Report No. TM-65-3, March 1965.

[17] Hawk N. E., and Amick J. L., "Two-Dimensional Secondary Jet Interaction with a Supersonic Stream," AIAA Journal Vol. 5, No. 4, 1967, pp. 655-659.

[18] Niksch G. L., and Guhse R. D., "Parameters Influencing Thrust Vector Control by Secondary Injection," Jet Propulsion Center, Purdue University, Report No. TM-67-6, August 1967.

[19] Lees L., and Kubota T., "Inviscid Flow over Blunt-Nosed Slender Bodies," Journal of the Aeronautical Sciences, March 1957, pp. 159-202.

[20] Yamanaka T., "Shock Waves in a Conical Nozzle Supersonic Flow," Transaction of the Japan Society for Aeronautical and Space Sciences, Vol. 10, No. 16, 1967, pp. 1-10.

[21] Sakurai A., "On the Propagation and Structure of the Blast Wave, I," Journal of the Physical Society of Japan, Vol. 8, No. 5, September-October 1953, pp. 662-669.

[22] Sakurai A., "On the Propagation and Structure of a Blast Wave, II," Journal of the Physical Society of Japan, Vol. 9, No. 2, March-April 1954, pp. 256-266.

[23] Sperry Rand Corp., "Proportional Solid Propellant Secondary Injection Thrust Vector Control Study," NASA CR-637, November 1966.

[24] Charwat A. F., and Allegre J., "Interaction of a Supersonic Stream and a Transverse Supersonic Jet," AIAA Journal Vol. 2, No. 11, 1964, pp. 1965-1972.

[25] Love E. S., Grigsby C. E., and Lee L. P., "Experimental and Theoretical Studies of Axisymmetric Free Jets," NASA TR R-6, 1959.

[26] Adamson Jr., T. C., and Nicholls J. A., "On the Structure of Jets from Highly Under-expanded Nozzles into Still Air," J. Aero/Space S. January, 1959, pp. 16-24.

[27] Johannesen N. H., and Meyer R. E., "Axially-Symmetrical Flow near the Centre of an Expansion," The Aeronautical Quarterly, Vol. II, August 1950, pp. 127-142.

TR-276	Overall Ground Experiments on Flying Test Bed for VTOL Aircrafts at National Aerospace Laboratory.	Naoto TAKIZAWA, Yoshikazu TANABE, Akiyoshi SHIBUTANI, Toshio OGAWA, Kakushun FUJIEDA, Tadao KAI, Hiroshi NISHIMURA, Koichi ONO & Yoshio GOTO	Feb. 1972
TR-277	Development of Turbulent Boundary Layers Along the Curred Walls of an Annular Diffusing Passages	Shoichi FUJII, Mitsuo GOMI, Hideo NISHIWAKI & Theodore H. OKIISHI	Feb. 1972
TR-278T	Development of Turbulent Boundary Layers Along the Curred Walls of an Annular Diffusing Passage	Shoichi FUJII & Theodore H. OKIISHI	Feb. 1972
TR-279	Stress and Strain Concentration Factor of Strigs with a Control Circular Hole in Linearly Herdening	Yoshio AOKI, Makoto KURAMOTO, Yoshito KOBAYASHI & Takeshi KUNIO	Feb. 1972
TR-280	Experimental Study on the Hypersonic Aerodynamic Characteristics of Spherically Blunted Cones by the Gun Tunnel	Kunio SOGA & Nobuyuki ONODERA	May 1972
TR-281	Digital Control of Jet Engines (1) Control System and Preliminary Experiment	Kenji NISHIO, Masanori ENDO, Nanahisa SUGIYAMA, Takeshi KOSHINUMA, Toshimi OHATA, Yukio MATSUDA, Akira YOSHIDA & Osamu NAKAYAMA	Jul. 1972
TR-282	On the High Temperature Turbine Test Facilities and the Data Processing System	Aeroengine Division	Jun. 1972
TR-283	Real-time Simulation of Jet Engines with Digital Computer (I) (Fabrication and Characteristics of the Simulator)	Kenji NISHIO, Nanahisa SUGIYAMA, Takeshi KOSHINUMA, Takeo HASHIMOTO, Toshimi OHATA & Hideo ICHIKAWA	Jul. 1972
TR-284	Study on Performance of Ball Bearings at d_n Values	Yukio MIYAKAWA, Katsumi SEKI & Masayuki YOKOYAMA	May 1972
TR-285	Study on Lead Monoxide as Solid Lubricant for High Temperatures	Yukio MIYAKAWA, Makoto NISHIMURA & Wataru ABE	May 1972

TECHNICAL REPORT OF NATIONAL AEROSPACE RABORATORY
TR-286T

航空宇宙技術研究所報告 286 T 号 (欧文)

昭和 47 年 5 月 発行

発行所 航空宇宙技術研究所
東京都調布市深大寺町 1,880
電話武蔵野三鷹(0422)47-5911(大代表)
印刷所 有限会社 啓文堂松本印刷
東京都文京区水道 2—7—5

Published by
NATIONAL AEROSPACE LABORATORY
1,880 Jindaiji, Chōfu, Tokyo
JAPAN

Printed in Japan